Roles of Metal Oxides on the Activity of Fuel Cells Electrocatalysts

リベラ ロカバド デイビッド サムエル

https://hdl.handle.net/2324/1959129

出版情報：Kyushu University, 2018, 博士（工学）, 課程博士
バージョン：
権利関係：

Roles of Metal Oxides on the Activity of Fuel Cells Electrocatalysts

David Samuel Rivera Rocabado

2018 年 7 月

Roles of Metal Oxides on the Activity of Fuel Cells Electrocatalysts

九州大学
KYUSHU UNIVERSITY

A dissertation submitted to the Kyushu University
in partial fulfillment of the requirements for the
degree of Doctor of Engineering

By

David Samuel Rivera Rocabado

Department of Hydrogen Energy Systems
Graduate School of Engineering
Kyushu University

Approved by:

Prof. Akari Hayashi (examiner/supervisor)
Department of Hydrogen Energy Systems, Graduate School of Engineering, Kyushu University

Prof. Michihisa Koyama (examiner/supervisor)
Department of Hydrogen Energy Systems, Graduate School of Engineering, Kyushu University

Prof. Kazunari Yoshizawa (examiner)
Department of Chemistry and Biochemistry Graduate School of Engineering, Kyushu University

Fukuoka, Japan
2018

ABSTRACT

Fuel cells are among the potential candidates to help decrease local and global environmental impacts. Decades of research, development, demonstration, dissemination, and governmental involvement led to the commercialization of the polymer electrolyte and solid oxide fuel cells. However, their commercialization is limited due to several long-standing issues. Thus several researchers have been focused on finding alternative materials for the next generation fuel cells. Among the targeted materials, metal oxides, and metal oxides-based materials showed not only promising catalytic activities but also improved stabilities. Nevertheless, in some cases, the reason behind this improvement has only been hypothesized, and no conclusive results were presented. The development of new theoretical approaches formulated on a molecular level, by means of computer simulation methods are targeted as key tools to obtain sufficient knowledge of the factors determining catalytic activity, which can lead to tailoring catalysts with improved activities and selectivities. In this work, the roles of two different oxides in the activity of fuel cells electrocatalysts were studied using density functional theory method.

In Chapter 1 a concise introduction about the operating principles, components, materials, benefits, and disadvantages of solid oxide and polymer electrolyte fuel cells is given. The use of $BaTiO_3$ and Pt-nanoparticles supported on SnO_2 and their limitations when used as fuel cell materials are also described.

The theoretical background of the density functional theory method is presented in Chapter 2.

In Chapter 3 the role of $BaTiO_3$ as a solid oxide fuel cell anode was studied. First, the likelihood of the sulfidation of the $BaTiO_3$(001) surfaces was estimated via different reaction pathways. Next, the hydrogen oxidation reaction and methane sequential decomposition on pristine $BaTiO_3$(001) were studied, and the effect of sulfur on these reactions was evaluated. For the hydrogen oxidation reaction, the presence of sulfur activated the H-H bond, led to the formation of different molecular entities; thus alternative sequences of elementary steps for the reaction to proceed came to light and promoted the formation of some intermediates such as oxygen vacancy formation. On the other hand, for the methane sequential dissociation, methane activation and the promoted scission of some C-H bonds may be responsible for the mentioned boost in I-V characteristics.

In Chapter 4 the role of SnO_2 as support material for Pt-nanoparticles as polymer electrolyte fuel cell electrocatalyst was investigated based on changes in the nanoparticles' geometrical features, electronic and chemical properties, and stability. The O-atom binding energy was successfully decomposed as a linear combination of the nanoparticles' properties, and a generalized model that can describe the O-atom binding energy considering the variation of the nanoparticle size, adsorption site, and support effect was proposed. SnO_2 has a negative effect on the oxygen reduction reaction as it stabilizes the interaction between the Pt-nanoparticles and oxygenated species that can effectively block the active sites of the Pt-nanoparticles required for the adsorption and dissociation of O_2. This strong interaction can lead to the formation and later dissolution of PtO_x during the electrochemical reduction of O_2. Additionally, SnO_2 weakened the interatomic interaction of the outer-shell atoms of small size nanoparticles, while for Pt-nanoparticles larger than 1.70 nm a slight increase in the Pt-Pt interaction was observed, which in part can explain the higher stability of Pt-nanoparticles when SnO_2 is used as support material.

In Chapter 5, the main results are summarized, the conclusions of this work are outlined, and the future directions are considered.

ACKNOWLEDGMENTS

At first, I would like to thank, Professor Michihisa Koyama for accepting me into his group. Since I joined his laboratory, Professor Koyama contributed to a rewarding research experience by giving me intellectual freedom in my work, supporting my attendance at various conferences, engaging me in new ideas, and demanding a high-quality work in all my activities.

I want to express my gratitude to Professor Akari Hayashi, for accepting me into her research group at the last stage of the Doctor Course, for her comments and advice to improve my thesis manuscript and presentation, and for her support, help, patience, and making me feel welcome into her research group.

I would also like to thank Professor Kazunari Yoshizawa for his kind acceptance to participate as examiner of my thesis, and for his insightful comments and questions during my thesis presentation.

Additionally, I would also like to thank Professor Takayoshi Ishimoto for his academic assistance and guidance, and personal support, I gained a lot from his vast theoretical knowledge and advice during the time spent together.

Likewise, I would like to thank Professor Alexandar Staykov for his teachings, constant help, encouragement and friendship.

Also, my gratitude goes to Professor Stephen Lyth and Professor Masamichi Nishihara for their advice, constructive comments, help, and knowledge shared.

I gratefully acknowledge the funding from the Ministry of Education, Culture, Sports, Science and Technology of Japan that made my Doctor Course possible. I would like to recognize the Professors and staff at the Department of Hydrogen Energy Systems at Kyushu University for the vast knowledge and help received.

I want to express gratitude to the staff members, postdocs, and students at INAMORI Frontier Research Center and at the International Institute for Carbon-Neutral Energy Research (I^2CNER). Thank you for the friendly and cooperative atmosphere and memorable time shared together.

I would like to thank all members of the Kyushu University Shorinji Kempo Club for all the good and tough times during the practices, for the great adventures and all the fun we had together.

My special thanks to Miss Ara Cho for her help, encouragement, understanding, and patience. For always believing in me and pushing me not to give up. For the fantastic adventures and time spent together, and always trying to make me feel special.

Lastly, I would like to thank my family for all their love, support and encouragement. All that I am and hope to be, I owe to my parents. Their values, teachings, strength, sacrifices, and patience allowed me to become the person I am today. To my sisters for always believing in me even when I did not believe in myself, for their help, support, and the good moments shared.

Fukuoka, June 2018

David Rivera

TABLE OF CONTENTS

CHAPTER 4. Theoretical Study of SnO$_2$ as Support Material for Polymer Electrolyte Fuel Cell Electrocatalyst ··· 81

LIST OF TABLES

LIST OF FIGURES

CHAPTER 1

Introduction

Catalysis has enormous technological significance in the production and processing of fuels, manufacture of chemicals and pharmaceuticals, energy conversion, environmental technologies, etc.[1-4] Catalysis is a support of our current life, the growing demand for better chemicals and fuels to improve our quality of living resulted in a parallel demand for better catalyst. Since most industrial chemical processes such as chemical, petrochemical, biochemical, polymers production and environmental protection use catalysts, the importance and economical significance of catalysis is enormous.[3]

Based on the physical phase formed, catalysts can be divided in two types, homogenous where the catalysts and the reactants form a common physical phase, and heterogeneous catalysts that involve the formation of separate physical phases. Typical heterogeneous catalysts are inorganic solids such as metals, oxides, sulfides, metal salts, additionally they can also be organic materials such as organic hydroperoxides, ion exchangers, and enzymes.

Among the different type of heterogeneously catalyzed reactions, photocatalysis, biocatalysis, environmental catalysis, and electrocatalysis are special cases as they are potential candidates to help decrease local and global environmental impacts. In recent decades, the international awareness of environmental problems has grown due to the use of the global atmosphere as waste depository for greenhouse gases creating changes in climate that threaten human habitats and sustenance activities around the world.[5] In this regard, research into cleaner, more efficient technologies, and alternative options for long-term, environmentally friendly, and acceptable cost energy supply is being conducted.

The use of energy from renewable sources, and fuel cells can contribute to securing long-term sustainable energy supplies, help decreasing local and global environmental impacts and make available commercially attractive options to meet specific energy service needs, particularly in developing countries and rural areas, additionally to creating new employment opportunities directly or indirectly.[6,7]

Since the early 90's, fuel cells started to be targeted as promising devices to meet the power needs of applications ranging from portable electronics, transportation, building cogeneration to distribution power plants. Additionally to their modularity, they are considered as one of the most favorable technologies to face the future power generation requirements because they can convert efficiently the chemical energy to electricity, and consequently reducing the fuel consumption and pollutant emissions such as NO_x, SO_x, and CO_2.[8] Furthermore, as the combustion reaction does not occur, fuel cells are low noise pollutants,[9,10] and because there are no mobile parts in a fuel cell, no degradation or failure due to tribological problems occurs.

Fuel cells are usually classified by the electrolyte employed in the cell, with the exception of direct methanol fuel cell (DMFC) in which methanol is electrochemically oxidized directly in the fuel cell. A second and more adequate classification is by the operating temperature of each of the fuel cell. Low temperature fuel cells are the polymer electrolyte fuel cell (PEFC), the alkaline fuel cell (AFC), the DMFC, and the phosphoric acid fuel cell (PAFC). The high temperature fuel cells operate at 500-1000 °C and are classed into two types, the molten carbonate fuel cell (MCFC), and the solid oxide fuel cell (SOFC). In Table 1-1 the components, charge carrier, operating temperatures, typical fuels used in the different type of fuel cells are summarized.

Table 1-1. Fuel cell types and selected features[11,12,13]

	PEFC	PAFC	AFC	MCFC	SOFC
Electrolyte	Cation exchange membrane	Concentrated H_3PO_4 solution	KOH solution	$(Li,K)_2CO_3$	$ZrO_2(Y_2O_3)$, $ZrO_2(Sc_2O_3)$, $CeO_2(Gd_2O_3)$
Anode	Pt-based catalyst	Pt-based catalyst	Pt-based catalyst	Ni	Ni- $ZrO_2(Y_2O_3)$
Cathode	Pt-based catalyst	Pt-based catalyst	Pt-based catalyst	$Li_xNi_{1-x}O$	$La(Sr)MnO_3$, $La(Sr)Co(Fe)O_3$
Charge carrier	H^+	H^+	OH^-	CO_3^{2-}	O^{2-}
Temperature (°C)	20-80	160-210	20-90	600-700	600-1000
Fuels	H_2, alcohol	H_2	H_2	H_2, CO	H_2, CO, C_xH_y

In Japan, the research to develop fuel cells was initiated by research institutions around 1955. The Agency of Industrial Science and Technology (AIST) under Japan's Ministry of Economy, Trade and Industry (METI) started the Moonlight Project in 1981 to engage research on the PAFC, MCFC, and SOFC.[14] A governmental plan, in 1993 combined the existing Sunshine Project for research and development in renewables (initiated in 1974), the Moonlight Project for research and development in energy conservation technologies (initiated in 1978), and research projects for environmental technologies (initiated in 1989) into the New Sunshine Project.[15] This project aimed to promote technologies for renewables, energy conservation, and environmental protection where besides the research on PAFC, SOFC, and MCFC, PEFCs were targeted to be used in transportation and commercial applications. The first full-scale efforts to commercialize PEFCs were initiated under a sub-project incorporated in the "Millennium Project" in the Japanese fiscal year of 2000. A large scale demonstration program, totaling 3300 units, and consumer education and advertising strategy to generate a high level of consumer awareness began in 2005. These efforts and generous subsidies from part of the government resulted in the-first-in-the-world commercialization of PEFC based combined heat and power system ENE-FARM (later called type P) in 2009, and an SOFC system called ENE-FARM type S in 2011.[16] As of March 2018, more than 257,339 units of the two types of ENE-FARM systems have been installed.[17] The New Energy and Industrial Technology Development Organization (NEDO) continues to contribute to research, development, demonstration and dissemination of fuel cell technologies to construct a hydrogen economy in the future. In this work, the major features, properties, limitations, and two different research topics from an atomistic point of view of the SOFC, and PEFC are provided.

1.1 SOLID OXIDE FUEL CELLS

An SOFC consists of four major components: two porous electrodes (cathode and anode) separated by a solid oxide ion (O^{2-}) conducting electrolyte, and the interconnector. The most investigated SOFC is composed of a nickel and yttria-stabilized zirconia (YSZ) composite (Ni-YSZ) anode, YSZ oxide-ion conducting electrolyte and lanthanum strontium manganite, $La_{0.8}Sr_{0.8}MnO_3$ (LSM) cathode.[11] The anodic electrochemical reactions occur at the triple-phase boundary (TPB), where gases from the oxidant or fuel, electrons, and oxide ions meet. At the cathode, oxygen from the air is reduced according to equation 1-1 and the resulting O^{2-} ions are transported through the electrolyte lattice to the anode where they react with the gaseous fuel, yielding heat, H_2O and in the case of hydrocarbons fuels, CO_2, and releasing electrons as shown in equation 1-2, and equation 1-3, respectively.

Cathode: $$O_2 + 4e^- \rightarrow 2O^{2-}, \tag{1-1}$$

Anode: $$2H_2 + 2O^{2-} \rightarrow 2H_2O + 4e^-, \tag{1-2}$$

$$C_nH_m + \left(2n + \frac{m}{2}\right)O^{2-} \rightarrow \frac{m}{2}H_2O + nCO_2 + (4n+m)e^-, \tag{1-3}$$

In order to balance the charges of the reaction, electrons move from the anode to the cathode through the external circuit, while O^{2-} ions move through the electrolyte internally. In Figure 1-1, a schematic view of the microstructure of the oxygen and fuel electrodes, the chemical reactions at each electrode's TPBs and the electronic and ionic pathways are shown.

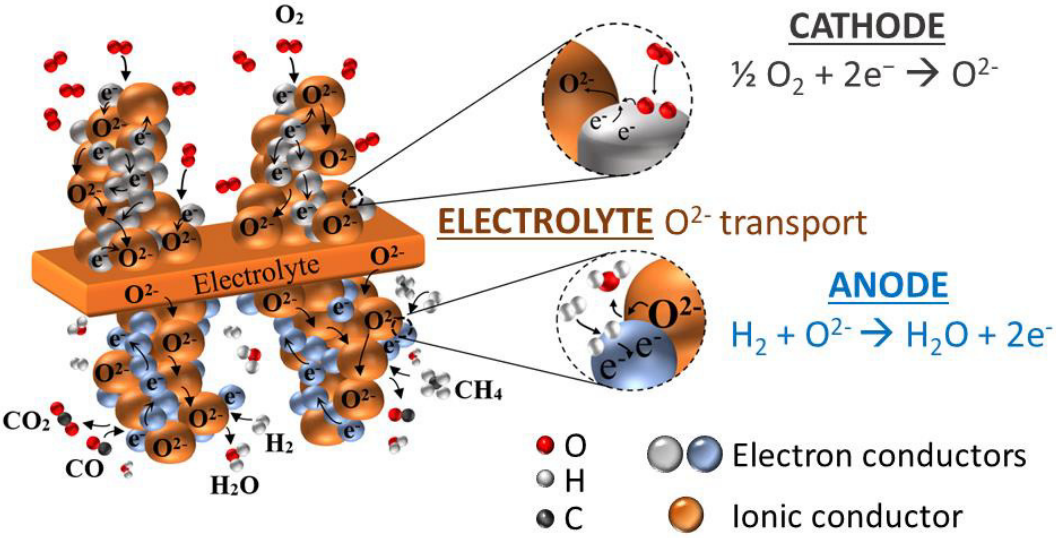

Figure 1-1. Schematic drawing of the anode and cathode microstructure. TPBs, electronic and ionic pathways, and chemical reactions are also shown.

Multiple cells can be coupled via interconnectors that offer both electrical contacts and gas channels between the individual cells. The resultant "stacks" are then arranged in series and parallel configurations to deliver the desired voltage and power outputs for portable, transportation applications, distributed generation and large-scale power generation.[18] For practical applications, the SOFC cell structure can be planar, tubular and flattened tubular. Figure 1-2 shows a flattened tubular cell and the assembly of the cells. The flattened-tubular configuration was adopted by Kyocera Corporation, Osaka Gas and AIST.[17] Furthermore, because they operate at high temperatures (600-1000 °C), SOFCs are fuel flexible, capable of operating on hydrogen, ammonia,[19-22] synthesis gas,[23,24] biofuels,[25-29] oxygenates,[30,31] hydrocarbons,[32-36] carbon,[37,38] etc. Additionally, the pressurized SOFCs are suitable to be combined with gas turbines, steam turbines, combination of gas and steam turbines, and combination of gasifiers, gas and steam turbines to form hybrid cycle power systems, which can reach high electrical and total efficiencies.[39-42]

On the other hand, among the disadvantages, in the practical operation, most fuels contain impurities that may attack the active sites of the eletrocatalysts decreasing the performance and often influencing the long term stability. Moreover, at high operating temperatures, small differences in the thermal expansion coefficient between the different materials result in stresses that cause cracking as a result of the fatigue stress caused by thermal cycling.[43,44] For the case of planar SOFCs, the sealing material's thermal expansion coefficient has to be equivalent to the one of the SOFC, and simultaneously keep a viscosity that is tolerant to thermal cycling and sustaining a gas-tight seal in all the range of conditions.[45] Moreover, the elemental interdiffusion and migration, metallic corrosion and ceramic aging effects are thermally activated processes, hence achieving good chemical stability at high temperatures could be a limiting factor.[44,45] Furthermore, the high operating temperatures usually require slow temperature change during start-up and shutdown cycles that dramatically limits the applicability in portable and transportation markets.

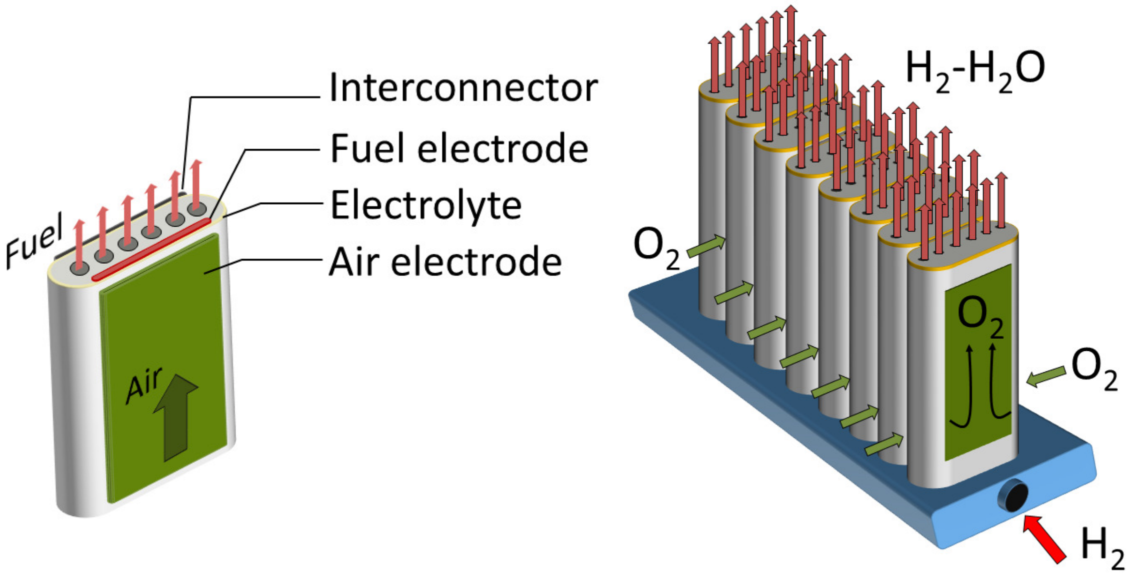

Figure 1-2. Drawing schematics of a flattened-tubular cell and the stack.

1.1.1 Ni-YSZ SOFC anodes. In the conventional Ni-YSZ cermet anode, nickel has the roles of catalyst, and electrical current collector.[46-49] In addition to having an excellent activity for the oxidation of hydrogen,[11,47-50] nickel possesses a high activity for methane steam reforming.[47-49,51] However, it also catalyzes the reactions that lead to the formation of different carbon forms. The main reactions leading to carbon deposition when carbon-containing fuels are involved are the following:[52]

CO disproportionation: $2CO_{(g)} \rightarrow C_{(s)} + CO_{2(g)},$ (1-4)

Syngas reaction: $CO_{(g)} + H_{2(g)} \rightarrow C_{(s)} + H_2O_{(g)},$ (1-5)

Hydrocarbon decomposition: $C_nH_{m(g)} \rightarrow nC_{(g)} + \frac{m}{2}H_{2(g)}$, (1-6)

The CO disproportionation, also known as the Boudouard reaction, is an exothermic reaction, however it becomes favorable at lower temperatures due to the reduction in entropy. Similarly, the syngas reaction is also more favorable at lower temperatures. On the other hand, the hydrocarbons decomposition is an endothermic reaction and favored at high temperatures. The mechanism of carbon formation varies with the material and it can lead to different carbon morphologies such as nanotubes, char, amorphous and graphitic whisker.[11,47,48,53,54] When carbon deposition takes place on metal particles, the deactivation can be due to strong chemisorption or physisorption of C-atoms blocking the active sites, complete deactivation of the metal particles due to encapsulation and pore blocking limiting the access of the reactants to the catalyst, growth of carbon whisker carbon that can stress and fracture the support or push the metal particles off the support, dissolution of carbon atoms into the metal (dusting), causing a volume expansion destroying the structure of the anode, etc.[55]

Another example of degradation arises from impurities found in most fuels such as phosphorous-, boron-, chlorine-, silicon-, and sulfur-based compounds.[56] These impurities may attack the active sites of the electrocatalysts hence decreasing the performance and often influencing the long term stability. Among the different impurities, H_2S can drastically lower the performance of SOFC even at ppm concentrations.[57-62] Thus, the need of a cleaning system to remove the small concentration of impurities adds an extra cost and increases the footprint to the overall SOFC system.[63] It was reported that the poisoning effect of sulfur decreases in the order of H_2S, SO_2, and SO_4^{2-}.[64] At the majority of conditions occurring in an SOFC anode, sulfur compounds are converted into H_2S.[65,66] Theoretical studies showed that the decrease of the anode performance under H_2S containing gas mixtures was due to the strong adsorption of S-atom on Ni-atoms, thus blocking the active sites of the anode after the H_2S dissociation.[67,68] The dissociation of H_2S leading to S-atom adsorbed on Ni(111) was shown to be a favorable process with large exothermic reaction energies and low activation energies.[69] Experimental studies have shown that the performance degradation is proportional to sulfur coverage at constant current density in SOFC anodes.[70] Theoretical studies confirmed the decrease in performance due to an increment in the kinetic barrier for the H_2[71] and CH_4[72] dissociation as the sulfur coverage increases. A Ni-S phase diagram showed that the sulfur poisoning is fully recoverable before the formation of Ni_3S_2.[73] Thus, avoiding the dissociation of H_2S will lead to a greater sulfur resistance. Alloying Ni with Cu increased Ni resistance to sulfur poisoning.[74] Nevertheless, the main problem of these alternative materials is their poor catalytic activity for the hydrogen oxidation reaction (HOR).[74,75]

Additionally, carbon deposition is strongly affected by the presence of sulfur in the fuel.[52] Sulfur deactivation can reduce the carbon by blocking the access to the catalytic centers.[76] At coverage ratios of around 0.7, it is possible to diminish carbon deposition without compromising reforming activity.[77-79] It was shown that, carbon nucleation needs larger sites that at the high coverages of S-atom are almost completely blocked, while methane reforming reactions can proceed in the smaller sites, which are still available. However, the complete inhibition of carbon formation is not possible. Instead, the usual whisker structure is replaced by less deactivating carbon forms.[77,80]

Moreover, material transport by evaporation/condensation and diffusion mechanisms can affect the long term degradation of the cell. These thermally activated processes and the steam content can lead to changes on the electrocatalyst surface morphology by the agglomeration of nickel particles that decreases the conductivity and the TPB length, hence increasing the polarization resistance for the electrochemical reactions.[53] In addition, due to mismatch of the thermal expansion coefficient, and elastic modulus between Ni and YSZ, thermomechanical degradation due to residual stress arises that may lead to delamination or cracking of the anode.[53,81]

In order to improve the long-term stability of the SOFC, a number of researchers are focused on finding alternative anode materials with lower predisposition to the above mentioned degradation mechanisms, but at the same time will retain the same catalytic activity and electronic conductivity.[49,82-85] The desired anode is supposed to have mixed ionic and electronic conductivity with predominant electronic conductivity to allow the transfer of electrons. It must be chemically compatible with the adjacent components (electrolyte and interconnector). It should also have thermal expansion coefficient close to those of adjoining components. It must show high electrocatalytic activity towards oxidation of fuel gases, and desired catalytic activity toward the hydrocarbon reforming. The anode ought to be fuel flexible and thermally and chemically stable in an impurity-containing fuel atmosphere for long-term service. A simple fabrication, and low cost are of tremendous importance for a wide range of commercial applications.[86-88] Although no material possesses all the aforementioned qualities, a combination of needs can be satisfied by using a mixed ionic-electronic conductor (MIEC) material as anode. Ceramics with both ionic and electronic conductivity at high temperature and in a reducing environment have received increasing interest in recent years on their application as SOFC anodes or anode components due to a combination of: 1) expanding the reaction sites from the TPB to the whole anode due to high ambipolar conductivity, hence reducing the interfacial polarization resistance; 2) relatively good compatibility with high-quality electrolytes, increased mechanical stability ensuring long term service without expansion of metal components; 3) improved sulfur tolerance compared to metal components.[48,86,87,89] Therefore, it is no surprise that significant research has been carried out to develop different MIEC anode materials for the application on fuel-flexible SOFC with sulfur tolerance. Among those materials, MIEC oxides with perovskite structures have drawn significant interest during the development of high performance sulfur-tolerant anode materials. Through the appropriate introduction of dopants, it is possible to obtain a large variety of materials with a wide range of properties and applications.[49,86-90]

1.1.2 Perovskite materials. The typical chemical formula of perovskite-type oxides is ABO_3, where A and B denote different cations. Their cubic structure consists of large-sized 12-coordinated cations at the A-site and small-sized 6-coordinated cations at the B-site,[11,44,90] the perovskite structure of $BaTiO_3$ is shown as example in Figure 1-3. Because of the variety of structures and chemical compositions, perovskite oxides exhibit a large variety of properties. Well-known properties are ferroelectricity ($BaTiO_3$, $PdTiO_3$), superconductivity ($YBa_2Cu_3O_7$, $HgBa_2Ca_2Cu_2O_8$), good electric conductivity which is close to that of metals ($LaCrO_3$, $SrFeO_3$), ionic conductivity ($BaZrO_3$, $BaCeO_3$), catalytic properties ($LaMnO_3$, $BaCuO_3$).

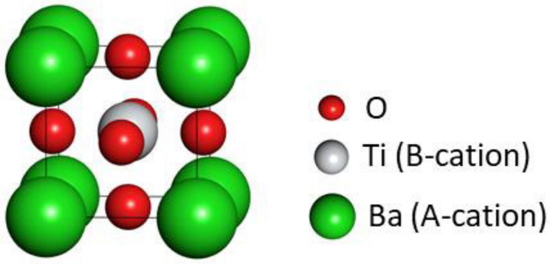

Figure 1-3. Cubic structure of $BaTiO_3$.

Moreover, a large amount of dopants of different valence and similar-size cations can be substituted into A and/or B sites to create oxygen or cation deficiencies. The substitution of the B-site ions with cations of lower or higher valence will form oxygen vacancies or interstitials, respectively, producing compounds of stoichiometry $AB_{(1-x)}B'_xO_{(3-/+\delta)}$. On one hand, the substitution of the A-site with cations of higher valence will form A-site vacancies, giving compounds of stoichiometry of $A_{(1-x)}A'_xBO_3$. On the other hand, if the substitution is with lower valence cations, it will introduce oxygen vacancies, giving compounds of stoichiometry $A_{(1-x)}A'_xBO_{(3-\delta)}$.[11,44,90] Additionally, their intrinsic structural stabilities exhibiting mixed ionic and electronic conductivity under a wide range of oxygen partial pressures and elevated temperatures.[11] Based on these variations on their properties, perovskite oxide materials have been intensively studied to find the most promising materials with improved properties than the current SOFC anode. It has been found that some perovskite materials can hinder the carbon deposition, due to higher availability of oxygen through the anode,[91,92] and a number of perovskite materials have been examined for application as sulfur-tolerant anodes.[51,93-99] However, few reported perovskite anodes with both sulfur tolerance and decent catalytic activity for H_2 oxidation comparable to that of Ni–YSZ anodes. Such is the case of $BaTiO_3$ anode, which was used in the presence of H_2 and CH_4 containing H_2S. Although the performance of $BaTiO_3$ was lower compared to Ni-YSZ, $BaTiO_3$ not only showed tolerance towards H_2S but the performance of the SOFC increased significantly.[94]

1.1.3 $BaTiO_3$ based materials. Since its discovery in 1943, $BaTiO_3$ has received much attention because it showed favorable application performances in ferroelectricity,[100] microelectronics,[101] photoelectronics,[102] and superconductivity.[103] Furthermore, $BaTiO_3$ has been studied for its catalytic properties in packed-bed reactors used for the decomposition of methane in nitrogen and air plasmas,[104] the decomposition of butane in dry and humid nitrogen and air streams,[105] the decomposition of volatile organic compounds,[106,107] the oxidative coupling of methane,[108] partial oxidation of methane,[109] and for the total oxidation of methane[110] showing some promising results. As catalyst support, $BaTiO_3$ showed to suppress the carbon deposition for the low temperature dry methane reforming,[111] and for the partial oxidation of methane[112] when $Ni/BaTiO_3$ was employed as catalyst. In addition, $BaTiO_3$ was also employed as anode for the SOFC exhibiting higher resistance against carbon deposition, better electrochemical performance and much higher stability during long term operation than undoped $SrTiO_3$ and $La_2Ti_2O_7$ anodes.[94] What is more, in the presence 5000 ppm H_2S containing fuels, the power density of the SOFC using $BaTiO_3$ anode increases ca. three and six times for H_2 and CH_4 fuel, respectively. This increment was hypothesized due to the presence of sulfur at the surface as has been revealed by the X-ray photoelectron spectroscopy (XPS) measurement, however up to these days the effect of sulfur has not been elucidated. The oxidation of CH_4 has been suggested to be promoted in the presence of up to 5000 ppm H_2S when $Sr_{0.6}La_{0.4}TiO_3$/YSZ was used as anode.[113] The presence of H_2S led to an improved performance of an SOFC fueled with CH_4 containing 5000 ppm H_2S and $La_{0.4}Sr_{0.6}Ba_{0.1}TiO_{3-\delta}$ was used as anode,[114] however the mechanism for this enhancement is also not yet clarified. Although, theoretical studies performing density functional theory (DFT) calculations have been useful to elucidate and to confirm experimental results, studies focused on the interaction and possible reaction mechanisms of different fuels on perovskite materials when employed as SOFC anodes are lacking.

1.2 POLYMER ELECTROLYTE FUEL CELLS

PEFCs have been broadly researched as technologies for power sources in the transportation sector, for portable technologies, and residential co-generation systems due to their environmental friendly operation and high energy conversion efficiency.[115-120] However, several long-standing issues related to high cost, unreliable performance and low durability are still a major impediment for the large scale commercialization.[115,116,118,119,121-124]

The core component of the PEFC is the membrane, which works as the conductor for protons, as separator for the reactant gases, and as electronic insulator to avoid the transport of electrons.[125,126] Additionally, the PEFC consists of two porous electrodes composed of a gas diffusion layer and a catalyst layer fitted between two bipolar plates that act as current collectors and incorporating the gas channels. A schematic drawing of the PEFC is shown in Figure 1-4.

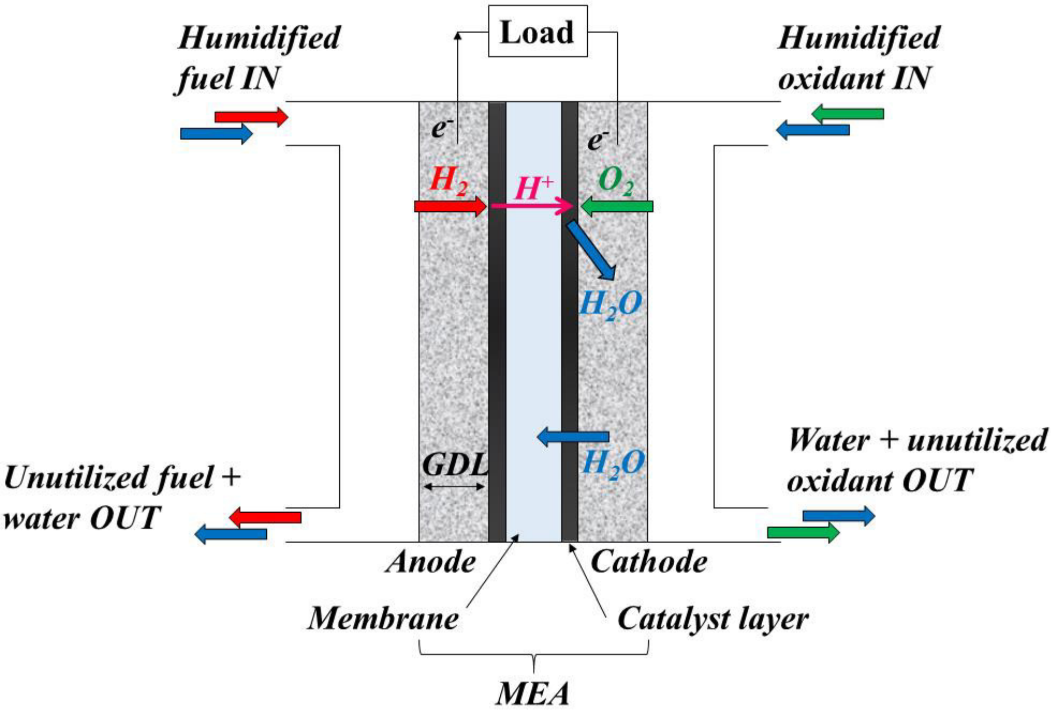

Figure 1-4. Schematic drawing of the PEFC.

The catalyst layer consists of catalyst particles, ionomer and pore spaces which form a TPB where electrons, protons and reactant gases meet and the electrochemical reaction takes place. A schematic depiction of the TPB is shown in Figure 1-5.

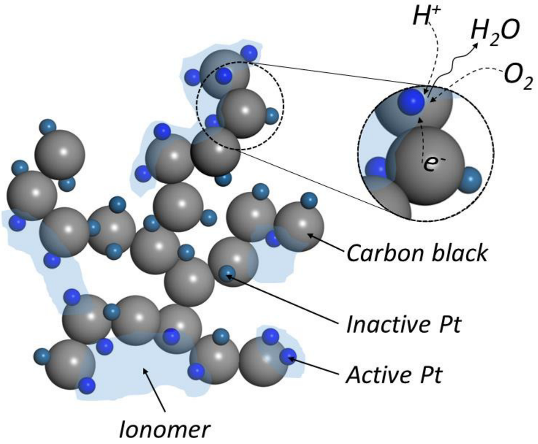

Figure 1-5. Schematic drawing of the microstructure of the cathode's TPB

The hydrogen oxidation reaction occurs at the anode side where the molecule dissociates into protons and electrons, as shown in equation 1-7. The protons migrate to the cathode side via the electrolyte membrane, and the electrons flow around the external circuit generating electricity. The protons and electrons combine at the cathode side to reduce the oxygen producing water, as shown in equation 1-8.

Anode: $$2H_2 \rightarrow 4H^+ + 4e^-, \tag{1-7}$$

Cathode: $$O_2 + 4H^+ + 4e^- \rightarrow 2H_2O, \tag{1-8}$$

Pt and Pt-based alloys are the most commonly used catalysts in PEFC, due to their high electrocatalytic performance.[127-137] However, the scarcity of Pt and its high cost claimed for an immediate reduction of the Pt usage.[118-121,124-126,138-141] In the latest generations of PEFC electrodes, Pt-nanoparticles are uniformly dispersed on carbon support to maximize the active surface area, stabilizing the catalyst making against agglomeration, and increasing the electronic conductivity.[120,122,139-142] However due to the severe conditions at the cathode side during operation; relatively high temperature, high potential, acidic and humid conditions, degradation of the cathode catalyst layer occurs.[139,143-145]

1.2.1 Degradation of the catalyst layer. The degradation of the cathodic electrocatalyst is tightly linked to four main processes that affect to Pt and Pt-alloys supported on carbon-based materials. In Figure 1-6 a schematic drawing of the degradation processes is shown.

1.2.1.1 Carbon corrosion. The performance losses of a PEFC are greatly caused by the degradation of the carbon support. Severe corrosion occurs at the cathode catalyst layer on the long term because thermodynamically carbon can be electrochemically oxidized to CO_2 at low potentials, leading to performance losses in the fuel cell. Carbon corrosion reactions leading to the formation of CO_2 and CO are shown in the following equations:[139,144-146]

$$C + 2H_2O \rightarrow CO_2 + 4H^+ + 4e^- \; E_0 = 0.207\,V\,vs\,RHE\,at\,298\,K, \qquad (1\text{-}9)$$

$$C + H_2O \rightarrow CO + 2H^+ + 2e^- \; E_0 = 0.518\,V\,vs\,RHE\,at\,298\,K, \qquad (1\text{-}10)$$

Although, carbon thermodynamically can be oxidized at potentials higher than 0.20 V vs. the reversible hydrogen electrode (RHE). The latter reaction is considered to proceed reasonably slow at temperatures below 398 K and below 1.0 V vs. RHE.[147-149] However, at high potential values that occur during start/stop or fuel starvation conditions rapid and significant carbon weight loss has been observed.[150,151] The corrosion of carbon induces losses in the electrochemical surface area (ECSA), following the detachment/agglomeration of the metal nanoparticles as the amount of carbon decreased after the carbon oxidation reaction.[144,146] Additionally, the water management of the whole membrane-electrode assembly is affected by the presence of oxygen containing groups, which decrease the hydrophobicity of the catalyst layer.[152] Losses in the porosity of the catalyst layer as a result of changes in the carbon microstructure hinders the mass-transport of gas reactants to the active sites and the water removal from the electrolyte.[140] It was reported that Pt catalyzes the oxidation of carbon.[153,152]

1.2.1.2 Crystallite migration and agglomeration. Carbon corrosion also plays a negative effect on the stability of the Pt/C catalyst. The presence of hydrophilic oxygen surface groups promotes carbon corrosion leading to a decrease in the conductivity of the catalyst layer and weakening the interaction between the support and the metal nanoparticles. Over time the corrosion of the carbon support promotes the motion of the metal nanoparticles until their stabilization by collision or agglomeration with other nanoparticles and possibly their detachment from the support.[143,155] This degradation mechanism is influenced by many factors such as: Pt-nanoparticle size,[156] Pt-loading,[157] flatness of the carbon surface[158] and stability of the carbon support.

1.2.1.3 Dissolution/precipitation. The degradation of Pt-nanoparticles is thought to occur via the electrochemical dissolution of its metallic phase,[159,160] formation of Pt complexes and subsequent chemical dissolution,[161] or reduction of the PtO_2.[162] The nanometer-scale of the metal crystallites emphasizes such degradation, smaller nanoparticles corrode more easily into metal ions than larger ones due to their increased fraction of low-coordinated atoms.[122,137,145,146] The migration of Pt-ions towards the neighboring particles and their agglomeration especially in wet operating medium leads to increasing in the average particle size. This mechanism is known as Oswald ripening. This mechanism does not lead to a loss of Pt-mass in the electrodes but to a decrease in the ECSA.

The fate of the dissolved Pt-ions can also lead them to precipitate into the polymer membrane that they contaminate. In the presence of a reducing agent such as H_2 from crossover, the Pt-ions will reduce back to metallic Pt precipitating in a solid band either inside the membrane or at the cathode membrane interface where strongly interact with the sulfonic acid groups of the perfluorosulfonated membrane leading to a decrease of its proton transport properties.[122,145,146]

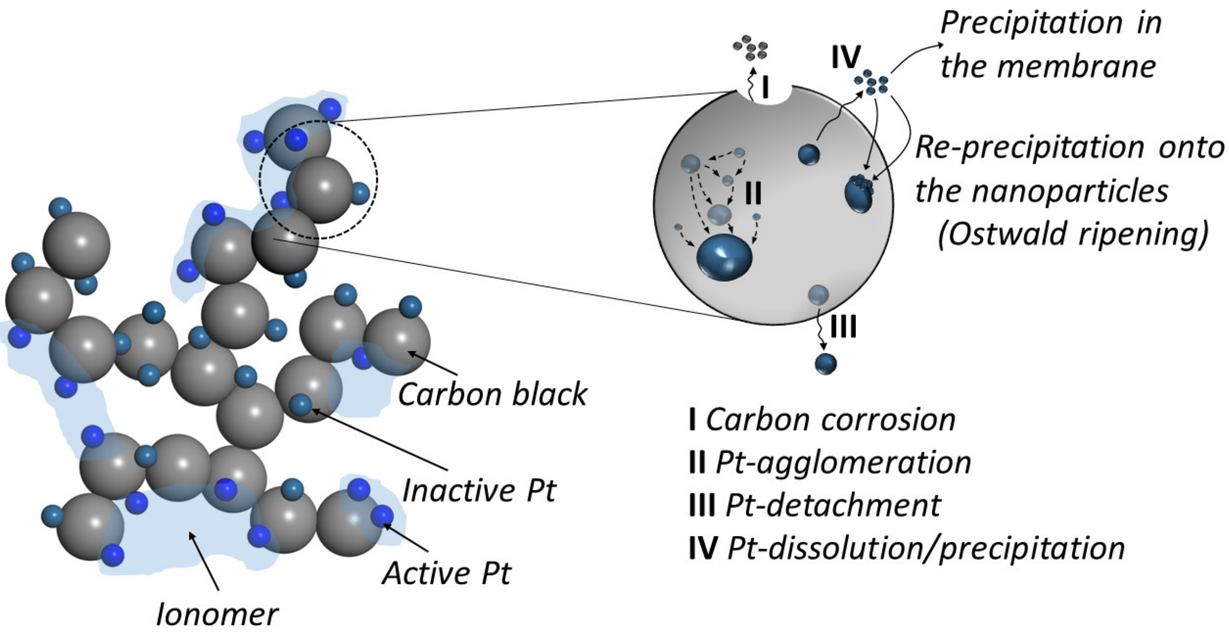

Figure 1-6. Schematic illustration of the degradation mechanism at the catalyst layer. For simplification, the presence of oxygenated species was omitted.

1.2.2 Carbon-based materials as support. Besides the above mentioned degradation processes, carbon blacks are the most commonly used supports for Pt and Pt-alloys due to the high surface area, good electronic properties and low cost.[122,124,141,163,164] In order to improve the durability of Pt/C catalyst, multitude of carbon-based materials other than carbon black have been extensively investigated as supports for the PEFC catalysts such as single[165,166] and multiple wall nanotubes,[167] highly tailored graphitic nanofibers,[168] carbon nanofibers,[169] boron doped diamonds,[170,171] graphene and graphene sheets.[172-174] Although, using different carbon-based support materials improved the anchorage of the metal nanoparticles to the support, the decrease in performance due to losses in the ECSA remain. Although, theoretical approaches cannot fully represent the actual conditions for the degradation of the catalyst layer, the stability of Pt/C systems was studied from a theoretical point of view showing the weak interaction for a Pt-nanoparticle supported on graphene, which was accounted for the Pt-nanoparticle migration and agglomeration that can proceed easily.[125] The magnitude of the interaction between Pt-nanoparticles and graphene depends on the shape of the nanoparticle.[137] Icosahedral nanoparticles exhibited the largest interaction due to easier expansion of the Pt-Pt distance that accommodates at the bridge site of graphene. The weak Pt-Pt interaction of the icosahedral nanoparticles renders this flexibility for atomic rearrangement, however it may make the nanoparticle more prone to dissolution,[137] where atoms at edges are more prone to dissolution than the ones in flat facets.[175] The dissolution process is also size dependent, especially for smaller size Pt-nanoparticles that have a weaker cohesive energy.[175] However, in order to occur the dissolution reaction, the formation of Pt-complexes must occur, where Pt(IV) complexes showed to be more probable to form.[161] Doping graphene with sulfur led to more stable interactions with Pt and enhanced Pt-nanoparticle cohesive energies agreeing with the remarkable electrochemical stability of Pt/S-doped graphene than Pt/carbon black.[119]

1.2.3 Oxides as support material. In the quest of the ideal support material, non-carbonaceous materials have been targeted. Among them, titanium oxides, have been used due to their resistance to corrosion,[176] and low cost.[177] DFT calculations indicated a strong interfacial reaction between Pt and Ti atoms forming a metal-metal bond.[178] Additionally, the presence of oxygen vacancies on TiO_2 not only affected its electrical conductivity[179] but also stabilized the Pt-atom adsorption.[180] Similarly, titanium nitride showed low dissolution rate without any passivation and higher conductivity than carbon black.[181] Moreover, titanium diboride showed to be electrochemically more stable than carbon black.[182] The specific activities of Pt/TiO_2[183] and Pt/$Nb_{0.25}Ti_{0.75}O_2$[184] are lower than Pt/C catalyst. Nevertheless after potential cycling tests, the oxide material systems preserve almost half of their ECSA while less than 10% was retained for the Pt/C catalyst. Similarly, a higher stability was observed for Pt/$Ti_{0.7}Mo_{0.3}O_2$ when compared to Pt/C, which was attributed to strong bonding between Pt-nanoparticles and oxide preventing the agglomeration of the nanoparticles.[185] Furthermore, indium thin oxide displayed increased electrochemical and thermal stability,[186] and faster electron kinetics[187] than carbon black. Tungsten oxide exhibited greater stability, however its catalytic activity and conductivity were not as good as carbon black.[188] Studies of Pt/tungsten carbides reported higher electrocatalytic activity, with higher CO tolerance,[189] however better catalyst dispersion is required as optimal Pt-nanoparticle size was not yet been achieved. This CO anti-poisoning property was attributed to an electron donating effect from tungsten carbide to Pt-atoms avoiding CO adsorption.[190] Similarly, DFT calculations confirmed that for Pt-nanoparticles supported on CeO_2, electron transfer occurs from the nanoparticle to CeO_2 and activated O-atom from CeO_2 to the nanoparticle.[191] Furthermore, a suppression in the activity for O_2 dissociation was reported for a Pt-nanoparticle supported on CeO_2, which was due to hybridization of 5*d* orbitals of Pt-atoms with the 2*p* orbitals of O-atoms in the CeO_2.[192] On the other hand, unreactive supports such as MgO had not influenced the H-atom binding energies of Pd- and Pt-nanoparticles, however it influenced the adsorption site due to an steric repulsion with the H-atom.[193] Thus, selecting a proper support material is crucial as influences the behavior, performance, longevity, and cost effectiveness of the catalyst and of the overall fuel cell.

1.2.3.1 Tin oxide as support material. SnO_2 is an n-type semiconductor and amphoteric oxide widely used in gas sensing devices including low CO concentrations.[194] Furthermore, as support material for Pt, and Pd catalysts strongly promoted the oxidation of traces of CH_4 at low temperatures.[195] Moreover, the oxidation-reduction pretreatment of Pt/SnO_2 catalysts affected the chemical interaction between the metal and the oxide support leading to a weaker adsorption of CO avoiding poisoning during the electrochemical oxidation of hydrogen,[196] similar peculiar catalytic activity due to metal-support interaction was observed for the methane combustion and electrochemical oxidation of CO.[197] Similarly to Pt/TiO_2, Pt/SnO_2 as catalyst indicated an improved durability compared to Pt/C catalysts.[198] However, in its fully oxidized state, SnO_2 possess a poor electronic conductivity limiting its application as electrocatalyst support.[199] Doping SnO_2 with Nb or Sb increased not only the conductivity of the support but also the ECSA and oxygen reduction reaction (ORR) of the metal oxide supported catalyst.[198,200] On one hand the higher ORR activity was attributed to the beneficial metal support interaction,[117] on the other hand, the high activity was linked to the increase in the electronic conductivity.[198] Different dopants concentrations on SnO_2 affects the ORR activity, however no direct relationship with the support conductivity was observed.[201] Thus the controversy between different literature results remains. In order to elucidate the effect of SnO_2 as support material, a systematic study based on the elemental properties and features of the Pt-nanoparticles is required. Literature results from first principles studies of the Pt/SnO_2 are limited, e.g., DFT calculations concluded that larger changes in the Pt-Pt distance are an indication of stronger interaction of Pt/SnO_2 than Pt/graphene.[125] In descended stability order the adsorption of a Pt-nanoparticle was reported for Sb-doped reduced SnO_2,[202] reduced SnO_2[203] and stoichiometric SnO_2. Additionally, at the Pt/SnO_2 interface the H-atom diffusion,[204] and H_2O formation were promoted.[205] For the reasons mentioned above, a detailed analysis based on DFT calculations to rationalize the experimental trends closing the gap between theoretical and experimental work is needed. Additionally, obtaining a molecular-scale picture of the mechanisms underlying the surface chemical reactivity by predicting the performance of a catalyst based on theoretical models is considered the ultimate goal in catalysis.

1.3. OBJECTIVES

1.3.1 General objective

To elucidate the role of metal oxides on the activity of fuel cells electrocatalysts from a theoretical point of view.

To achieve the general objective, the following specific objectives will be completed.

1.3.2 Specific objectives

- To investigate the likelihood of the H_2S, H_2 and CH_4 reaction on $BaTiO_3(001)$ surfaces.
- To quantify, and clarify the effect of the of sulfur on the H_2 oxidation and on the CH_4 sequential decomposition reaction on $BaTiO_3(001)$ surfaces.
- To elucidate the size effect on the geometrical features, electronic and chemical properties of Pt-nanoparticles.
- To clarify the effect of SnO_2 on the geometrical features, electronic and chemical properties, and stability of Pt-nanoparticles.

REFERENCES

(1-1) Hvolbæk, B.; Janssens, T. V. W.; Clausen, B. S.; Falsig, H.; Christensen, C. H.; Nørskov, J. K. Catalytic Activity of Au Nanoparticles. *Nano Today* **2007**, *2* (4), 14–18.

(1-2) Balasanthiran, C.; Hoefelmeyer, J. D. Nanocatalysis: Definition and Case Studies. *Met. Nanoparticles Catal.* **2014**, No. 17, 6–29.

(1-3) Deutschmann, O.; Knözinger, H.; Kochloefl, K.; Turek, T. Heterogeneous Catalysis and Solid Catalysts. *Ullmann's Encycl. Ind. Chem.* **2009**.

(1-4) Talapin, D. V; Shevchenko, E. V. Introduction: Nanoparticle Chemistry. ACS Publications 2016.

(1-5) Dunlap, R. E.; Jorgenson, A. K. Environmental Problems. In *The Wiley-Blackwell Encyclopedia of Globalization*; Ritzer, G., Ed.; John Wiley & Sons, Ltd: Chichester, UK, 2012.

(1-6) Asif, M.; Muneer, T. Energy Supply, Its Demand and Security Issues for Developed and Emerging Economies. *Renew. Sustain. Energy Rev.* **2007**, *11* (7), 1388–1413.

(1-7) Omer, A. M. Energy, Environment and Sustainable Development. *Renew. Sustain. energy Rev.* **2008**, *12* (9), 2265–2300.

(1-8) Wachsman, E. D.; Marlowe, C. A.; Lee, K. T. Role of Solid Oxide Fuel Cells in a Balanced Energy Strategy. *Energy Environ. Sci.* **2012**, *5* (2), 5498–5509.

(1-9) Singhal, S. C. Advances in Solid Oxide Fuel Cell Technology. *Solid state ionics* **2000**, *135* (1–4), 305–313.

(1-10) Singhal, S. C. Solid Oxide Fuel Cells for Power Generation. *Wiley Interdiscip. Rev. Energy Environ.* **2014**, *3* (2), 179–194.

(1-11) Kan, W. H.; Thangadurai, V. Challenges and Prospects of Anodes for Solid Oxide Fuel Cells (SOFCs). *Ionics (Kiel).* **2015**, *21* (2), 301–318.

(1-12) http://www.fuelcelltoday.com/media/1637138/fc_basics_technology_types.pdf, accessed May, 2018

(1-13) Hydrogen Energy Engineering; Sasaki, K., Li, H.-W., Hayashi, A., Yamabe, J., Ogura, T., Lyth, S. M., Eds.; Green Energy and Technology; Springer Japan: Tokyo, 2016.

(1-14) Itoh, N. Fuel Cell Developments in Japan. *J. Power Sources* **1990**, *29* (1–2), 29–35.

(1-15) Maeda, A. Innovation in Fuel Cell Technologies in Japan: Development and Commercialization of Polymer Electrolyte Fuel Cells. Retrieved May 2003, 20, 2005.

(1-16) Nirasawa, H. Current Status of National SOFC Projects in Japan. *ECS Trans.* **2017**, *78* (1), 33–40.

(1-17) https://www.ace.or.jp/web/works/works_0090.html, accessed May, 2018.

(1-18) Wachsman, E. D.; Lee, K. T. Lowering the Temperature of Solid Oxide Fuel Cells. *Science.* **2011**, *334* (6058), 935–939.

(1-19) Cairns, E. J.; Simons, E. L.; Tevebaugh, A. D. Ammonia–Oxygen Fuel Cell. *Nature* **1968**, *217*, 780-781.

(1-20) Sigal, C. T.; Vayenas, C. G. Ammonia Oxidation to Nitric Oxide in a Solid Electrolyte Fuel Cell. *Solid State Ionics* **1981**, *5*, 567-570.

(1-21) Wojcik, A.; Middleton, H.; Damopoulos, I.; Van Herle, J. Ammonia as a Fuel in Solid Oxide Fuel Cells. *J. Power Sources* **2003**, *118*, 342-348.

(1-22) Ma, Q.; Peng, R.; Lin, Y.; Gao, J.; Meng, G. A High-Performance Ammonia-Fueled Solid Oxide Fuel Cell. *J. Power Sources* **2006**, *161*, 95-98.

(1-23) Drewery, M.; Kennedy, E.; Alenazey, F.; Dlugogorski, B.; Stockenhuber, M. The Effect of Synthesis Gas Composition on the Performance of Ni-Based Solid Oxide Fuel Cells. *Chem. Eng. Res. Des.* **2015**, *101*, 22-26.

(1-24) Sun, Y. F.; Li, J. H.; Chuang, K. T.; Luo, J. L. Electrochemical Performance and Carbon Deposition Resistance of Ce-Doped $La_{0.7}Sr_{0.3}Fe_{0.5}Cr_{0.5}O_{3-\delta}$ Anode Materials for Solid Oxide Fuel Cells Fed with Syngas. *J. Power Sources* **2015**, *274*, 483-487.

(1-25) Qin, H.; Zhu, Z.; Liu, Q.; Jing, Y.; Raza, R.; Imran, S.; Singh, M.; Abbas, G.; Zhu, B. Direct Biofuel Low-Temperature Solid Oxide Fuel Cells. *Energy Environ. Sci.* **2011**, *4*, 1273-1276.

(1-26) Kirtley, J. D.; Pomfret, M. B.; Steinhurst, D. A.; Owrutsky C.; Walker, R. A. Toward a Working Mechanism of Fuel Oxidation in SOFCs: *in situ* Optical Studies of Simulated Biogas and Methane. *J. Phys. Chem. C* **2015**, *119*, 12781-12791.

(1-27) Papurello, D.; Lanzini, A.; Tognana, L.; Silvestri, S.; Santarelli, M. Waste to Energy: Exploration of Biogas from Organic Waste in a 500 W_{el} Solid Oxide Fuel Cell (SOFC) Stack. *Energy* **2015**, *85*, 145-158.

(1-28) Tuyen, T. Q.; Kaida, T.; Sakamoto, M.; Sasaki, K.; Shiratori, Y. Effectiveness of Paper-Structured Catalyst for the Operation of Biodiesel-Fueled Solid Oxide Fuel Cell. *J. Power Sources* **2015**, *283*, 320-327.

(1-29) Mehr, A. S.; Mahmoudi, S. M. S.; Yari, M.; Chitsaz, A. Thermodynamic and Exergoeconomic Analysis of Biogas Fed Solid Oxide Fuel Cell Power Plants Emphasizing on Anode and Cathode Recycling: A Comparative Study. *Energy Convers. Manage.* **2015**, *105*, 596-606.

(1-30) Kirtley, J. D.; Pomfret, M. B.; Steinhurst D. A.; Owrutsky, J. C.; Walker, R. A. In Operando Optical Studies of SOFCs Operating with Butanol. *ECS Trans.* **2015**, *68*, 1091-1102.

(1-31) Slinn, M.; Kendall, K.; Mallon, C.; Andrews, J. Steam Reforming of Biodiesel By-Product to Make Renewable Hydrogen. *Bioresour. Technol.* **2008**, *99*, 5851-5858.

(1-32) Sengodan, S.; Choi, S.; Jun, A.; Shin, T. H.; Ju, H. Y.; Shin, J.; Irvine, J. T. S.; Kim, G. Layered Oxygen-Deficient Double Perovskite as an Efficient and Stable Anode for Direct Hydrocarbon Solid Oxide Fuel Cells. *Nat. Mater.* **2015**, *14*, 205-209.

(1-33) Yang, C.; Li, J.; Lin, Y.; Liu, J.; Chen, F.; Liu, M. In Situ Fabrication of CoFe Alloy Nanoparticles Structured $(Pr_{0.4}Sr_{0.6})_3(Fe_{0.85}Nb_{0.15})_2O_7$ Ceramic Anode for Direct Hydrocarbons Solid Oxide Fuel Cells. *Nano Energy* **2015**, *11*, 704-710.

(1-34) Aliotta, C.; Liotta, L. F.; Deganello, F.; La Parola, V.; Martorana, A. Direct Methane Oxidation on $La_{1-x}Sr_xCr_{1-y}Fe_yO_{3-\delta}$ Perovskite-Type Oxides as Potential Anode for Intermediate Temperature Solid Oxide Fuel Cells. *Appl. Catal., B* **2016**, *180*, 424-433.

(1-35) Farrell, B.; Linic, S. Direct Electrochemical Oxidation of Ethanol on SOFCs: Improved Carbon Tolerance of Ni Anode by Alloying. *Appl. Catal., B* **2016**, *183*, 386-393.

(1-36) Chick, L.; Weimar, M.; Whyatt, G.; Powell, M. The Case for Natural Gas Fueled Solid Oxide Fuel Cell Power Systems for Distributed Generation. *Fuel Cells* **2015**, *15*, 49-60.

(1-37) Cai, W.; Zhou, Q.; Xie, Y.; Liu, J. A Facile Method of Preparing Fe-Loaded Activated Carbon Fuel for Direct Carbon Solid Oxide Fuel Cells. *Fuel* **2015**, *159*, 887-893.

(1-38) Jiao, Y.; Tian, W.; Chen, H.; Shi, H.; Yang, B.; Li, C.; Shao, Z.; Zhu, Z.; Li, S. D. In Situ Catalyzed Boudouard Reaction of Coal Char for Solid Oxide-Based Carbon Fuel Cells with Improved Performance. *Appl. Energy* **2015**, *141*, 200-208.

(1-39) Calise, F.; d'Accadia, M. D.; Palombo, A.; Vanoli, L. Simulation and Exergy Analysis of a Hybrid Solid Oxide Fuel Cell (SOFC)–gas Turbine System. *Energy* **2006**, *31* (15), 3278–3299.

(1-40) Minh, N. Q. System Technology for Solid Oxide Fuel Cells. In *Fuel Cell Science and Engineering*; Stolten, D., Emonts, B., Eds.; Wiley-VCH Verlag GmbH & Co. KGaA: Weinheim, Germany, 2012; pp 963–1010.

(1-41) Zhang, X.; Chan, S. H.; Li, G.; Ho, H. K.; Li, J.; Feng, Z. A Review of Integration Strategies for Solid Oxide Fuel Cells. *J. Power Sources* **2010**, *195* (3), 685–702.

(1-42) Choudhury, A.; Chandra, H.; Arora, A. Application of Solid Oxide Fuel Cell Technology for Power Generation—A Review. *Renew. Sustain. Energy Rev.* **2013**, *20*, 430–442

(1-43) Hsiao, Y. C.; Selman, J. R. The Degradation of SOFC Electrodes. *Solid State Ionics* **1997**, *98* (1–2), 33–38.

(1-44) Yokokawa, H. Overview of Intermediate-Temperature Solid Oxide Fuel Cells. In *Perovskite Oxide for Solid Oxide Fuel Cells*; Springer, 2009; pp 17–43.

(1-45) Tarancón, A. Strategies for Lowering Solid Oxide Fuel Cells Operating Temperature. *Energies* **2009**, *2* (4), 1130–1150

(1-46) Lohsoontorn, P.; Brett, D. J. L.; Brandon, N. P. Thermodynamic Predictions of the Impact of Fuel Composition on the Propensity of Sulphur to Interact with Ni and Ceria-Based Anodes for Solid Oxide Fuel Cells. *J. Power Sources* **2008**, *175* (1), 60–67.

(1-47) Atkinson, A.; Barnett, S.; Gorte, R. J.; Irvine, J. T. S.; McEvoy, A. J.; Mogensen, M.; Singhal, S. C.; Vohs, J. Advanced Anodes for High-Temperature Fuel Cells. *Nat. Mater.* **2004**, *3* (1), 17.

(1-48) Boukamp, B. A. Fuel Cells: The Amazing Perovskite Anode. *Nat. Mater.* **2003**, *2* (5), 294.

(1-49) Tao, S.; Irvine, J. T. S. A Redox-Stable Efficient Anode for Solid-Oxide Fuel Cells. *Nat. Mater.* **2003**, *2* (5), 320.

(1-50) Roushanafshar, M.; Luo, J.-L.; Vincent, A. L.; Chuang, K. T.; Sanger, A. R. Effect of Hydrogen Sulfide Inclusion in Syngas Feed on the Electrocatalytic Activity of LST-YDC Composite Anodes for High Temperature SOFC Applications. *Int. J. Hydrogen Energy* **2012**, *37* (9), 7762–7770.

(1-51) Hagen, A.; Rasmussen, J. F. B.; Thydén, K. Durability of Solid Oxide Fuel Cells Using Sulfur Containing Fuels. *J. Power Sources* **2011**, *196* (17), 7271–7276.

(1-52) Spivey, J. J. Deactivation of Reforming Catalysts. In *Fuel Cells: Technologies for Fuel Processing*; Shekhawat, D., Spivey, J. J., Berry, D. A., Eds.; Elsevier: Oxford, UK, 2011; pp. 285–315.

(1-53) Chen, T.; Wang, W. G.; Miao, H.; Li, T.; Xu, C. Evaluation of Carbon Deposition Behavior on the Nickel/Yttrium-Stabilized Zirconia Anode-Supported Fuel Cell Fueled with Simulated Syngas. *J. Power Sources* **2011**, *196* (5), 2461–2468.

(1-54) Yokokawa, H.; Tu, H.; Iwanschitz, B.; Mai, A. Fundamental Mechanisms Limiting Solid Oxide Fuel Cell Durability. *J. Power Sources* **2008**, *182* (2), 400–412.

(1-55) Argyle, M. D.; Bartholomew, C. H. Heterogeneous Catalyst Deactivation and Regeneration: A Review. *Catalysts* **2015**, *5* (1), 145–269.

(1-56) Sasaki, K.; Haga, K.; Yoshizumi, T.; Minematsu, D.; Yuki, E.; Liu, R.; Uryu, C.; Oshima, T.; Ogura, T.; Shiratori, Y. Chemical Durability of Solid Oxide Fuel Cells: Influence of Impurities on Long-Term Performance. *J. Power Sources* **2011**, *196* (22), 9130–9140.

(1-57) Boldrin, P.; Ruiz-Trejo, E.; Mermelstein, J.; Bermúdez Menéndez, J. M.; Ramírez Reina, T.; Brandon, N. P. Strategies for Carbon and Sulfur Tolerant Solid Oxide Fuel Cell Materials, Incorporating Lessons from Heterogeneous Catalysis. *Chem. Rev.* **2016**, *116* (22), 13633–13684.

(1-58) Zeng, Z. H.; Björketun, M. E.; Ebbesen, S.; Mogensen, M. B.; Rossmeisl, J. Origin of Electrolyte-Dopant Dependent Sulfur Poisoning of SOFC Anodes. *Phys. Chem. Chem. Phys.* **2013**, *15*, 6769-6772.

(1-59) Matsuzaki, Y. The Poisoning Effect of Sulfur-Containing Impurity Gas on a SOFC Anode: Part I. Dependence on Temperature, Time, and Impurity Concentration. *Solid State Ionics* **2000**, *132* (3–4), 261–269.

(1-60) Haga, K.; Adachi, S.; Shiratori, Y.; Ito, K.; Sasaki, K. Poisoning of SOFC Anodes by Various Fuel Impurities. *Solid State Ionics* **2008**, *179*, 1427-1431.

(1-61) Yoshizumi, T.; Taniguchi, S.; Shiratori, Y.; Sasaki, K. Sulfur Poisoning of SOFCs: Voltage Oscillation and Ni Oxidation. *J. Electrochem. Soc.* **2012**, *159*, F693-F701.

(1-62) Alfonso, D. R. First-Principles Studies of H_2S Adsorption and Dissociation on Metal Surfaces. *Surf. Sci.* **2008**, *602*, 2758-2768.

(1-63) Danilovic, N.; Luo, J.-L.; Chuang, K. T.; Sanger, A. R. Effect of Substitution with Cr^{3+} and Addition of Ni on the Physical and Electrochemical Properties of $Ce_{0.9}Sr_{0.1}VO_3$ as a H_2S-Active Anode for Solid Oxide Fuel Cells. *J. Power Sources* **2009**, *194* (1), 252–262.

(1-64) Bartholomew, C. H. Mechanisms of Catalyst Deactivation. *Appl. Catal. A Gen.* **2001**, *212* (1–2), 17–60.

(1-65) Rostrup-Nielsen, J. R.; Sehested, J.; Nørskov, J. K. Hydrogen and Synthesis Gas by Steam- and CO_2 Reforming. **2002**.

(1-66) Kim, J.-H.; Suh, D. J.; Park, T.-J.; Kim, K.-L. Effect of Metal Particle Size on Coking during CO_2 Reforming of CH_4 over Ni–alumina Aerogel Catalysts. *Appl. Catal. A Gen.* **2000**, *197* (2), 191–200.

(1-67) Wang, J.-H.; Liu, M. Computational Study of Sulfur–nickel Interactions: A New S–Ni Phase Diagram. *Electrochem. commun.* **2007**, *9* (9), 2212–2217.

(1-68) Choi, Y. M.; Compson, C.; Lin, M. C.; Liu, M. A Mechanistic Study of H_2S Decomposition on Ni-and Cu-Based Anode Surfaces in a Solid Oxide Fuel Cell. *Chem. Phys. Lett.* **2006**, *421* (1–3), 179–183.

(1-69) Cheng, Z.; Wang, J.-H.; Choi, Y.; Yang, L.; Lin, M. C.; Liu, M. From Ni-YSZ to Sulfur-Tolerant Anode Materials for SOFCs: Electrochemical Behavior, in Situ Characterization, Modeling, and Future Perspectives. *Energy Environ. Sci.* **2011**, *4* (11), 4380–4409.

(1-70) Hansen, J. B. Correlating Sulfur Poisoning of SOFC Nickel Anodes by a Temkin Isotherm. *Electrochem. Solid-State Lett.* **2008**, *11* (10), B178–B180.

(1-71) Galea, N. M.; Kadantsev E. U.; Ziegler, T. Studying Reduction in Solid Oxide Fuel Cell Activity with Density Functional Theory-Effects of Hydrogen Sulfide Adsorption on Nickel Anode Surface. *J. Phys. Chem. C* **2007**, *111*, 14457-14468.

(1-72) Monder, S. D.; Karan, K. Ab Initio Adsorption Thermodynamics of H_2S and H_2 on Ni(111): The Importance of Thermal Corrections and Multiple Reaction Equilibria. *J. Phys. Chem. C* **2010**, 114, 22597−22602

(1-73) Ogura, T.; Ishimoto, T.; Koyama, M. Density Functional Theory Study of Sulfur Poisoning on Nickel Anode in Solid Oxide Fuel Cells: Effects of Surface and Subsurface Sulfur. *J. Chem. Eng. Jpn.* **2014**, 47, 793−800.

(1-74) Choi, Y. M.; Compson, C.; Lin, M.-C.; Liu, M. Ab Initio Analysis of Sulfur Tolerance of Ni, Cu, and Ni–Cu Alloys for Solid Oxide Fuel Cells. *J. Alloys Compd.* **2007**, *427* (1–2), 25–29.

(1-75) Grgicak, C. M.; Pakulska, M. M.; O'Brien, J. S.; Giorgi, J. B. Synergistic Effects of $Ni_{1-x}Co_x$–YSZ and $Ni_{1-x}Cu_x$–YSZ Alloyed Cermet SOFC Anodes for Oxidation of Hydrogen and Methane Fuels Containing H_2S. *J. Power Sources* **2008**, *183* (1), 26–33.

(1-76) Kim, M. S.; Rodriguez, N. M.; Baker, R. T. K. The Interplay between Sulfur Adsorption and Carbon Deposition on Cobalt Catalysts. *J. Catal.* **1993**, *143* (2), 449–463.

(1-77) Rostrup-Nielsen, J. R. Sulfur-Passivated Nickel Catalysts for Carbon-Free Steam Reforming of Methane. *J. Catal.* **1984**, *85* (1), 31–43.

(1-78) Hepola, J.; Simell, P. Sulphur Poisoning of Nickel-Based Hot Gas Cleaning Catalysts in Synthetic Gasification Gas: II. Chemisorption of Hydrogen Sulphide. *Appl. Catal. B Environ.* **1997**, *14* (3–4), 305–321.

(1-79) Rostrup-Nielsen, J. R.; Alstrup, I. B. Ensemble Control by Sulfur Poisoning of Nickel Catalysts for Steam Reforming. In Studies in Surface Science and Catalysis; Elsevier, 1988; Vol. 38, pp 725–732.

(1-80) Owens, W. T.; Rodriguez, N. M.; Baker, R. T. K. Effect of Sulfur on the Interaction of Nickel with Ethylene. *Catal. Today* **1994**, *21* (1), 3–22.

(1-81) Malzbender, J.; Wakui, T.; Steinbrech, R. W. Curvature of Planar Solid Oxide Fuel Cells during Sealing and Cooling of Stacks. *Fuel Cells* **2006**, *6* (2), 123–129.

(1-82) Howell, T. G.; Kuhnell, C. P.; Reitz, T. L.; Sukeshini, A. M.; Singh, R. N. A_2MgMoO_6 (A= Sr, Ba) for Use as Sulfur Tolerant Anodes. *J. Power Sources* **2013**, *231*, 279–284.

(1-83) Nowick, A. S.; Liang, K. C. Effect of Non-Stoichiometry on the Protonic and Oxygen-Ionic Conductivity of $Sr_2(ScNb)O_6$: A Complex Perovskite. *Solid State Ionics* **2000**, *129* (1–4), 201–207.

(1-84) Yang, L.; Wang, S.; Blinn, K.; Liu, M.; Liu, Z.; Cheng, Z.; Liu, M. Enhanced Sulfur and Coking Tolerance of a Mixed Ion Conductor for SOFCs: $BaZr_{0.1}Ce_{0.7}Y_{0.2-x}Yb_xO_{3-\delta}$. *Science* **2009**, *326* (5949), 126–129.

(1-85) Ruiz-Morales, J. C.; Canales-Vázquez, J.; Savaniu, C.; Marrero-López, D.; Zhou, W.; Irvine, J. T. S. Disruption of Extended Defects in Solid Oxide Fuel Cell Anodes for Methane Oxidation. *Nature* **2006**, *439* (7076), 568.

(1-86) Liu, M.; Lynch, M. E.; Blinn, K.; Alamgir, F. M.; Choi, Y. Rational SOFC Material Design: New Advances and Tools. *Mater. Today* **2011**, *14* (11), 534–546.

(1-87) Gong, M.; Liu, X.; Trembly, J.; Johnson, C. Sulfur-Tolerant Anode Materials for Solid Oxide Fuel Cell Application. *J. Power Sources* **2007**, *168* (2), 289–298.

(1-88) Zhu, W. Z.; Deevi, S. C. A Review on the Status of Anode Materials for Solid Oxide Fuel Cells. *Mater. Sci. Eng. A* **2003**, *362* (1–2), 228–239.

(1-89) Fergus, J. W. Oxide Anode Materials for Solid Oxide Fuel Cells. *Solid State Ionics* **2006**, *177* (17–18), 1529–1541.

(1-90) de Larramendi, I. R.; Ortiz-Vitoriano, N.; Dzul-Bautista, I. B.; Rojo, T. Designing Perovskite Oxides for Solid Oxide Fuel Cells. In *Perovskite Materials-Synthesis, Characterisation, Properties, and Applications*; InTech, 2016.

(1-91) Slater, P. R.; Fagg, D. P.; Irvine, J. T. S. Synthesis and Electrical Characterisation of Doped Perovskite Titanates as Potential Anode Materials for Solid Oxide Fuel Cells. *J. Mater. Chem.* **1997**, *7* (12), 2495–2498.

(1-92) La Rosa, D.; Sin, A.; Faro, M. Lo; Monforte, G.; Antonucci, V.; Arico, A. S. Mitigation of Carbon Deposits Formation in Intermediate Temperature Solid Oxide Fuel

Cells Fed with Dry Methane by Anode Doping with Barium. *J. Power Sources* **2009**, *193* (1), 160–164.

(1-93) Li, J.; Luo, J.-L.; Chuang, K. T.; Sanger, A. R. Chemical Stability of Y-Doped Ba(Ce, Zr)O_3 Perovskites in H_2S-Containing H_2. *Electrochim. Acta* **2008**, *53* (10), 3701–3707.

(1-94) Li, J.-H.; Fu, X.-Z.; Luo, J.-L.; Chuang, K. T.; Sanger, A. R. Application of $BaTiO_3$ as Anode Materials for H_2S-Containing CH_4 Fueled Solid Oxide Fuel Cells. *J. Power Sources* **2012**, *213*, 69–77.

(1-95) Vincent, A.; Luo, J.-L.; Chuang, K. T.; Sanger, A. R. Effect of Ba Doping on Performance of LST as Anode in Solid Oxide Fuel Cells. *J. Power Sources* **2010**, *195* (3), 769–774.

(1-96) Aguilar, L.; Zha, S.; Cheng, Z.; Winnick, J.; Liu, M. A Solid Oxide Fuel Cell Operating on Hydrogen Sulfide (H_2S) and Sulfur-Containing Fuels. *J. Power Sources* **2004**, *135* (1–2), 17–24.

(1-97) Huang, Y.-H.; Dass, R. I.; Xing, Z.-L.; Goodenough, J. B. Double Perovskites as Anode Materials for Solid-Oxide Fuel Cells. *Science (80-.).* **2006**, *312* (5771), 254–257.

(1-98) Mukundan, R.; Brosha, E. L.; Garzon, F. H. Sulfur Tolerant Anodes for SOFCs. *Electrochem. Solid-State Lett.* **2004**, *7* (1), A5–A7.

(1-99) Cheng, Z.; Zha, S.; Aguilar, L.; Liu, M. Chemical, Electrical, and Thermal Properties of Strontium Doped Lanthanum Vanadate. *Solid State Ionics* **2005**, *176* (23–24), 1921–1928.

(1-100) Choi, K. J. Enhancement of Ferroelectricity in Strained BaTiO3 Thin Films. *Science.* **2004**, *306* (5698), 1005–1009.

(1-101) Heeg, T.; Wagner, M.; Schubert, J.; Buchal, C.; Boese, M.; Luysberg, M.; Cicerrella, E.; Freeouf, J. L. Rare-Earth Scandate Single- and Multi-Layer Thin Films as Alternative Gate Oxides for Microelectronic Applications. *Microelectron. Eng.* **2005**, *80*, 150–153.

(1-102) Li, X.; Wang, G.; Cheng, Y. Preparation and Characteristics of Fe_3O_4-$BaTiO_3$ Heterostructural Nanocomposite as Photocatalyst. *Res. Chem. Intermed.* **2015**, *41* (5), 3031–3039.

(1-103) Ogata, A.; Mizuno, K.; Kushiyama, S.; Yamamoto, T. Methane Decomposition in a Barium Titanate Packed-Bed Nonthermal Plasma Reactor. *Plasma Chem. plasma Process.* **1998**, *18* (3), 363–373.

(1-104) Futamura, S.; Zhang, A. H.; Yamamoto, T. The Dependence of Nonthermal Plasma Behavior of VOCs on Their Chemical Structures. *J. Electrostat.* **1997**, *42* (1–2), 51–62.

(1-105) Prantsidou, M.; Whitehead, J. C. The Chemistry of Gaseous Dodecane Degradation in a $BaTiO_3$ Packed-Bed Plasma Reactor. *Plasma Chem. Plasma Process.* **2015**, *35* (1), 159–172.

(1-106) Kim, H.-H.; Kobara, H.; Ogata, A.; Futamura, S. Comparative Assessment of Different Nonthermal Plasma Reactors on Energy Efficiency and Aerosol Formation from the Decomposition of Gas-Phase Benzene. *IEEE Trans. Ind. Appl.* **2005**, *41* (1), 206–214.

(1-107) Pringle, K. J.; Whitehead, J. C.; Wilman, J. J.; Wu, J. The Chemistry of Methane Remediation by a Non- thermal Atmospheric Pressure Plasma. *Plasma Chem. plasma Process.* **2004**, *24* (3), 421–434.

(1-108) Teymouri, M.; Bagherzadeh, E.; Petit, C.; Rehspringer, J. L.; Libs, S.; Kiennemann, A. Reactivity of Perovskites on Oxidative Coupling of Methane. *J. Mater. Sci.* **1995**, *30* (11), 3005–3009.

(1-109) Guo, C.; Zhang, J.; Li, W.; Zhang, P.; Wang, Y. Partial Oxidation of Methane to Syngas over $BaTi_{1-x}Ti_xO_3$ Catalysts. *Catal. today* **2004**, *98* (4), 583–587.

(1-110) Popescu, I.; Urda, A.; Yuzhakova, T.; Marcu, I.-C.; Kovacs, J.; Sandulescu, I. $BaTiO_3$ and $PbTiO_3$ Perovskite as Catalysts for Methane Combustion. *Comptes Rendus Chim.* **2009**, *12* (9), 1072–1078.

(1-111) Li, X.; Hu, Q.; Yang, Y.; Wang, Y.; He, F. Studies on Stability and Coking Resistance of $Ni/BaTiO_3–Al_2O_3$ Catalysts for Lower Temperature Dry Reforming of Methane (LTDRM). *Appl. Catal. A Gen.* **2012**, *413*, 163–169.

(1-112) Shiozaki, R.; Andersen, A. G.; Hayakawa, T.; Hamakawa, S.; Suzuki, K.; Shimizu, M.; Takehira, K. Partial Oxidation of Methane over a $Ni/BaTiO_3$ Catalyst Prepared by Solid Phase Crystallization. *J. Chem. Soc. Faraday Trans.* **1997**, *93* (17), 3235–3242.

(1-113) Mukundan, R.; Brosha, E. L.; Garzon, F. H. Sulfur Tolerant Anodes for SOFCs. *Electrochem. Solid-State Lett.* **2004**, *7* (1), A5–A7.

(1-114) Vincent, A. L.; Luo, J.-L.; Chuang, K. T.; Sanger, A. R. Promotion of Activation of CH_4 by H_2S in Oxidation of Sour Gas over Sulfur Tolerant SOFC Anode Catalysts. *Appl. Catal. B Environ.* **2011**, *106* (1–2), 114–122.

(1-115) Ishimoto, T.; Koyama, M. A Review of Molecular-Level Mechanism of Membrane Degradation in the Polymer Electrolyte Fuel Cell. *Membranes* **2012**, *2* (3), 395–414.

(1-116) Seo, J. K.; Khetan, A.; Seo, M. H.; Kim, H.; Han, B. First-Principles Thermodynamic Study of the Electrochemical Stability of Pt Nanoparticles in Fuel Cell Applications. *J. Power Sources* **2013**, *238*, 137–143.

(1-117) Kakinuma, K.; Chino, Y.; Senoo, Y.; Uchida, M.; Kamino, T.; Uchida, H.; Deki, S.; Watanabe, M. Characterization of Pt Catalysts on Nb-Doped and Sb-Doped $SnO_{2-\delta}$ Support Materials with Aggregated Structure by Rotating Disk Electrode and Fuel Cell Measurements. *Electrochim. Acta* **2013**, *110*, 316–324.

(1-118) De Lile, J. R.; Zhou, S. Theoretical Modeling of the PEMFC Catalyst Layer: A Review of Atomistic Methods. *Electrochim. Acta* **2015**, *177*, 4–20.

(1-119) Higgins, D.; Hoque, M. A.; Seo, M. H.; Wang, R.; Hassan, F.; Choi, J. Y.; Pritzker, M.; Yu, A.; Zhang, J.; Chen, Z. Development and Simulation of Sulfur-Doped Graphene Supported Platinum with Exemplary Stability and Activity towards Oxygen Reduction. *Adv. Funct. Mater.* **2014**, *24*, 4325–4336.

(1-120) Chino, Y.; Taniguchi, K.; Senoo, Y.; Kakinuma, K.; Hara, M.; Watanabe, M.; Uchida, M. Effect of Added Graphitized CB on Both Performance and Durability of Pt/Nb-SnO_2 Cathodes for PEFCs. *J. Electrochem. Soc.* **2015**, *162* (7), F736–F743.

(1-121) Knights, S. D.; Colbow, K. M.; St-Pierre, J.; Wilkinson, D. P. Aging Mechanisms and Lifetime of PEFC and DMFC. *J. Power Sources* **2004**, *127* (1–2), 127–134.

(1-122) Yousfi-Steiner, N.; Moçotéguy, P.; Candusso, D.; Hissel, D. A Review on Polymer Electrolyte Membrane Fuel Cell Catalyst Degradation and Starvation Issues: Causes, Consequences and Diagnostic for Mitigation. *J. Power Sources* **2009**, *194* (1), 130–145.

(1-123) Peighambardoust, S. J.; Rowshanzamir, S.; Amjadi, M. Review of the Proton Exchange Membranes for Fuel Cell Applications. *Int. J. Hydrogen Energy* **2010**, *35* (17), 9349–9384.

(1-124) Sharma, S.; Pollet, B. G. Support Materials for PEMFC and DMFC Electrocatalysts—a Review. *J. Power Sources* **2012**, *208*, 96–119.

(1-125) Daio, T.; Staykov, A.; Guo, L.; Liu, J.; Tanaka, M.; Lyth, S. M.; Sasaki, K. Lattice Strain Mapping of Platinum Nanoparticles on Carbon and SnO_2 Supports. *Sci. Rep.* **2015**, *5*, 13126.

(1-126) Escaño, M. C. S. First-Principles Calculations of the Dissolution and Coalescence Properties of Pt Nanoparticle ORR Catalysts: The Effect of Nanoparticle Shape. *Nano Res.* **2015**, *8* (5), 1689–1697.

(1-127) Fang, B.; Kim, J. H.; Yu, J.-S. Colloid-Imprinted Carbon with Superb Nanostructure as an Efficient Cathode Electrocatalyst Support in Proton Exchange Membrane Fuel Cell. *Electrochem. commun.* **2008**, *10* (4), 659–662.

(1-128) Fang, B.; Kim, J. H.; Lee, C.; Yu, J.-S. Hollow Macroporous Core/Mesoporous Shell Carbon with a Tailored Structure as a Cathode Electrocatalyst Support for Proton Exchange Membrane Fuel Cells. *J. Phys. Chem. C* **2008**, *112* (2), 639–645.

(1-129) Chai, G. S.; Fang, B.; Yu, J.-S. γ-Ray Irradiation as Highly Efficient Approach for Synthesis of Supported High Pt Loading Cathode Catalyst for Application in Direct Methanol Fuel Cell. *Electrochem. commun.* **2008**, *10* (11), 1801–1804.

(1-130) Fang, B.; Kim, J. H.; Kim, M.; Kim, M.; Yu, J.-S. Hierarchical Nanostructured Hollow Spherical Carbon with Mesoporous Shell as a Unique Cathode Catalyst Support in Proton Exchange Membrane Fuel Cell. *Phys. Chem. Chem. Phys.* **2009**, *11* (9), 1380.

(1-131) Kim, J. H.; Fang, B.; Yoon, S. B.; Yu, J.-S. Hollow Core/Mesoporous Shell Carbon Capsule as an Unique Cathode Catalyst Support in Direct Methanol Fuel Cell. *Appl. Catal. B Environ.* **2009**, *88* (3–4), 368–375.

(1-132) Kim, J. H.; Fang, B.; Song, M. Y.; Yu, J.-S. Topological Transformation of Thioether-Bridged Organosilicas into Nanostructured Functional Materials. *Chem. Mater.* **2012**, *24* (12), 2256–2264.

(1-133) Antolini, E. Formation of Carbon-Supported PtM Alloys for Low Temperature Fuel Cells: A Review. *Mater. Chem. Phys.* **2003**, *78* (3), 563–573.

(1-134) Antolini, E. Platinum-Based Ternary Catalysts for Low Temperature Fuel Cells. *Appl. Catal. B Environ.* **2007**, *74* (3–4), 337–350.

(1-135) Srivastava, R.; Mani, P.; Hahn, N.; Strasser, P. Efficient Oxygen Reduction Fuel Cell Electrocatalysis on Voltammetrically Dealloyed Pt–Cu–Co Nanoparticles. *Angew. Chemie Int. Ed.* **2007**, *46* (47), 8988–8991.

(1-136) Strasser, P.; Koh, S.; Greeley, J. Voltammetric Surface Dealloying of Pt Bimetallic Nanoparticles: An Experimental and DFT Computational Analysis. *Phys. Chem. Chem. Phys.* **2008**, *10* (25), 3670.

(1-137) Strasser, P.; Koh, S.; Anniyev, T.; Greeley, J.; More, K.; Yu, C.; Liu, Z.; Kaya, S.; Nordlund, D.; Ogasawara, H.; et al. Lattice-Strain Control of the Activity in Dealloyed Core–shell Fuel Cell Catalysts. *Nat. Chem.* **2010**, *2* (6), 454–460.

(1-138) Stamenkovic, V. R.; Fowler, B.; Mun, B. S.; Wang, G.; Ross, P. N.; Lucas, C. A.; Marković, N. M. Improved Oxygen Reduction Activity on Pt_3Ni (111) via Increased Surface Site Availability. *Science* **2007**, *315* (5811), 493–497.

(1-139) Yu, X.; Ye, S. Recent Advances in Activity and Durability Enhancement of Pt/C Catalytic Cathode in PEMFC: Part I. Physico-Chemical and Electronic Interaction between Pt and Carbon Support, and Activity Enhancement of Pt/C Catalyst. *J. Power Sources* **2007**, *172* (1), 133–144.

(1-140) Verga, L. G.; Aarons, J.; Sarwar, M.; Thompsett, D.; Russell, A. E.; Skylaris, C.-K. Effect of Graphene Support on Large Pt Nanoparticles. *Phys. Chem. Chem. Phys.* **2016**, *18* (48), 32713–32722.

(1-141) Seger, B.; Kamat, P. V. Electrocatalytically Active Graphene-Platinum Nanocomposites. Role of 2-D Carbon Support in PEM Fuel Cells. *J. Phys. Chem. C* **2009**, *113* (19), 7990–7995.

(1-142) Antolini, E. Carbon Supports for Low-Temperature Fuel Cell Catalysts. *Appl. Catal. B Environ.* **2009**, *88* (1–2), 1–24.

(1-143) Wang, J.; Yin, G.; Shao, Y.; Zhang, S.; Wang, Z.; Gao, Y. Effect of Carbon Black Support Corrosion on the Durability of Pt/C Catalyst. *J. Power Sources* **2007**, *171* (2), 331–339.

(1-144) Shao, Y.; Yin, G.; Gao, Y. Understanding and Approaches for the Durability Issues of Pt-Based Catalysts for PEM Fuel Cell. *J. Power Sources* **2007**, *171* (2), 558–566.

(1-145) De Bruijn, F. A.; Dam, V. A. T.; Janssen, G. J. M. Durability and Degradation Issues of PEM Fuel Cell Components. *Fuel cells* **2008**, *8* (1), 3–22.

(1-146) Dubau, L.; Castanheira, L.; Maillard, F.; Chatenet, M.; Lottin, O.; Maranzana, G.; Dillet, J.; Lamibrac, A.; Perrin, J.; Moukheiber, E. A Review of PEM Fuel Cell Durability: Materials Degradation, Local Heterogeneities of Aging and Possible Mitigation Strategies. *Wiley Interdiscip. Rev. Energy Environ.* **2014**, *3* (6), 540–560.

(1-147) Fowler, M.; Amphlett, J. C.; Mann, R. F.; Peppley, B. A.; Roberge, P. R. Issues Associated with Voltage Degradation in a PEMFC. *J. New Mater. Electrochem. Syst.* **2002**, *5* (4), 255–262.

(1-148) Ozouf, G.; Cognard, G.; Maillard, F.; Chatenet, M.; Guétaz, L.; Heitzmann, M.; Jacques, P. A.; Beauger, C. Sb-Doped SnO_2 Aerogels Based Catalysts for Proton Exchange Membrane Fuel Cells: Pt Deposition Routes, Electrocatalytic Activity and Durability. *J. Electrochem. Soc.* **2018**, *165* (6), F3036–F3044.

(1-149) Maillard, F.; Bonnefont, A.; Micoud, F. An EC-FTIR Study on the Catalytic Role of Pt in Carbon Corrosion. *Electrochem. commun.* **2011**, *13* (10), 1109–1111.

(1-150) Linse, N.; Gubler, L.; Scherer, G. G.; Wokaun, A. The Effect of Platinum on Carbon Corrosion Behavior in Polymer Electrolyte Fuel Cells. *Electrochim. Acta* **2011**, *56* (22), 7541–7549.

(1-151) Hong, B. K.; Mandal, P.; Oh, J.-G.; Litster, S. On the Impact of Water Activity on Reversal Tolerant Fuel Cell Anode Performance and Durability. *J. Power Sources* **2016**, *328*, 280–288.

(1-152) Reiser, C. A.; Bregoli, L.; Patterson, T. W.; Yi, J. S.; Yang, J. D.; Perry, M. L.; Jarvi, T. D. A Reverse-Current Decay Mechanism for Fuel Cells. *Electrochem. Solid-State Lett.* **2005**, *8* (6), A273.

(1-153) Siroma, Z.; Ishii, K.; Yasuda, K.; Miyazaki, Y.; Inaba, M.; Tasaka, A. Imaging of Highly Oriented Pyrolytic Graphite Corrosion Accelerated by Pt Particles. *Electrochem. commun.* **2005**, *7* (11), 1153–1156.

(1-154) Li, L.; Xing, Y. Electrochemical Durability of Carbon Nanotubes in Noncatalyzed and Catalyzed Oxidations. *J. Electrochem. Soc.* **2006**, *153* (10), A1823–A1828.

(1-155) Shao, Y.; Yin, G.; Zhang, J.; Gao, Y. Comparative Investigation of the Resistance to Electrochemical Oxidation of Carbon Black and Carbon Nanotubes in Aqueous Sulfuric Acid Solution. *Electrochim. Acta* **2006**, *51* (26), 5853–5857.

(1-156) Chen, J.; Chan, K.-Y. *Size-Dependent Mobility of Platinum Cluster on a Graphite Surface*; 2005; Vol. 31.

(1-157) Zhao, Z.; Dubau, L.; Maillard, F. Evidences of the Migration of Pt Crystallites on High Surface Area Carbon Supports in the Presence of Reducing Molecules. *J. Power Sources* **2012**, *217*, 449–458.

(1-158) Wang, X.; Li, W.; Chen, Z.; Waje, M.; Yan, Y. Durability Investigation of Carbon Nanotube as Catalyst Support for Proton Exchange Membrane Fuel Cell. *J. Power Sources* **2006**, *158* (1), 154–159.

(1-159) Borup, R.; Meyers, J.; Pivovar, B.; Kim, Y. S.; Mukundan, R.; Garland, N.; Myers, D.; Wilson, M.; Garzon, F.; Wood, D.; et al. Scientific Aspects of Polymer Electrolyte Fuel Cell Durability and Degradation. *Chem. Rev.* **2007**, *107* (10), 3904–3951.

(1-160) Rinaldo, S. G.; Stumper, J.; Eikerling, M. Physical Theory of Platinum Nanoparticle Dissolution in Polymer Electrolyte Fuel Cells. *J. Phys. Chem. C* **2010**, *114* (13), 5773–5785.

(1-161) Ishimoto, T.; Ogura, T.; Umeda, M.; Koyama, M. Theoretical Study on Dissolution and Reprecipitation Mechanism of Pt Complex in Pt Electrocatalyst. *J. Phys. Chem. C* **2011**, *115* (7), 3136–3142.

(1-162) Johnson, D. C.; Napp, D. T.; Bruckenstein, S. A Ring-Disk Electrode Study of the Current/Potential Behaviour of Platinum in 1.0 M Sulphuric and 0.1 M Perchloric Acids. *Electrochim. Acta* **1970**, *15* (9), 1493–1509.

(1-163) Park, Y.-C.; Tokiwa, H.; Kakinuma, K.; Watanabe, M.; Uchida, M. Effects of Carbon Supports on Pt Distribution, Ionomer Coverage and Cathode Performance for Polymer Electrolyte Fuel Cells. *J. Power Sources* **2016**, *315*, 179–191.

(1-164) Lázaro, M. J.; Calvillo, L.; Celorrio, V.; Pardo, J. I.; Perathoner, S.; Moliner, R. Study and Application of Vulcan XC-72 in Low Temperature Fuel Cells. In *Carbon Black: Production, Properties and Uses*; Sanders, I. J., Peeten, T. L., Eds.; Nova Science Publishers, Inc., 2011; pp. 41–68.

(1-165) Che, G.; Lakshmi, B. B.; Fisher, E. R.; Martin, C. R. Carbon Nanotubule Membranes for Electrochemical Energy Storage and Production. *Nature* **1998**, *393* (6683), 346.

(1-166) Dudin, P. V; Unwin, P. R.; Macpherson, J. V. Electrochemical Nucleation and Growth of Gold Nanoparticles on Single-Walled Carbon Nanotubes: New Mechanistic Insights. *J. Phys. Chem. C* **2010**, *114* (31), 13241–13248.

(1-167) Park, S.; Shao, Y.; Kou, R.; Viswanathan, V. V; Towne, S. A.; Rieke, P. C.; Liu, J.; Lin, Y.; Wang, Y. Polarization Losses under Accelerated Stress Test Using Multiwalled Carbon Nanotube Supported Pt Catalyst in PEM Fuel Cells. *J. Electrochem. Soc.* **2011**, *158* (3), B297–B302.

(1-168) Bessel, C. A.; Laubernds, K.; Rodriguez, N. M.; Baker, R. T. K. Graphite Nanofibers as an Electrode for Fuel Cell Applications. *J. Phys. Chem. B* **2001**, *105* (6), 1115–1118.

(1-169) Maiyalagan, T. Pt–Ru Nanoparticles Supported PAMAM Dendrimer Functionalized Carbon Nanofiber Composite Catalysts and Their Application to Methanol Oxidation. *J. Solid State Electrochem.* **2009**, *13* (10), 1561–1566.

(1-170) Swain, G. M. The Use of CVD Diamond Thin Films in Electrochemical Systems. *Adv. Mater.* **1994**, *6* (5), 388–392.

(1-171) Xu, J.; Granger, M. C.; Chen, Q.; Strojek, J. W.; Lister, T. E.; Swain, G. M. Peer Reviewed: Boron-Doped Diamond Thin-Film Electrodes. *Anal. Chem.* **1997**, *69* (19), 591A–597A.

(1-172) Guo, S.; Dong, S.; Wang, E. Three-Dimensional Pt-on-Pd Bimetallic Nanodendrites Supported on Graphene Nanosheet: Facile Synthesis and Used as an Advanced Nanoelectrocatalyst for Methanol Oxidation. *ACS Nano* **2009**, *4* (1), 547–555.

(1-173) Qu, L.; Liu, Y.; Baek, J.-B.; Dai, L. Nitrogen-Doped Graphene as Efficient Metal-Free Electrocatalyst for Oxygen Reduction in Fuel Cells. *ACS Nano* **2010**, *4* (3), 1321–1326.

(1-174) Liu, S.; Wang, J.; Zeng, J.; Ou, J.; Li, Z.; Liu, X.; Yang, S. “Green” Electrochemical Synthesis of Pt/graphene Sheet Nanocomposite Film and Its Electrocatalytic Property. *J. Power Sources* **2010**, *195* (15), 4628–4633.

(1-175) Jinnouchi, R.; Toyoda, E.; Hatanaka, T.; Morimoto, Y. First Principles Calculations on Site-Dependent Dissolution Potentials of Supported and Unsupported Pt Particles. *J. Phys. Chem. C* **2010**, *114* (41), 17557–17568.

(1-176) Fovet, Y.; Gal, J.-Y.; Toumelin-Chemla, F. Influence of PH and Fluoride Concentration on Titanium Passivating Layer: Stability of Titanium Dioxide. *Talanta* **2001**, *53* (5), 1053–1063.

(1-177) Leroux, F.; Dewar, P. J.; Intissar, M.; Ouvrard, G.; Nazar, L. F. Study of the Formation of Mesoporous Titania via a Template Approach and of Subsequent Li Insertion. *J. Mater. Chem.* **2002**, *12* (11), 3245–3253.

(1-178) Jiang, D.; Overbury, S. H.; Dai, S. Structures and Energetics of Pt Clusters on TiO 2 : Interplay between Metal–Metal Bonds and Metal–Oxygen Bonds. *J. Phys. Chem. C* **2012**, *116* (41), 21880–21885.

(1-179) Nowotny, M. K.; Bak, T.; Nowotny, J. Electrical Properties and Defect Chemistry of TiO_2 Single Crystal. I. Electrical Conductivity. *J. Phys. Chem. B* **2006**, *110* (33), 16270–16282.

(1-180) Cai, Y.; Bai, Z.; Chintalapati, S.; Zeng, Q.; Feng, Y. P. Transition Metal Atoms Pathways on Rutile TiO_2(110) Surface: Distribution of Ti^{3+} States and Evidence of Enhanced Peripheral Charge Accumulation. *J. Chem. Phys.* **2013**, *138* (15), 154711.

(1-181) Avasarala, B.; Haldar, P. On the Stability of TiN-Based Electrocatalysts for Fuel Cell Applications. *Int. J. Hydrogen Energy* **2011**, *36* (6), 3965‑3974.

(1-182) Yin, S.; Mu, S.; Lv, H.; Cheng, N.; Pan, M.; Fu, Z. A Highly Stable Catalyst for PEM Fuel Cell Based on Durable Titanium Diboride Support and Polymer Stabilization. *Appl. Catal. B Environ.* **2010**, *93* (3‑4), 233‑240.

(1-183) Huang, S.-Y.; Ganesan, P.; Popov, B. N. Titania Supported Platinum Catalyst with High Electrocatalytic Activity and Stability for Polymer Electrolyte Membrane Fuel Cell. *Appl. Catal. B Environ.* **2011**, *102* (1–2), 71–77.

(1-184) Huang, S.-Y.; Ganesan, P.; Popov, B. N. Electrocatalytic Activity and Stability of Niobium-Doped Titanium Oxide Supported Platinum Catalyst for Polymer Electrolyte Membrane Fuel Cells. *Appl. Catal. B Environ.* **2010**, *96* (1–2), 224–231.

(1-185) Ho, V. T. T.; Pan, C.-J.; Rick, J.; Su, W.-N.; Hwang, B.-J. Nanostructured $Ti_{0.7}Mo_{0.3}O_2$ Support Enhances Electron Transfer to Pt: High-Performance Catalyst for Oxygen Reduction Reaction. *J. Am. Chem. Soc.* **2011**, *133* (30), 11716–11724.

(1-186) Chhina, H.; Campbell, S.; Kesler, O. An Oxidation-Resistant Indium Tin Oxide Catalyst Support for Proton Exchange Membrane Fuel Cells. *J. Power Sources* **2006**, *161* (2), 893–900.

(1-187) Park, I.-S.; Lee, E.; Manthiram, A. Electrocatalytic Properties of Indium Tin Oxide-Supported Pt Nanoparticles for Methanol Electro-Oxidation. *J. Electrochem. Soc.* **2010**, *157* (2), B251–B255.

(1-188) Chhina, H.; Campbell, S.; Kesler, O. Ex Situ Evaluation of Tungsten Oxide as a Catalyst Support for PEMFCs. *J. Electrochem. Soc.* **2007**, *154* (6), B533–B539.

(1-189) Fu, Z.; Huang, Q. M.; Xiang, X. D.; Lin, Y. L.; Wu, W.; Hu, S. J.; Li, W. S. Mesoporous Tungsten Carbide-Supported Platinum as Carbon Monoxide-Tolerant Electrocatalyst for Methanol Oxidation. *Int. J. Hydrogen Energy* **2012**, *37* (5), 4704–4709.

(1-190) Cui, G.; Shen, P. K.; Meng, H.; Zhao, J.; Wu, G. Tungsten Carbide as Supports for Pt Electrocatalysts with Improved CO Tolerance in Methanol Oxidation. *J. Power Sources* **2011**, *196* (15), 6125–6130.

(1-191) Vayssilov, G. N.; Lykhach, Y.; Migani, A.; Staudt, T.; Petrova, G. P.; Tsud, N.; Skála, T.; Bruix, A.; Illas, F.; Prince, K. C.; et al. Support Nanostructure Boosts Oxygen Transfer to Catalytically Active Platinum Nanoparticles. *Nat. Mater.* **2011**, *10* (4), 310–315.

(1-192) Nguyen, T. Q.; Escaño, M. C. S.; Nakanishi, H.; Kasai, H.; Maekawa, H.; Osumi, K.; Sato, K. DFT+ U Study on the Oxygen Adsorption and Dissociation on CeO_2-Supported Platinum Cluster. *Appl. Surf. Sci.* **2014**, *288*, 244–250.

(1-193) Kozlov, S. M.; Aleksandrov, H. A.; Neyman, K. M. Adsorbed and Subsurface Absorbed Hydrogen Atoms on Bare and MgO(100)-Supported Pd and Pt Nanoparticles. *J. Phys. Chem. C* **2014**, *118* (28), 15242–15250.

(1-194) Mädler, L.; Sahm, T.; Gurlo, A.; Grunwaldt, J.-D.; Barsan, N.; Weimar, U.; Pratsinis, S. E. Sensing Low Concentrations of CO Using Flame-Spray-Made Pt/SnO_2 Nanoparticles. *J. Nanoparticle Res.* **2006**, *8* (6), 783–796.

(1-195) Roth, D.; Gelin, P.; Tena, E.; Primet, M. Combustion of Methane at Low Temperature over Pd and Pt Catalysts Supported on Al_2O_3, SnO_2 and Al_2O_3-Grafted SnO_2. *Top. Catal.* **2001**, *16* (1–4), 77–82.

(1-196) Baltacioğlu, F. S.; Gülyüz, B.; Aksoylu, A. E.; Oensan, Z. I. Low Temperature CO Oxidation Kinetics over Activated Carbon Supported Pt-SnO_x Catalysts. *Turkish J. Chem.* **2007**, *31* (5), 455–464.

(1-197) Urfels, L.; Gélin, P.; Primet, M.; Tena, E. Complete Oxidation of Methane at Low Temperature over Pt Catalysts Supported on High Surface Area SnO_2. *Top. Catal.* **2004**, *30* (1–4), 427–432.

(1-198) Takasaki, F.; Matsuie, S.; Takabatake, Y.; Noda, Z.; Hayashi, A.; Shiratori, Y.; Ito, K.; Sasaki, K. Carbon-Free Pt Electrocatalysts Supported on SnO_2 for Polymer Electrolyte Fuel Cells: Electrocatalytic Activity and Durability. *J. Electrochem. Soc.* **2011**, *158* (10), B1270–B1275.

(1-199) Batzill, M.; Diebold, U. The Surface and Materials Science of Tin Oxide. *Prog. Surf. Sci.* **2005**, *79* (2–4), 47–154.

(1-200) Tsukatsune, T.; Takabatake, Y.; Noda, Z.; Daio, T.; Zaitsu, A.; Lyth, S. M.; Hayashi, A.; Sasaki, K. Platinum-Decorated Tin Oxide and Niobium-Doped Tin Oxide PEFC Electrocatalysts: Oxygen Reduction Reaction Activity. *J. Electrochem. Soc.* **2014**, *161* (12), F1208–F1213.

(1-201) Fabbri, E.; Rabis, A.; Chino, Y.; Uchida, M.; Schmidt, T. J. Boosting Pt Oxygen Reduction Reaction Activity by Tuning the Tin Oxide Support. *Electrochem. Commun.* **2017**, *83*, 90–95.

(1-202) Zyubin, A. S.; Zyubina, T. S.; Dobrovol'skii, Y. A.; Frolova, L. A.; Volokhov, V. M. Platinum Nanoparticles on the Antimony-Doped Tin Dioxide Surface: Quantum-Chemical Modeling. *Russ. J. Inorg. Chem.* **2013**, *58* (12), 1489–1495.

(1-203) Zyubin, A. S.; Zyubina, T. S.; Dobrovol'skii, Y. A.; Volokhov, V. M. Interaction of Platinum Nanoparticles with Different Types of Tin Dioxide Surface: Quantum-Chemical Modeling. *Russ. J. Inorg. Chem.* **2013**, *58* (1), 56–61.

(1-204) Zyubina, T. S.; Zyubin, A. S.; Dobrovol, Y. A.; Volokhov, V. M. Quantum Chemical Modeling of Hydrogen Migration on the Pt_{29}/SnO_2 Composite Catalyst. *Russ. Chem. Bull.* **2015**, *64* (4), 752–758.

(1-205) Zyubina, T. S.; Zyubin, A. S.; Dobrovol'skii, Y. A.; Volokhov, V. M. Interaction of Dioxygen with the Platinum $Pt_{19}/SnO_2/H_2$ Cluster: DFT Calculation. *Russ. J. Inorg. Chem.* **2013**, *58* (3), 311–319.

CHAPTER 2

Theory and Computational Methods

Computational chemistry has rapidly emerged as a new practical and robust branch of chemistry to describe the structure and properties of a system.[1,2] Quantum chemical calculations play an important role addressing real-world research problems as they can supplement experimental results to uncover and explore new chemistry.[3] The rigorous foundations in quantum theory, the evolution of the approximations used to decrease the computational cost, the advances in computer hardware, and user-friendly software made quantum chemical calculations a legitimate and indispensable part of chemistry. However, the mathematical equations used in the application of quantum mechanics to chemistry and describe the molecular structure and properties are still the fundamental problem. Thus, the entire field of computational chemistry is built around approximate solutions to those equations. Some of these solutions are very crude but yielding qualitative and valuable insights and not computationally costly, and others are expected to be more rigorous than any experiment ever conducted but requiring extremely long computation time. In short, no method of calculation is likely to be ideal for all applications. Hence the ultimate choice rests on a suitable level of theory for the system to be studied with a reasonable computational cost.[1-4] As a prominent example, DFT method has been developed and evolved as an effective tool to describe the structure and properties of molecules and solids at the atomic scale. The main idea of DFT is to solve the many-particle Schrödinger equation by replacing the complete electron wavefunction with the much simpler ground-state electron density.[5] Using the electron density as the fundamental variable for the description of the energies of electronic systems started soon after the introduction of the Schrödinger equation as its solution was beyond reach in most cases.[3,6-10] Hohenberg and Kohn's work[11] complemented by Kohn and Sham research[12] demonstrated that the electron density of a fully interacting system could be approximated from simple one-electron theory. For decades due to the contribution of different researchers, DFT slowly gathered momentum and improved to the point to be implemented and commercially available in different codes to be applied in a large number of research areas such as material science, biochemistry, chemistry, physics, nano-systems, and devices.

In this chapter, the theoretical backgrounds of the DFT method are presented from the advent of quantum mechanics to the correction/approximations that led to the widespread application of DFT.

2.1 QUANTUM MECHANICS

In theory, quantum mechanics can exactly predict all properties of any system composed of a number of nuclei and electrons interacting with each other.

Formally the Hamiltonian of such system can be written as the following general form:

$$\hat{H} = -\sum_{I=1}^{P} \frac{\hbar^2}{2M_I} \nabla_I^2 - \sum_{I=1}^{N} \frac{\hbar^2}{2m} \nabla_i^2 + \frac{e^2}{2} \sum_{I=1}^{P} \sum_{J \neq 1}^{P} \frac{Z_I Z_J}{|\boldsymbol{R}_I - \boldsymbol{R}_J|}$$

$$+ \frac{e^2}{2} \sum_{i=1}^{N} \sum_{j \neq 1}^{N} \frac{1}{|r_i - r_j|} - \frac{e^2}{2} \sum_{I=1}^{P} \sum_{i=1}^{N} \frac{Z_I}{|\boldsymbol{R}_I - r_i|} \qquad (2\text{-}1)$$

where $\boldsymbol{R} = \{\boldsymbol{R}_I\}, I = 1, \dots, P$ is a set of nuclear coordinates and $\boldsymbol{r} = \{\boldsymbol{r}_i\}, I = 1, \dots, N$ is a set of electronic coordinates. Z_I and M_I are the nuclear charges and masses, respectively.

In principle, all the properties can be derived by solving the many-body Schrödinger equation:

$$\hat{H}\Psi(\boldsymbol{r}, \boldsymbol{R}) = E\Psi(\boldsymbol{r}, \boldsymbol{R}), \qquad (2\text{-}2)$$

where Ψ is the many-body wavefunction for the N electronic eigenstates, and E is the total energy.

In practice, the exact solution of this equation is known only for hydrogen-like atoms. Because this is a multicomponent many-body system, where each component, i.e., the nuclear species and the electrons obey a particular statistics, and the total wavefunction cannot be easily factorized because of coulombic correlations, the Schrödinger equation cannot be easily decoupled into a set of independent equations so that, in general, is required to deal with $3P+3N$ degrees of freedom. Various methods have been developed for approximating the solution for multiple electron systems.

2.2 ADIABATIC APPROXIMATION

This approximation is also called the Born-Oppenheimer approximation,[13] and is based on the difference in mass between nuclei and electrons, meaning that the electron velocity is much larger than that of the nuclei due to the difference of mass. Hence, it was proposed that the electrons can be regarded to respond the motion of the nuclei instantaneously, i.e., as the nuclei follow their dynamics, the electrons immediately adjust their wavefunction according to the nuclear wavefunction.[13] Hence, the full wavefunction can be expressed as:

$$\Psi(\boldsymbol{R},\boldsymbol{r},t) = \Theta_m(\boldsymbol{R},t)\Phi_m(\boldsymbol{R},\boldsymbol{r}), \tag{2-3}$$

which is the electronic Schrödinger equation and is the basis for standard quantum chemistry.[3,7,10,14] In the electronic Schrödinger equation, the electronic wavefunction $\Phi_m(R,r)$ is the mth stationary state of the electronic Hamiltonian,

$$\hat{h}_e = \hat{T}_e + \hat{U}_{ee} + \hat{V}_{ne} = \hat{H} - \hat{T}_n - \hat{U}_{nn}, \tag{2-4}$$

where $\hat{\mathrm{T}}_n$ and $\hat{U}_{nn}$ are the kinetic and potential nuclear operators, $\hat{\mathrm{T}}_e$ and $\hat{U}_{ee}$ are the kinetic and potential electron operators, and $\hat{\mathrm{V}}_{ne}$ the electron-nuclear interaction.

To obtain the correct potential energy curves from quantum chemical calculations, the interaction between nuclei has to be added:

$$E = E_e + \frac{e^2}{2}\sum_{I=1}^{P}\sum_{J\neq 1}^{P}\frac{Z_I Z_J}{|\boldsymbol{R}_I-\boldsymbol{R}_J|}, \tag{2-5}$$

Separating the electronic and nuclear wavefunctions simplifies the resolution of the total Schrödinger equation. The determination of the entire wavefunction of the system nuclei plus electrons is reduced to finding the total electronic wavefunction. However, the electronic wavefunction cannot be factorized because the presence of an electron in a region of space influences the behavior of other electrons in other regions, so they cannot be considered as individual entities. Hence, getting the exact solution involves solving an equation in $3N$ degrees of freedom. This exact solution is known only for the homogeneous electron gas, for atoms with a small number of electrons and a few small molecules, for larger systems the only option is to employ some types of approximations.

2.3 HARTREE-FOCK APPROXIMATION

The Hartree approximation postulates that the many-electron wavefunction can be written as a simple product of one-electron wavefunction. Each of these verifies a one-particle Schrödinger equation in an effective potential that takes into consideration the interaction with the other electrons in a mean-field:

$$\Phi_m(\boldsymbol{R},\boldsymbol{r}) = \prod_i \varphi_i(\boldsymbol{r}_i), \tag{2-6}$$

$$\left(-\frac{\hbar}{2m}\nabla^2 + V^i_{eff}(\boldsymbol{R},\boldsymbol{r})\right)\varphi_i(\boldsymbol{r}) = \varepsilon_i\varphi_i(\boldsymbol{r}), \tag{2-7}$$

where φ_i is the one electron orbital, ε_i is the one-electron eigenvalue, and the effective potential is defined as:

$$V^i_{eff}(\boldsymbol{R},\boldsymbol{r}) = V(\boldsymbol{R},\boldsymbol{r}) + \int \frac{\sum_{j\neq i}^N \rho_j(r')}{|r-r'|} d\boldsymbol{r}', \tag{2-8}$$

where the second term in the right side of the equation is the classical electrostatic potential generated by the charge distribution $\sum_{j\neq i}^N \rho_j(\boldsymbol{r})$, and the electronic density associated with particle j is defined as:

$$\rho_j(\boldsymbol{r}) = \left|\varphi_j(\boldsymbol{r})\right|^2, \tag{2-9}$$

The charge density does not include the charge associated with particle i, so that the Hartree approximation is self-interaction-free. As consequence of the effective potential the electron-electron interaction is counted twice, hence the correct expression for the energy is as follows:

$$E_H = \sum_{n=1}^N \varepsilon_n - \frac{1}{2}\sum_{i\neq j}^N \iint \frac{\rho_i(r)\rho_j(r\prime)}{|r-r'|} d\boldsymbol{r}d\boldsymbol{r}', \tag{2-10}$$

The set of N coupled partial differential equations in (2-7) can be solved by minimizing the energy with respect to a set of variational parameters in a trial wavefunction or, alternatively, by recalculating the electronic densities in (2-9) using the solutions of (2-7), then inserting them back into the expression for the effective potential (2-8), and solving again the Schrödinger equation. This procedure can be iterated, until self-consistency in the input and output wavefunctions or potentials is achieved. This process is called self-consistent Hartree. The Hartree approximation treats the electrons as distinguishable particles, thus it does not consider Pauli's Exclusion Principle that states that two fermions cannot occupy the same quantum state because the many-fermion wave function has to be antisymmetric upon particle exchange. For two electrons in the same quantum state, the only antisymmetric wavefunction is the null wave function. Hence, the description of the electronic components is incomplete.

The consideration of the Pauli Exclusion Principle is included by proposing an antisymmetrized many-electron wavefunction in the form of a Slater determinant:

$$\Phi_{HF}(\boldsymbol{x}_1, \dots, \boldsymbol{x}_N) = \frac{1}{\sqrt{N!}} \begin{vmatrix} \varphi_1(1) & \varphi_2(1) & \cdots & \varphi_N(1) \\ \varphi_1(2) & \varphi_2(2) & \cdots & \varphi_N(2) \\ \vdots & \vdots & \ddots & \vdots \\ \varphi_1(N) & \varphi_2(N) & \cdots & \varphi_N(N) \end{vmatrix}$$

$$= SD\{\varphi_1(1)\varphi_2(2) \dots \varphi_N(N)\}, \qquad (2\text{-}11)$$

where $\varphi_i(j)$ refers to the i th one-electron spin orbital composed of spatial and spin components, and (j) indicates the spatial and spin coordinates of electron j condensed in a single variable $\boldsymbol{x}_1 = (\boldsymbol{r}_j, \boldsymbol{\sigma}_j)$. The mathematical properties of the determinant expression ensures that the wavefunction changes sign when exchanging the coordinates of two of the electrons. The method of approximation consisting of postulating a wavefunction of the form as in (2-11) is called Hartree-Fock (HF) or self-consistent field (SCF) method, and it has been used for long time to calculate the electronic structure of molecular systems, because it provides a reasonable picture of atomic systems and a reasonable good description of interatomic bonding.[7,10] One of the limitations of HF method is that they do not include electron correlation.[2] This means that HF method takes into account the average effect of electron repulsion, but not the explicit electron-electron interaction. The HF method is usually used as starting point of more rigorous calculations such as Møller-Plesset perturbation theory (MPn, where n is the order of correction), the generalized valence bond

(GVB) method, multi-configurational self-consistent field (MCSCF), configuration interaction (CI), and coupled cluster theory (CC) and then correcting for correlation.

2.4 THOMAS-FERMI APPROXIMATION

Alongside the HF approximation, Thomas[15] and Fermi[16] proposed to use the electronic density as the fundamental variable for solving the many-electron problem, since the electron density is a physical observable, it can be measured, calculated, and easily visualized.

In their approximation, Thomas and Fermi stated that the properties of an inhomogeneous system are locally identical to those of the homogeneous electron. This was the first time that the local density approximation (LDA) was used. For the homogeneous electron gas, the density is related to the Fermi energy (ε_F) by:

$$\rho = \frac{1}{3\pi^2}\left(\frac{2m}{\hbar^2}\right)^{3/2} \varepsilon_F^{3/2}, \tag{2-12}$$

and the kinetic energy of the homogeneous gas is:

$$T = \frac{3\rho\varepsilon_F}{5}, \tag{2-13}$$

then the kinetic energy density is:

$$t[\rho] = \frac{3}{5}\frac{\hbar^2}{2m}(3\pi^2)^{2/3}\rho^{5/3}, \tag{2-14}$$

the Thomas-Fermi kinetic energy functional, which is function of the local electron density is:

$$T_{TF}[\rho] = C_k \int \rho(\boldsymbol{r})^{5/3}\, dr, \tag{2-15}$$

with $C_k = \frac{3}{10}(3\pi^2)^{2/3} = 2.871$ atomic units. Adding to the Thomas-Fermi kinetic energy functional the classical electrostatic energies of electron-nucleus attraction and electron-electron repulsion it is possible to obtain the energy functional of the Thomas-Fermi theory of atoms:

$$E_{TF}[\rho] = C_k \int \rho(\boldsymbol{r})^{5/3}\, d\boldsymbol{r} + \int v(\boldsymbol{r})\rho(\boldsymbol{r})d\boldsymbol{r} + \frac{1}{2}\iint \frac{\rho(r)\rho(r\prime)}{|r-r\prime|}\, d\boldsymbol{r}d\boldsymbol{r}', \tag{2-16}$$

Because E_{TF} depends only on the electronic density, it is a function of the density, which can be minimized with the constraint $\int \rho(\boldsymbol{r})d\boldsymbol{r} = N$ to approximate the ground state electron density of an atom. The Thomas-Fermi approximation is actually too crude because it does not include exchange and correlation effects, more importantly, no molecular bonding is predicted. However, it sets up the basis for the later development of DFT.

2.5 DENSITY FUNCTIONAL THEORY

The DFT method has become very popular in recent years as it can describe accurately the structure and properties of a system and less computationally demanding than other methods with similar accuracy.[2,5,17,18]

The modern formalism of DFT started when Hohenberg and Kohn formulated and proved a theorem that put on solid mathematical grounds the ideas proposed by Thomas and Fermi.

2.5.1 Hohenberg-Kohn theorem. The Hohenberg and Kohn theorem is divided into two parts:

Theorem: For any system of interacting particles in an external potential, the potential is uniquely determined by the ground state particle density, except for a trivial additive constant.

Proof: Supposing the opposite, i.e., that the potential is not uniquely determined by the density, then it is possible to find two potentials v and v' such that they have the same ground state density ρ. Let Ψ and $E_0 = \langle\Psi|\hat{H}|\Psi\rangle$ be the ground state wavefunction and ground state energy of $\hat{H} = \hat{T} + \hat{U} + \hat{V}$, and Ψ' and $E_0' = \langle\Psi'|\hat{H}'|\Psi'\rangle$ the ground state wavefunction and ground state energy of $\hat{H}' = \hat{T} + \hat{U} + \hat{V}'$. Owing to the variatonal principle:

$$E_0 < \langle\Psi'|\hat{H}|\Psi'\rangle = \langle\Psi'|\hat{H}'|\Psi'\rangle + \langle\Psi'|\hat{H} - \hat{H}'|\Psi'\rangle, \qquad (2\text{-}17)$$

which written in terms of the density:

$$E_0 < \langle\Psi'|\hat{H}|\Psi'\rangle = E_0' + \int \rho(\boldsymbol{r})\big(v(\boldsymbol{r}) - v'(\boldsymbol{r})\big)d\boldsymbol{r}, \qquad (2\text{-}18)$$

Reversing the situation of Ψ and Ψ' it can be obtained:

$$E_0' < \langle\Psi|\hat{H}'|\Psi\rangle = \langle\Psi|\hat{H}|\Psi\rangle + \langle\Psi|\hat{H}' - \hat{H}|\Psi\rangle, \tag{2-19}$$

$$E_0' < \langle\Psi|\hat{H}'|\Psi\rangle = E_0 - \int \rho(\boldsymbol{r})\big(v(\boldsymbol{r}) - v'(\boldsymbol{r})\big)d\boldsymbol{r}, \tag{2-20}$$

Adding the inequalities, it turns out that $E_0 + E_0' < E_0' + E_0$, which is absurd. Therefore, there are not two external potentials determined by the same ground state electronic density.

Theorem: A universal functional for the energy $E[\rho]$ in terms of the density $\rho(\boldsymbol{r})$ can be defined valid for any external potential $v(\boldsymbol{r})$. For any particular $v(\boldsymbol{r})$, the exact ground state energy of the system is the global minimum value of this functional, and the density that minimizes the functional is the exact ground state density.

Proof: For a trial electron density $\tilde{\rho}(\boldsymbol{r})$ such that $\tilde{\rho}(\boldsymbol{r}) \geq 0$ and $\int \tilde{\rho}(\boldsymbol{r})\, dr = N$, then $E_0 < E_v[\tilde{\rho}]$, for

$$E_v[\tilde{\rho}] = F[\tilde{\rho}] + \int \tilde{\rho}(\boldsymbol{r})v(\boldsymbol{r})d\boldsymbol{r}, \tag{2-21}$$

and $F[\tilde{\rho}]$ can be defined as:

$$F[\tilde{\rho}] = \langle\Psi[\tilde{\rho}]|\hat{T} + \hat{U}|\Psi[\tilde{\rho}]\rangle, \tag{2-22}$$

where $\Psi[\tilde{\rho}]$ is the ground state of a potential that has $\tilde{\rho}$ as its ground state density.

Since the external potential is uniquely determined by the density and the potential, in turn, determines the ground state wavefunction, all the other observables of the system such as kinetic energy are uniquely determined. Then, the energy as functional can be written as:

$$\begin{aligned}\langle\Psi[\tilde{\rho}]|\hat{H}|\Psi[\tilde{\rho}]\rangle &= F[\tilde{\rho}] + \int \tilde{\rho}(\boldsymbol{r})v(\boldsymbol{r})d\boldsymbol{r}, \\ &= E_v[\tilde{\rho}] \geq E_v[\rho] = E_0 = \langle\Psi|\hat{H}|\Psi\rangle,\end{aligned} \tag{2-23}$$

Employing the Rayleigh-Ritz's variational principle applied the electronic density:

$$\delta\{E_v[\rho] - \mu(\int \rho(\boldsymbol{r})d\boldsymbol{r} - N)\} = 0, \tag{2-24}$$

and a generalized Thomas-Fermi equation is obtained:

$$\mu = \frac{\delta E_v[\rho]}{\delta\rho} = v(\boldsymbol{r}) + \frac{\delta F[\rho]}{\delta\rho}, \tag{2-25}$$

where μ is the Lagrange multiplier associated with the constraint that the number of electrons N is conserved.

Using DFT, one can determine the electronic ground state density and energy exactly, provided that $F[\rho]$ is known.[4,7,10] $F[\rho]$ is a universal functional that does not depend explicitly on the external potential. It depends only on the electronic density.

2.5.2 The Kohn-Sham formulation. DFT would remain a minor curiosity today if it were not for the ansatz made by Kohn and Sham, which has provided a way to make useful approximate ground state functionals for real systems of many electrons.[17] The idea of Kohn and Sham was to set up a system where the kinetic energy could be determined exactly, since this was a significant problem in Thomas-Fermi theory. Kohn-Sham formulation proposed to replace the kinetic energy of the interacting electrons with that of an equivalent non-interacting system, and that the exact ground state density can be represented by the ground state density of a reference system of non-interacting particles:

$$T = \sum_{s=1}^{2}\sum_{i=1}^{\infty} n_{i,s}\left\langle \varphi_{i,s}\left|-\frac{\nabla^2}{2}\right|\varphi_{i,s}\right\rangle, \tag{2-26}$$

$$\rho_s(\boldsymbol{r},\boldsymbol{r}') = \sum_{i=1}^{\infty} n_{i,s}\varphi_{i,s}(\boldsymbol{r})\varphi_{i,s}^{*}(\boldsymbol{r}'), \tag{2-27}$$

where $\{\varphi_{i,s}(\boldsymbol{r})\}$ are the natural spin orbitals and $\{n_{i,s}\}$ are the occupation numbers of these orbitals. The non-interacting reference system of density $\rho(\boldsymbol{r})$ that is described by the Hamiltonian:

$$\widehat{H}_R = \sum_{i=1}^{N}\left(-\frac{\nabla_i^2}{2} + v_R(\boldsymbol{r}_i)\right), \tag{2-28}$$

where the potential $v_R(\boldsymbol{r})$ is such that the ground state density of $\widehat{H}_R$ equals $\rho(\boldsymbol{r})$ and the ground state energy equals the energy of the interacting system. This Hamiltonian has no electron-electron interactions and, thus, its eigenstates can be expressed in the form of Slater determinants meaning that the density can be written as:

$$\rho(\boldsymbol{r}) = \sum_{s=1}^{2}\sum_{i=1}^{N_s}\left|\varphi_{i,s}(\boldsymbol{r})\right|^2, \tag{2-29}$$

The kinetic term is:

$$T_R[\rho] = \sum_{s=1}^{2}\sum_{i=1}^{N_s}\left\langle \varphi_{i,s}\left|-\frac{\nabla^2}{2}\right|\varphi_{i,s}\right\rangle, \tag{2-30}$$

The ground-state density is obtained in practice by solving the N one-electron Schrödinger equations.

$$\left\{-\frac{\nabla^2}{2}+v_R(\boldsymbol{r})\right\}\varphi_{i,s}(\boldsymbol{r})=\varepsilon_{i,s}\varphi_{i,s}(\boldsymbol{r}), \tag{2-31}$$

where ε_i are Lagrange multipliers corresponding to the orthonormality of the N single-particle states $\varphi_i(\boldsymbol{r})$. Then the universal density functional $F[\rho]$ can be partitioned into three terms:

$$F[\rho]=T_R[\rho]+\frac{1}{2}\iint\frac{\rho(r)\rho(r\prime)}{|r-r\prime|}d\boldsymbol{r}d\boldsymbol{r}'+E_{XC}[\rho], \tag{2-32}$$

where $E_{XC}[\rho]$, is the exchange-correlation energy as functional of the density, which contains the difference between the exact and non-interacting kinetic energies and also the non-classical contribution to the electron-electron interactions, and $T_R[\rho]$, is the kinetic energy term of the non-interacting reference system. Hence this implies that the correlation piece of the true kinetic energy has been ignored and has to be taken into account elsewhere. This is done by redefining the correlation energy functional in such a way as to include kinetic correlations. Replacing this value for the universal functional in the total energy functional $E_{KS}[\rho]=F[\rho]+\int\rho(\boldsymbol{r})v(\boldsymbol{r})d\boldsymbol{r}$, the latter is called the Kohn-Sham functional:

$$E_{KS}[\rho]=T_R[\rho]+\int\rho(\boldsymbol{r})v(\boldsymbol{r})d\boldsymbol{r}+\frac{1}{2}\iint\frac{\rho(r)\rho(r\prime)}{|r-r\prime|}d\boldsymbol{r}d\boldsymbol{r}'+E_{XC}[\rho], \tag{2-33}$$

In the Kohn-Sham formalism, the Euler equation is expressed as

$$\mu_R=\frac{\delta T_R[\rho]}{\delta\rho(\boldsymbol{r})}+v_R(\boldsymbol{r}), \tag{2-34}$$

where μ_R is the chemical potential for the non-interacting system and the effective potential v_R or v_{eff} is given by

$$v_{eff}(\boldsymbol{r})=v(r)+\int\frac{\rho(v_R(r\prime)}{|r-r\prime|}d\boldsymbol{r}'+\mu_{XC}[\rho](\boldsymbol{r}), \tag{2-35}$$

The exchange-correlation potential $\mu_{XC}[\rho](\boldsymbol{r})$ is the functional derivative of the exchange-correlation energy $\delta E_{XC}[\rho]/\delta\rho$. The solution of the Kohn-Sham equations has to be obtained by an iterative procedure similar to the HF equations and double counting terms have to be subtracted:

$$E_{KS}[\rho] = \sum_{i=1}^{N_s}\sum_{s=1}^{2} \varepsilon_{i,s} - \frac{1}{2}\iint \frac{\rho(\boldsymbol{r})\rho(\boldsymbol{r}')}{|\boldsymbol{r}-\boldsymbol{r}'|} d\boldsymbol{r}d\boldsymbol{r}' + \{E_{XC}[\rho] \qquad (2\text{-}36)$$
$$- \int \rho(\boldsymbol{r})\mu_{XC}[\rho](\boldsymbol{r})d\boldsymbol{r}\},$$

All the unknowns about the many-fermion problem have been displaced to the $E_{XC}[\rho]$ term, while the remaining terms in the energy are known.

2.5.3 Exchange-correlation energy. The fact that both exchange and correlation effects tend to keep electrons apart led to the description of the exchange and correlation contribution in terms of a hole surrounding each electron and keeping other electrons from approaching it. The exchange-correlation hole averaged over the strength of the interaction, taking into consideration kinetic correlations can be defined as:

$$E_{XC}[\rho] = \frac{1}{2}\iint \frac{\rho(r)\tilde{\rho}_{XC}(r,r')}{|r-r'|} d\boldsymbol{r}d\boldsymbol{r}' , \qquad (2\text{-}37)$$

where $\tilde{\rho}_{XC}(\boldsymbol{r},\boldsymbol{r}') = \rho(\boldsymbol{r}')\,[\tilde{g}(\boldsymbol{r},\boldsymbol{r}') - 1]$, and $g(\boldsymbol{r},\boldsymbol{r}')$ is the pair correlation function, that takes into account the fact that the presence of an electron at $\boldsymbol{r}$ discourages a second electron to be located at a position $\boldsymbol{r}'$ because of the Coulomb repulsion.

Needless to mention, neither the exchange-correlation hole density or the pair correlation functional can be calculated exactly. Hence the exchange and correlation functionals have been the focus of many investigations, leading to differently available functionals discussed in the literature.

2.5.3.1 The local density approximation. The simplest and most widely used density functional approximation for the exchange-correlation energy is the LDA. The main idea is to consider general inhomogeneous electronic systems as locally homogeneous, and then to use the exchange-correlation hole corresponding to the homogeneous electron gas for which there are good approximations.

$$\tilde{\rho}_{XC}^{LDA}(\boldsymbol{r},\boldsymbol{r}') = \rho(\boldsymbol{r})(\tilde{g}^{h}[|\boldsymbol{r}-\boldsymbol{r}'|,\ \rho(\boldsymbol{r})] - 1)\, , \qquad (2\text{-}38)$$

where $\tilde{g}^{h}[|\boldsymbol{r}-\boldsymbol{r}'|,\ \rho(\boldsymbol{r})]$ is the pair correlation function of the homogenous gas depending only on the distances between $\boldsymbol{r}$ and $\boldsymbol{r}'$, evaluated at the density ρ^{h}, which locally equals $\rho(\boldsymbol{r})$.

Using this approximation, the energy per particle of the homogeneous electron gas is defined as:

$$\varepsilon_{XC}^{LDA}[\rho] = \frac{1}{2}\int \frac{\tilde{\rho}_{XC}^{LDA}(\boldsymbol{r},\boldsymbol{r}')}{|\boldsymbol{r}-\boldsymbol{r}'|}\, d\boldsymbol{r}' , \tag{2-39}$$

and the exchange-correlation energy becomes:

$$E_{XC}^{LDA}[\rho] = \int \rho(\boldsymbol{r})\, \varepsilon_{XC}^{LDA}[\rho] d\boldsymbol{r} , \tag{2-40}$$

2.5.3.2 The local spin density approximation. In systems where open electronic shells are studied, taking into consideration, the two spin densities led to better approximations to the exchange-correlation functional. The equivalent of the LDA in spin-polarized systems is the local spin density approximation (LSDA), which consists of replacing the energy per particle of the homogeneous electron gas with a spin-polarized expression:

$$E_{XC}^{LSDA}[\rho_{\uparrow}(\boldsymbol{r}), \rho_{\downarrow}(\boldsymbol{r})] = \int [\rho_{\uparrow}(\boldsymbol{r}) + \rho_{\downarrow}(\boldsymbol{r})] \varepsilon_{XC}^{h}[\rho_{\uparrow}(\boldsymbol{r}), \rho_{\downarrow}(\boldsymbol{r})] d\boldsymbol{r} , \tag{2-41}$$

The LDA is a successful approximation for bulk metals, semiconductors, and ionic crystals. However it fails to reproduce features in atomic systems, where the density has large variation, and the self-interaction is also important. Similarly, the LDA cannot reproduce all the properties in systems with weak molecular bonds, such as hydrogen bond because the density region is very small, and in negatively charged ions because fails to cancel the electronic self-interaction. Likewise, LDA calculations underestimate the energy band gap in semiconductors.

Introducing semi-locally the non-uniformity of the density by expanding $E_{XC}[\rho]$ as a series in terms of the density and its gradients led to some improvements over the LDA and computationally more convenient than full many-body approaches.

2.5.3.3 The generalized gradient approximation. In the generalized gradient approximation (GGA), the exchange-correlation energy has a gradient expansion of the type:

$$E_{XC}[\rho] = \int A_{XC}[\rho]\rho(\boldsymbol{r})^{4/3}\, d\boldsymbol{r} + \int C_{XC}[\rho]|\nabla\rho(\boldsymbol{r})|^2 / \rho(\boldsymbol{r})^{4/3} d\boldsymbol{r} + \cdots , \tag{2-42}$$

which is asymptotically valid for densities that fluctuate slowly in space. The expansion must be carried out carefully because they can violate one or more of the exact conditions required for the exchange and correlation holes such as the normalization condition, the negativity of the exchange density and the self-interaction cancellation.[7]

Hence, the GGA expresses the exchange-correlation energy as:

$$E_{XC}[\rho] = \int \rho(\boldsymbol{r})\varepsilon_{XC}[\rho(\boldsymbol{r})]\, d\boldsymbol{r} + \int F_{XC}[\rho(\boldsymbol{r}), \nabla\rho(\boldsymbol{r})]\, d\boldsymbol{r}, \tag{2-43}$$

where the function F_{XC} needs to satisfy a number of formal conditions for the exchange-correlation hole, such as sum rules, long-range decay. Therefore, there are different GGAs each making a different choice of the F_{XC} function. Among them, the Perdew-Burke-Ernzerhof (PBE)[18,19] exchange-correlation functional satisfies the uniform scaling condition, recovers the correct uniform electron gas limit, obeys the spin-scaling relationship, recovers the LSDA linear response limit, and satisfies the Lieb-Oxford bound. Aditionally, the PBE's GGA does not contain any fitting parameters making it satisfactory from the theoretical point of view. The enhancement factor F_{XC} over the local exchange in the PBE exchange-correlation functional, is defined as:

$$E_{XC}[\rho] = \int \rho(\boldsymbol{r})\varepsilon_X^{LDA}[\rho(\boldsymbol{r})]F_{XC}(\rho, \zeta, s)d\boldsymbol{r}, \tag{2-44}$$

where ρ is the local density, ζ is the relative spin polarization and $s = \frac{|\nabla\rho(\boldsymbol{r})|}{2k_F\rho}$ is the dimensionless density gradient:

$$F_X(s) = 1 + \kappa - \frac{\kappa}{1+\mu s^2/\kappa}, \tag{2-45}$$

where $\mu = \beta\left(\frac{\pi^2}{3}\right)$ =0.21951 and β =0.066725 is related to second order gradient expansion.

The correlation energy is written in the following form:

$$E_C^{GGA} = \int \rho(\boldsymbol{r})[\varepsilon_C^{LDA}(\rho, \zeta) + H[\rho, \zeta, t]]d\boldsymbol{r}, \tag{2-46}$$

with

$$H[\rho, \zeta, t] = (\frac{e^2}{a_0})\gamma\phi^3 \ln\{1 + \frac{\beta\gamma^2}{t}\left[\frac{1+At^2}{1+At^2+At^4}\right]\}, \tag{2-47}$$

where $t = \frac{|\nabla\rho(r)|}{2\phi k_s\rho}$ is a dimensionless density gradient, $k_s = (\frac{4k_F}{\pi a_0})^{1/2}$ is the Thomas-Fermi screening wave number and $\phi(\zeta) = \frac{[(1+\zeta)^{2/3}+(1-\zeta)^{2/3}]}{2}$ is a spin-scaling factor. The quantity β

is the same as for the exchange term and $\gamma = \frac{1-ln2}{\pi^2} = 0.031091$, and the function $A = \frac{\beta}{\gamma}[e^{-\varepsilon_C^{LDA}[\rho]/(\frac{\gamma\phi^3 e^2}{a_0})} - 1]^{-1}$.

The GGA-PBE retains the correct features of LSDA and combines them with the inhomogeneity features that are supposed to be the most important energetically. Some improvements of GGAs over the LDA can be pointed out; improved binding energies and atomic energies, enhanced bond lengths and angles, improved description of hydrogen-bonded systems. On the other hand, semiconductors are better described by LDA than GGA, lattice constants of noble metals (Ag, Au, Pt) are overestimated by GGA functionals, band gaps and consequently dielectric constants are better estimated by LDA than GGA.

2.6 PROJECTOR AUGMENTED WAVE METHOD

Solving the Kohn-Sham equations pose substantial numerical difficulties for example, near the nucleus, due to the large kinetic energy of the electrons, the rapid oscillating wavefunction can be properly represented by a small basis set. On the other hand, in the bonding region between atoms, the kinetic energy is small, and the wavefunction is smooth, and the change in the chemical environment has a strong effect on the shape of the wavefunction, hence requires a large basis set. Various strategies have been developed to deal with the problems mentioned above.

- In the pseudopotential method, the Pauli repulsion of the core electrons is therefore described by an effective potential that expels the valence electrons from the core region. This approach avoids describing explicitly the core electrons, hence avoiding the rapid oscillating wavefunction near the nucleus.
- Augmented wave methods compose their basis functions from atom-like wavefunctions in the atomic regions and a set of envelope functions appropriated for the bonding in between. Space is divided accordingly into atom-centered spheres, defining the atomic regions, and an interstitial region in between. The partial solutions of the different regions are matched at the interface between atomic and interstitial regions.

The projector augmented wave (PAW) method[20] combines features from the pseudopotential method and the augmented wave methods into a unified electronic structure method for calculating the total energy, forces, and stress. The PAW method introduced by Blöchl is built on projector functions that map the true wavefunction ($\Psi_n(r)$) with their complete (complicated) nodal structure onto pseudo (auxiliary) wavefunction ($\widetilde{\Psi}_n(r)$), which are easier to treat computationally. The transformation from the auxiliary to the physical wavefunctions is denoted by $\mathcal{T}$, such as:

$$\Psi_n(r) = \mathcal{T}\widetilde{\Psi}_n(r), \tag{2-48}$$

The operator $\mathcal{T}$, has to modify the smooth auxiliary wavefunction in each atomic region, so that the resulting wavefunction has the correct nodal structure.

$$\mathcal{T} = 1 + \textstyle\sum_R \mathrm{S}_R, \tag{2-49}$$

where S_R, is the atomic contribution, that adds the difference between the true and auxiliary wavefunction. The transformation $\mathcal{T}$ shall produce only wavefunctions orthogonal to the core electrons, while the core electrons are treated separately.

Then, total energy can be expressed by auxiliary wavefunctions as:

$$E = E[\Psi_n(r)] = E[\mathcal{T}\widetilde{\Psi}_n(r)], \tag{2-50}$$

and the Schrödinger-like equation for auxiliary functions can be obtained, but the Hamiltonian operator has a different form, $\widetilde{H} = \mathcal{T}^{\dagger}H\mathcal{T}$, an overlap operator $\widetilde{O} = \mathcal{T}^{\dagger}\mathcal{T}$ occurs, and the resulting auxiliary wavefunction are smooth.

To evaluate the physical quantities is required to assess the expectation values of an operator A that can be expressed in terms of the true or the auxiliary wavefunctions

$$\langle A\rangle = \textstyle\sum_n f_n \langle\Psi_n|A|\Psi_n\rangle = \sum_n f_n \langle\widetilde{\Psi}_n|\mathcal{T}^{\dagger}A\mathcal{T}|\widetilde{\Psi}_n\rangle, \tag{2-51}$$

where f_n is the occupation state.

The PAW method has extensively proven its high performance compared to norm-conserving pseudopotentials as the total energy expression is less complex and can, therefore, be expected to be more efficient.

2.7 QUANTUM CALCULATIONS SOFTWARE

The improved accuracy of DFT led to the point where most established and commercially available codes for molecular calculations nowadays can be run also in DFT mode. Among them Vienna Ab initio Simulation Package (VASP)[21-25] computes an approximate solution to the many-body Schrödinger equation by solving the Kohn-Sham equations within DFT. In VASP, the Kohn-Sham equations are solved self-consistently with an iterative matrix diagonalization coupled to highly efficient Broyden and Pulay density mixing schemes[26,27] to speed up the self-consistency cycle. The iterative matrix diagonalization is performed by techniques and algorithms implemented in VASP, like the residual minimization method with direct inversion of the iterative subspace (RMM-DIIS) or blocked Davidson algorithms. The algorithms calculate the electronic ground state for a given geometry, calculate forces, and then based on these forces calculate a new geometry. This process is repeated until an energy (force) criterion is reached. The interactions between the electrons and ions are described using norm-conserving or ultrasoft pseudopotentials, or the PAW method.

2.7.1 Periodic Boundary Conditions. Crystalline solids contain an infinite number of electrons, hence the wavefunction has to be calculated for each electron and the basis set, in which the wavefunction is expressed will also be infinitely large. To overcome this issue, periodic boundary conditions are introduced to reduce the studied system to one particular unit cell that is periodically repeated in three dimensions. The periodicity for surfaces and clusters is in two dimensions. Crystal surfaces are represented as slabs, i.e., several layers of atoms that can represent the bulk and surface atoms with a vacuum region. This vacuum region must be large enough to prevent any spurious interaction between the adsorbate and the next periodic image.

According to Bloch's theorem,[28] and the periodicity of the crystal, the massive number of one-electron wavefunctions is reduced to the number of electrons in the unit cell to be computed. Then the wavefunction of an electron, $\psi_{j,k}$, within a periodic potential, can be written as the product of a lattice periodic part $\mu_j(\boldsymbol{r})$, and a wavelike part $e^{ik\cdot\boldsymbol{r}}$:

$$\psi_{j,k}(\boldsymbol{r}) = \mu_j(\boldsymbol{r})e^{ik\cdot\boldsymbol{r}}, \tag{2-52}$$

where j indicates the band index and k is a continuous wavevector that is confined to the first Brillouin zone of the reciprocal lattice. To minimize the number of k-points needed to integrate the Brillouin zone, a number of special set of k-points is employed that can be calculated by various methods. Among them, in the Monkhorst-Pack method,[29] the k-points are distributed homogeneously throughout space in rows and columns that follow the shape of the Brillouin zone:

$$k_j = x_{1j}b_1 + x_{2j}b_2 + x_{3j}b_3, \tag{2-53}$$

where b_1, b_2, b_3 are the reciprocal vectors
and,

$$x_{ij} = \frac{l_i}{n_j}, \;\; j = 1, \dots, n_j\,, \tag{2-54}$$

where l_i are the lengths of the reciprocal lattice vectors and n_j characterizes the number of special points in the set.

In order to reproduce accurately the properties of the researched material, a sufficiently large number of k-points must be used. However, the computational cost increases with increasing the k-point mesh. Therefore, it is usual to test a varied set of k-points until the convergence is reached within the chosen accuracy.

In this work, two different material systems were engaged. Hence, to reproduce the materials and species' properties accurately, and to obtain meaningful and reproducible results different computational details were employed for each study. For each of the problems tackled a subsection with its specific computational procedure can be found in their respective chapter of the results and discussion.

REFERENCES

(2-1) Jensen, F. *Molecular Modelling*, Second edit.; John Wiley & Sons Ltd.: Chichester, England, 2007.

(2-2) Young, D. C. *Computational Chemistry A Practical Guide for Applying Techniques to Real-World Problems*; John Wiley & Sons, Inc.: New York, USA, 2001.

(2-3) Hehre, W. J. *A Guide to Molecular Mechanics and Quantum Chemical Calculations*; Wavefunction, Inc.: Irvine, CA, 2003.

(2-4) Jalbout, A. F.; Nazari, F.; Turker, L. Gaussian-Based Computations in Molecular Science. *J. Mol. Struct. THEOCHEM* **2004**, *671* (1–3), 1–21.

(2-5) Lejaeghere, K.; Bihlmayer, G.; Björkman, T.; Blaha, P.; Blügel, S.; Blum, V.; Caliste, D.; Castelli, I. E.; Clark, S. J.; Dal Corso, A.; et al. Reproducibility in Density Functional Theory Calculations of Solids. *Science* **2016**, *351* (6280), 1415.

(2-6) von Barth, U. Basic Density-Functional Theory an Overview. *Phys. Scr.* **2004**, *T109* (6), 9–39.

(2-7) Kohanoff, J.; Gidopoulos, G. N. Density Functional Theory: Basics, New Trends and Applications. In *Handbook of Molecular Physics and Quantum Chemistry. Volume 2: Molecular Electronic Structure*; Wilson, S., Bernath, P. F., McWeeny, R., Eds.; John Wiley & Sons, Ltd: Chichester, England, 2003; pp. 532–568.

(2-8) Jones, R. O. Density Functional Theory: Its Origins, Rise to Prominence, and Future. *Rev. Mod. Phys.* **2015**, *87* (3), 897–923.

(2-9) Perdew, J. P.; Kurth, S. Density Functionals for Non-Relativistic Coulomb Systems in the New Century. In *A Primer in Density Functional Theory. Lecture Notes in Physics*; Fiolhais, C., Nogueira, F., Marques, M., Eds.; Springer: Berlin, Heidelberg, 2003; Vol. 620, pp. 1–55.

(2-10) Kohanoff, J. *Electronic Structure Calculations for Solids and Molecules*, First edit.; Cambridge University Press: Cambridge, England, 2006.

(2-11) Hohenberg, P.; Kohn, W. Inhomogeneous Electron Gas. *Phys. Rev.* **1964**, *136* (3B), B864–B871.

(2-12) Kohn, W.; Sham, L. J. Self-Consistent Equations Including Exchange and Correlation Effects. *Phys. Rev.* **1965**, *140* (4A), A1133–A1138.

(2-13) Born, M.; Oppenheimer, R. Zur Quantentheorie Der Molekeln. *Ann. Phys.* **1927**, *389* (20), 457–484.

(2-14) Frank, I. On the Classical Description of Nuclear Motion. *arXiv:1402.1133* **2014**, 6, 1–3.

(2-15) Thomas, L. H. The Calculation of Atomic Fields. *Math. Proc. Cambridge Philos. Soc.* **1927**, *23* (5), 542–548.

(2-16) Fermi, E. Un Metodo Statistico per La Determinazione Di Alcune Proprietá Dell' Atomo. *Rend. Accad. Naz. del Lincei, Cl. Sci. Fis., Mat. e. Nat.* **1927**, *6* (6), 602–607.

(2-17) Perdew, J. P.; Burke, K.; Ernzerhof, M. Generalized Gradient Approximation Made Simple. *Phys. Rev. Lett.* **1996**, *77* (18), 3865–3868.

(2-18) Martin, R. M. *Electronic Structure*, First edit.; Cambridge University Press: Cambridge, 2004.

(2-19) Perdew, J. P.; Burke, K.; Ernzerhof, M. Generalized Gradient Approximation Made Simple-ERRATA. *Phys. Rev. Lett.* **1996**, *77* (18), 3865–3868.

(2-20) Blöchl, P. E. Projector Augmented-Wave Method. *Phys. Rev. B* **1994**, *50* (24), 17953–17979.

(2-21) Kresse, G.; Hafner, J. Ab Initio Molecular Dynamics for Liquid Metals. *Phys. Rev. B* **1993**, *47* (1), 558–561.

(2-22) Kresse, G.; Hafner, J. Norm-Conserving and Ultrasoft Pseudopotentials for First-Row and Transition Elements. *J. Phys. Condens. Matter* **1994**, *6* (40), 8245–8257.

(2-23) Kresse, G.; Furthmüller, J. Efficiency of Ab-Initio Total Energy Calculations for Metals and Semiconductors Using a Plane-Wave Basis Set. *Comput. Mater. Sci.* **1996**, *6* (1), 15–50.

(2-24) Kresse, G.; Furthmüller, J. Efficient Iterative Schemes for Ab Initio Total-Energy Calculations Using a Plane-Wave Basis Set. *Phys. Rev. B - Condens. Matter Mater. Phys.* **1996**, *54* (16), 11169–11186.

(2-25) Kresse, G.; Joubert, D. From Ultrasoft Pseudopotentials to the Projector Augmented-Wave Method. *Phys. Rev. B* **1999**, *59* (3), 1758–1775.

(2-26) Broyden, C. G. A Class of Methods for Solving Nonlinear Simultaneous Equations. *Math. Comput.* **1965**, *19* (92), 577–577.

(2-27) Pulay, P. Convergence Acceleration of Iterative Sequences. the Case of Scf Iteration. *Chem. Phys. Lett.* **1980**, *73* (2), 393–398.

(2-28) Baldereschi, A. Mean-Value Point in the Brillouin Zone. *Phys. Rev. B* **1973**, *7* (12), 5212–5215.

(2-29) Monkhorst, H. J.; Pack, J. D. Special Points for Brillouin-Zone Integrations. *Phys. Rev. B* **1976**, *13* (12), 5188–5192.

CHAPTER 3

Theoretical Study of the Activity of $BaTiO_3$ as Solid Oxide Fuel Cell Electrocatalyst

3.1 INTRODUCTION

One recognizable feature of solid oxide fuel cells (SOFCs) is their fuel flexibility, covering hydrogen, ammonia,[1-4] synthesis gas,[5,6] biofuels,[7-11] oxygenates,[12,13] hydrocarbons,[14-18] carbon,[19,20] etc. In practical operation, most fuels contain impurities that may attack the active sites of the electrocatalysts decreasing the performance and often influence the long term durability of the SOFC. Thus, the need for a clean-up unit to remove the small concentration of impurities adds an extra cost and increases the footprint to the overall SOFC system.[21] Nickel-yttria-stabilized zirconia (Ni-YSZ) is the most typical anode for the electro-oxidation of H_2,[22] and it also shows a high activity for CH_4 reforming.[23] Under the SOFC operating conditions, sulfur compounds convert into H_2S in the course to the anode chamber.[24] It is reported that a few parts per million H_2S can severely limit the performance of the Ni-YSZ.[24-29] To understand the poisoning effect of sulfur on the anode properties, its interaction with Ni surfaces has been studied from a theoretical point of view; e.g., the interaction and sequential scission of H_2S on Ni(111) have been reported as an exothermic process with low activation energy, leading to a strong chemisorption of the sulfur atom on the Ni(111) surface.[29,30] Density functional theory (DFT) calculations combined with thermodynamic estimations show that the sulfur poisoning is fully recoverable before the formation of Ni_3S_2.[31] Furthermore, the effect of H_2S on the H_2 reaction with Ni(111) has been described using a DFT-based model[32,33] and first-principles adsorption thermodynamics,[34] showing an increment in the kinetic barrier for the H_2 adsorption and dissociation as the sulfur coverage increases. Likewise, adsorbed sulfur decreases the activity of the Ni(111) surface toward the H_2 activation,[35] which escalates as the sulfur coverage increased.[33]

To mitigate the effect of sulfur, the effects of alloying additions on sulfur adsorption on Ni-surfaces have been explored.[36] In addition to the Ni-based anode, oxides have been explored as potential materials. Among those materials, mixed ionic and electronic conductor oxides with perovskite structures have proved to be sulfur tolerant when used as SOFC anode.

Different elements are often doped to control a material's properties such as ionic conductivity, electronic conductivity, catalytic activity, and mechanical compatibility.[37] Materials like $La_xSr_{1-x}VO_{3-\delta}$ have showed stable performances without any significant deterioration during forty-eight hours test when the fuel is 5% H_2S-95% H_2.[38] $La_{0.4}Sr_{0.6}TiO_3$ doped with Ba has been reported, in the presence of H_2S, to promote the reforming reaction resulting in an increased power density by ca. twenty times when dry CH_4 containing 5000 ppm of H_2S is employed as fuel.[39] The same research group has published that undoped $BaTiO_3$ has a better performance than undoped $SrTiO_3$ and $La_2Ti_2O_7$ as anodes for SOFC when H_2 and dry CH_4 are employed as fuels. Once 5000 ppm H_2S is added to the fuels, the power density of the SOFC using $BaTiO_3$ anode increases ca. three times for H_2 fuel and ca. six times for CH_4 fuel. This increment can be attributed to the presence of sulfur at the surface as has been revealed by X-ray photoelectron spectroscopy (XPS) measurement.[40] Theoretical approaches have been also carried out to investigate the properties of perovskite oxides as materials for SOFCs; e.g., oxygen activation on stoichiometric and oxygen-deficient $SrTiO_3$[41] and $La_{1-x}Sr_xCoO_3$,[42] and the oxygen reduction reaction (ORR) on $La_{1-x}Sr_xCoO_3$,[43] where reaction mechanisms and kinetics have been targeted. On the other hand, there is a lack of theoretical studies regarding the interaction and possible reaction mechanisms of different fuels on perovskite materials when employed as SOFC anodes. In this study, DFT calculations are employed to examine the sulfidation of the $BaTiO_3(001)$ surfaces after reacting with H_2S, and the promoting effect of sulfur on the H_2 oxidation and the CH_4 sequential dissociation reactions.

3.2 COMPUTATIONAL PROCEDURE

All calculations performed in this study were based on the plane wave DFT method implemented in the Vienna Ab Initio Simulation Package (VASP 5.3.3).[44-46] Perdew−Burke−Ernzerhof parametrization of the generalized gradient approximation (GGA-PBE) was employed as exchange-correlation functional together with the projector augmented wave (PAW) method.[47] Spin-polarized calculations were performed throughout the study with a plane wave energy cutoff of 400 eV. The ions were fully relaxed toward equilibrium until the Hellmann-Feynman forces were less than 0.03 eV/Å. Tighter force convergence criteria (0.01 eV/Å) showed that the calculated adsorption energies are converged within 0.005 eV. The optimization of the cubic phase of bulk $BaTiO_3$ was performed with 8 × 8 × 8 Monkhorst-Pack *k*-point mesh for the Brillouin zone integration where all the atoms and the crystal volume were allowed to relax. After the optimization, the calculated lattice parameter of bulk $BaTiO_3$ (a = 4.00 Å) was the same as the experimental value (a = 4.00 Å).[48] Subsequently, two non-stoichiometric $BaTiO_3$(001) slabs were constructed to avoid dipole-dipole interaction between the BaO-terminated (BaO^T) and TiO_2-terminated (TiO_2^T) sides of the slabs.[49-51] Although, $BaTiO_3$ experience a range of surface reconstructions; (1×1), (2×1), c(2×2), (3×2), (6×1), (3×1), (√5×√5)R26.6°, and (√13×√13)R33.6°,[52-56] in this study the clean $BaTiO_3$(001) surfaces were employed as models because they can be a source of fundamental knowledge for this study as they have been extensively studied.[50,51,56-61] The nonstoichiometric BaO-BaO and TiO_2-TiO_2 slabs were modeled with nine alternating TiO_2 and BaO layers in a 2x2 supercell. Using symmetric slab models allow that the polarization occurring on one surface is cancelled by equal and opposite polarization on the other side of the slab.[62,63] The polarization arises because the charges of Ba-, and Ti-atoms do not necessarily fulfill the relationship $\delta_{Ti} = 2\delta_{Ba}$ (δ, symbolizes the charge).[62] The deviation of the static charges compared to their formula values (Ba^{2+}, Ti^{4+}, and O^{2-}) has been reported to be due to the mixed ionic and covalent bond character of the cation-oxygen bonds.[62,64] In $BaTiO_3$, the ionic/covalent Ti-O bond character varies rapidly as function of the bond length.[64]

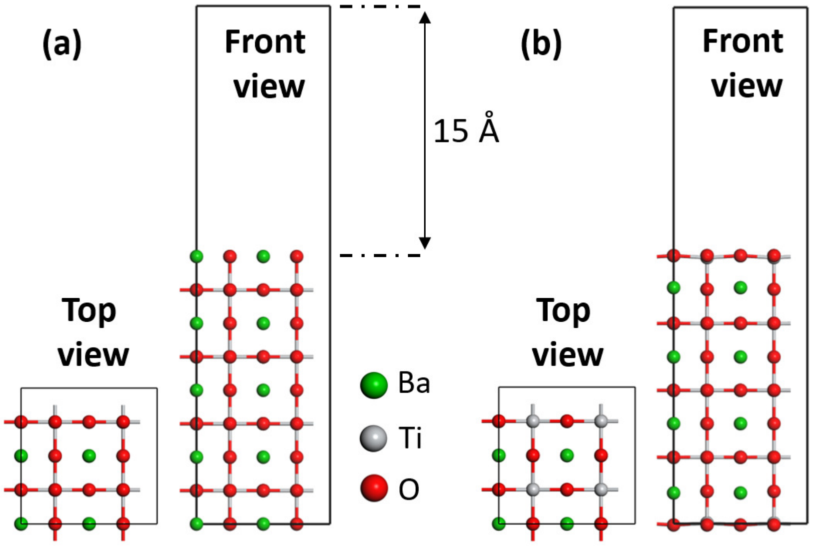

Figure 3-1. $BaTiO_3$(001) slabs: (a) top and front views of BaO-terminated slab, and (b) top and front views of TiO_2-terminated slab.

The slabs were optimized with 4 × 4 × 1 Monkhorst-Pack k-point mesh where the coordinates of the atoms in the middle three layers of the slabs were kept frozen while the coordinates of the atoms in the three top layers for both sides of the slabs were fully relaxed.

Increasing the number of layers to eleven showed that the calculated adsorption energies of H_2, H_2S, and CH_4 are converged within 0.05 eV, which does not change the conclusions in this work.

Increasing the supercell size from a 2×2 to a 3×3 supercell led to changes on the adsorption energies of H_2, H_2S, and CH_4 on the BaO^T in the range of 0.005 eV; on the other hand, on the TiO_2^T surface the adsorption energies of these species became less negative by 0.74 eV. Although there is a significant change in the adsorption energy of the TiO_2^T surface, the conclusions regarding the effect of sulfur will not be affected. The vacuum between the slabs was set to span a range of 15 Å to ensure no significant interaction between the slabs, as shown in Figure 3-1.

The adsorption energy of the adsorbates, E_{ads}, was defined as:

$$E_{ads} = \{E_{tot} - [E_{slab} + E_x]\}, \qquad (3\text{-}1)$$

where, E_{tot}, E_{slab}, and E_x are the total energies of the x adsorbate interacting with the pristine or sulfided surface (either BaO^T or TiO_2^T), and an isolated molecule, radical, or atom, respectively. The relative energy of the intermediates formed during the sulfidation process was calculated as the difference between their energy and the energy of the initial reactants (the $BaTiO_3$(001) surface without adsorbates and the isolated H_2S molecule). For the case of the CH_4 sequential dissociation, the relative energy was calculated as follows:

$$E_{rel} = [E_{tot} + y * (E_{H-slab})] - [E_{CH_4} + (y+1) * E_{slab}], \qquad (3\text{-}2)$$

where, E_{rel} is the relative energy of the $CH_{4\text{-}y}$ (y = 0, 1, 2, 3, and 4) species calculated with respect to the pristine or sulfided slabs (BaO^T and TiO_2^T) and a CH_4 molecule, E_{tot} is the total energy of the CH_y adsorbate interacting with the adsorbent surface, E_{H-slab} is the energy of a single H-atom interacting with the pristine or sulfided slabs, E_{CH_4} is the energy of the free CH_4 molecule, y is the number of H-atoms stripped from the CH_4 molecule, and E_{slab} is the energy of the surface without adsorbates, either pristine or sulfided BaO^T or TiO_2^T. In all cases, a negative value of the adsorption and relative energies denotes a stable interaction. In order to assess the trend in stability change of the overall chemical reaction, the intermediate states were calculated without the transition state search.

3.3 RESULTS AND DISCUSSION

3.3.1 Sulfidation Pathways of $BaTiO_3$(001) Surfaces.

3.3.1.1 Sulfidation of BaO^T Surface. The reaction pathways for the sulfidation of the BaO^T surface are shown in Figure 3-2.

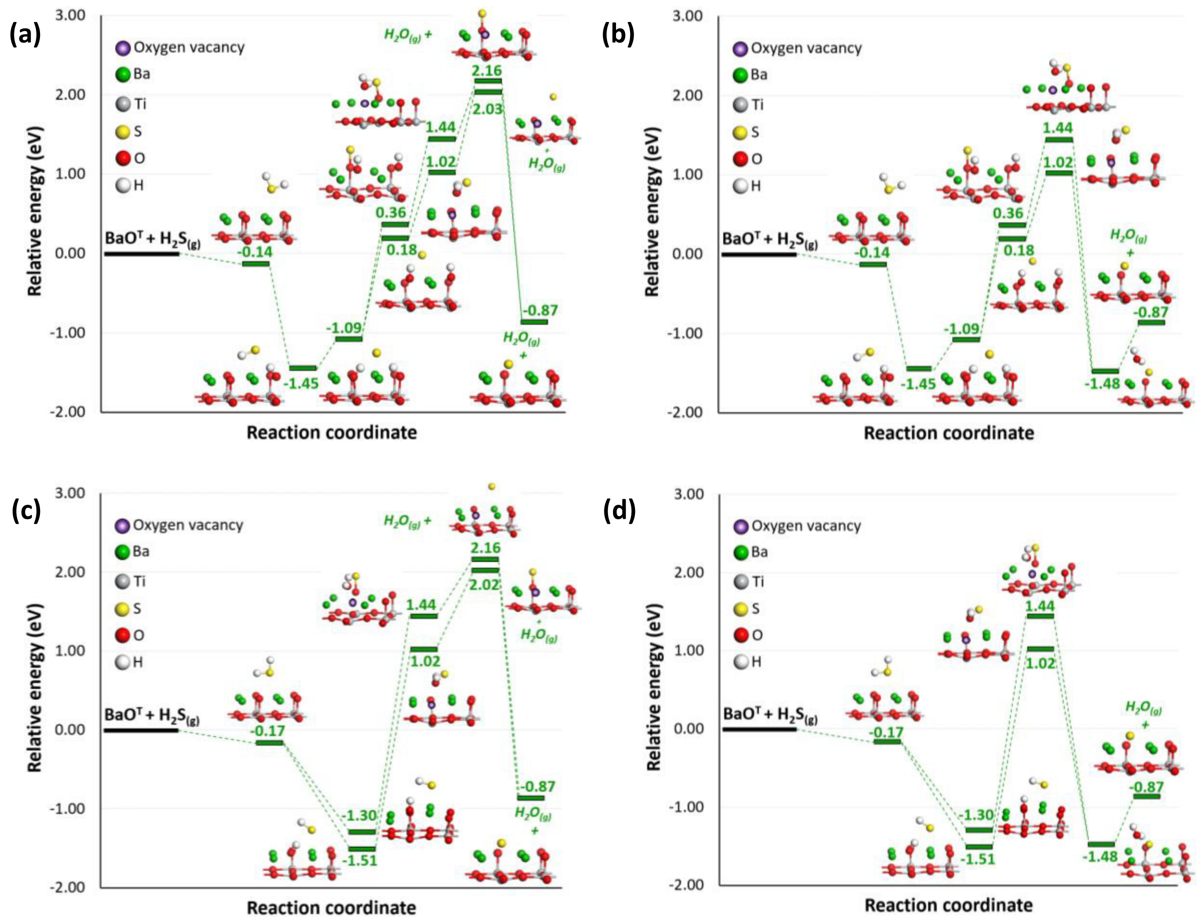

Figure 3-2. Reaction pathways for sulfidation of BaO-terminated surface: (a) first, (b) second, (c) third, and (d) fourth reaction pathways.

The first reaction pathway that leads to the sulfidation of the BaO^T surface is shown in Figure 3-2(a), and it started with the adsorption of the H_2S molecule. The calculated adsorption energy on the BaO^T surface was -0.14 eV. Successively, the molecule dissociated exothermically into HS and H-atom; the latter bonded with a surface O-atom to form OH. The relative energy for the first dissociative adsorption was -1.45 eV. The subsequent dissociation of HS on the BaO^T surface led to the formation of a new OH with the S-atom located between the H-atoms of the two formed OHs. This configuration had an energy value of -1.09 eV. Next, the S-atom diffused to interact between two Ba-atoms or on top of an O-atom with relative energies of 0.18 and 0.36 eV, respectively. The succeeding reaction intermediate was the formation of H_2O that desorbed from the surface and partially created an oxygen vacancy, while the S-atom interacted between two Ba-atoms, or with an O-atom with energies of 1.02 and 1.44 eV, respectively. The complete desorption of the H_2O molecule from the BaO^T surface, which was associated with the formation of an oxygen vacancy, was unstable. The relative energy for the complete desorption of H_2O, on the BaO^T surface, was 2.03 eV when the S-atom was located between two Ba-atoms and 2.16 eV when the S-atom was positioned on top of a surface O-atom. Lastly, the adsorbed S-atom moved to occupy the oxygen vacancy, hence stabilizing the surface; the relative energy corresponding to the sulfided BaO^T surface was -0.87 eV. Although the result showed a high positive value for the desorption of H_2O, hence forming an oxygen vacancy in the surface, this value was expected for the formation of oxygen vacancies; e.g., previous DFT studies have shown that under high oxygen potential conditions the oxygen vacancy formation is energetically demanding, i.e., 5.03 eV on bulk $BaTiO_3$[65] and for the case of $BaTiO_3(001)$ surfaces, 5.06 eV for the BaO^T surface and 4.06 eV for the TiO_2^T surface.[66] The theoretical oxygen vacancy energy formation on the $BaTiO_3(001)$ surfaces was calculated as follows:

$$E_{form}^{Vo}(A) = [E_{slab}^{Vo}(A) + \frac{1}{2}E(O_2) - E_{slab}(A)], \tag{3-3}$$

where $E_{form}^{Vo}(A)$ is the oxygen vacancy formation energy in the BaO^T or TiO_2^T surface, E_{slab}^{Vo} is the energy of an optimized slab missing an O-atom on the surface, and $E(O_2)$ is the energy of an isolated O_2 molecule, respectively. The results, 4.50 eV for the BaO^T and 3.48 eV for the TiO_2^T, agree with the more stable formation of an oxygen vacancy in the TiO_2^T than of the BaO^T surface by approximately 1.00 eV as mentioned in a previous work.[66] Furthermore, previous DFT studies have also shown that the oxygen vacancy formation in bulk $BaTiO_3$[65] and on the $BaTiO_3(001)$ surfaces[66] become stable under reducing conditions. This is in agreement with experimental works[67,68] where the decrease in the oxygen partial pressure leads to the formation of the oxygen vacancy and increase of the electrical conductivity (n-type conduction) of $BaTiO_3$. Therefore, in order to discuss the results of this study in a more realistic situation, the dependence of the oxygen vacancy formation energy was estimated taking into consideration the effect of temperature (1200 K, operating temperature in the $BaTiO_3$ based SOFC)[40] and oxygen partial pressure (10^{-19} atm, typical operating pressure in the anode side).[69-72] The Gibbs free energy for the formation of the oxygen vacancy was calculated as follows:

$$\Delta g_{form}^{Vo}(A) = E_{form}^{Vo}(A) + \Delta\mu_o(T, pO_2), \tag{3-4}$$

where $\Delta\mu_o(T, pO_2)$ corresponds to changes in the chemical potential for O-atom and it was calculated as in literature.[73] This work calculated Gibbs free energies for the oxygen vacancy formation were 1.96 eV for the BaO^T surface and 0.67 eV for the TiO_2^T surface. In a similar way, the effect from the oxygen chemical potential was added to the intermediate states that involve the formation of an oxygen vacancy after the H_2O desorption to the gas phase. Then, for the BaO^T surface, the formation energy of an oxygen vacancy decreased from 2.03 to -0.51 eV (for the S-atom between two Ba-atoms), and from 2.16 to -0.38 eV (for the S-atom on top of surface O-atom). Thus, the H_2O desorption and oxygen vacancy formation became thermodynamically stable. In this paper, the effect of the chemical potential is an approximation used to show how the energy can be decreased taking into consideration the operating conditions. This consideration was only employed for the complete formation of an oxygen vacancy (total desorption of the H_2O molecule from the surfaces), the effect of the oxygen chemical potential on the partial formation of the oxygen vacancy (H_2O molecule still physisorbed or chemisorbed on the surfaces) was not addressed. The second reaction pathway is shown in Figure 3-2(b). This pathway and the first one had the same reaction intermediates from the adsorption of H_2S until the H_2O formation. The following step led to the S-atom occupying the vacancy left by the O-atom after the H_2O was formed and moved to interact with its O-atom between two Ba-atoms. The relative energy for this configuration had a value of -1.48 eV. Then, the H_2O desorbed to the gas phase leaving the sulfided BaO^T surface.

The third reaction pathway is shown in Figure 3-2(c). The adsorption energy for the H_2S had an energy of -0.17 eV. The first dissociation of H_2S led to OH and HS pair with energy values that varied from -1.51 to -1.30 eV depending on the distance between the OH and HS pair. In the next step, the remaining H-S bond was broken to form H_2O while the S-atom moved between two Ba-atoms (1.02 eV) or on top of an O-atom (1.44 eV). The H_2O desorption occurred for the previous two configurations (between two Ba-atoms, and on top of an O-atom) with energies of 2.02 and 2.16 eV, respectively. These values corresponding to the oxygen vacancy formation were decreased by taking into consideration the effect of pressure and temperature at the operating conditions of the SOFC to -0.52 and -0.38 eV for the S-atom between two Ba-atoms, and for the S-atom on top of an O-atom, respectively. The next step corresponding to the sulfidation of the BaO^T surface had a value of -0.87 eV.

The last reaction pathway shared the initial reaction intermediates with the previous one and is shown in Figure 3-2(d). From the adsorption energy to the H_2O formation the reaction intermediates were the same. Once H_2O was formed, the S-atom occupied the place of the O-atom used to form the H_2O molecule. The formed H_2O had its O interacting with one of the Ba-atoms. The relative energy for this configuration was -1.48 eV. Lastly, the H_2O desorbed to the gas phase leaving the sulfided BaO^T surface, which had a stable energy of -0.87 eV.

To summarize, the sulfidation of the BaO^T surface can occur via the formation of an oxygen vacancy after the complete desorption of H_2O, or without the formation of the oxygen vacancy (as the H_2O started to desorb, the S-atom took the place of the missing O-atom). For the proposed pathways, the intermediate configurations where the S-atom was interacting with the Ba-atoms were the most stable, and the energy difference between those intermediates was smaller than the ones when the S-atom was interacting with a surface O-atom. Therefore, for the latter case, the increased energy differences between reaction intermediates will represent higher activation energy values, hence decreasing the likelihood of the reaction to occur.

3.3.1.2 Sulfidation of TiO_2^T surface. The sulfidation of the TiO_2^T surface can proceed via two reaction pathways that are shown in Figure 3-3.

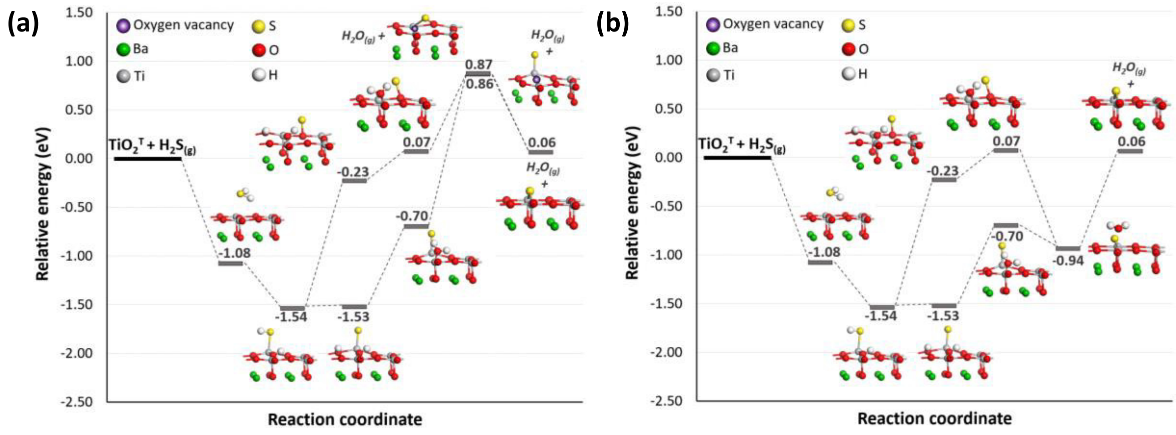

Figure 3-3. Reaction pathway for sulfidation of TiO_2-terminated surface: (a) first, and (b) second reaction pathways.

The first reaction pathway started with the adsorption of H_2S with an energy of -1.08 eV. Successively, the molecule dissociated exothermically into HS with the S-atom on top of a Ti-atom and the remaining H-atom bonded with a surface O-atom to form OH. The first dissociation had a relative energy of -1.54 eV. The subsequent dissociation of the HS led to the formation of two OHs and the remaining S-atom located on top of a surface Ti-atom; the relative energy was -1.53 eV. Similarly, the S-atom interacted on top of a surface O-atom; however, this configuration is more unstable, with an energy value of -0.23 eV. Next, H_2O was formed, where the S-atom bonded on top of a surface Ti-atom was more stable (-0.70 eV) than when the S-atom bonded to a surface O-atom (0.07 eV). The complete desorption of the H_2O molecule from the TiO_2^T surface, which was associated with the formation of an oxygen vacancy, was unstable. The lowest energy, 0.86 eV, was calculated when the S-atom bonded on top of a Ti-atom, and the relative energy increased to 0.87 eV when the S-atom bonded between an O-atom and a Ti-atom. By taking into consideration the oxygen chemical potential, the energies for the H_2O desorption decreased from 0.86 to -1.95 eV when the S-atom bonded on top of a Ti-atom, and from 0.87 to -1.94 eV when the S-atom bonded between an O- and a Ti-atoms. Hence, the oxygen vacancy formation after the H_2O desorption was thermodynamically stable. Lastly, the adsorbed S-atom moved to occupy the oxygen vacancy, hence stabilizing the surface; the relative energy corresponding to the sulfided TiO_2^T surface was 0.06 eV.

The second reaction pathway shared some of the reaction intermediates with the first one. The difference arose after H_2O was formed. Instead of desorbing as in the first reaction pathway, the H_2O bonded with its O-atom on top of the closest Ti-atom from the surface, while the S-atom occupied the vacancy left by the O-atom. This configuration had a relative energy of -0.94 eV. The complete desorption of the H_2O had a relative energy of 0.06 eV, similar to the first reaction pathway leading to the sulfided TiO_2^T.

To summarize, just as in the case of the sulfidation of the BaO^T surface, the sulfidation reaction of the TiO_2^T surface can occur via the formation of an oxygen vacancy or without the oxygen vacancy. The latter had the smaller energy difference between each of the reaction intermediates, especially when the S-atom was located on top of a Ti-atom; as a result, the activation energy to form that intermediate is expected to be lowest one, hence increasing the probability for the sulfidation of the TiO_2^T surface to occur.

3.3.2 Hydrogen Oxidation Reaction on $BaTiO_3$(001) Surfaces. The reaction pathways for the HOR on the $BaTiO_3$(001) surfaces are shown in Figure 3-4.

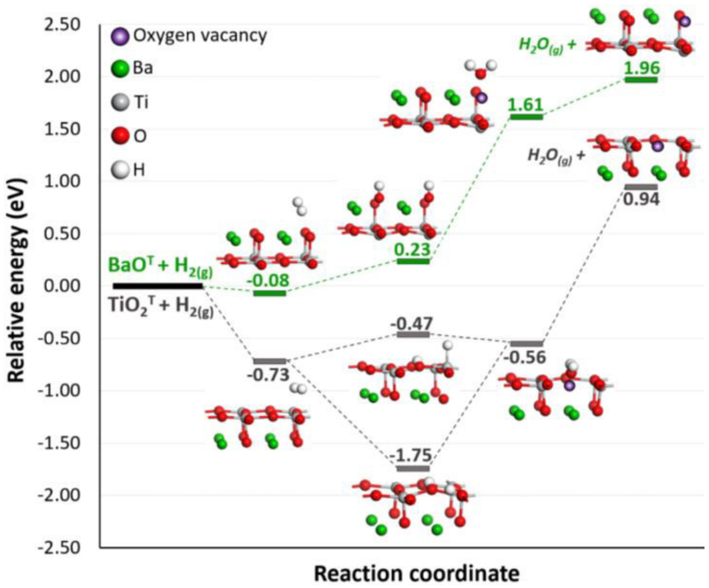

Figure 3-4. Reaction pathways for H_2 oxidation on pristine $BaTiO_3(001)$ surfaces: BaO-terminated (green lines) and TiO_2-terminated (gray lines) surfaces. Only the surface and subsurface layers are shown.

The H_2 adsorption on both surfaces was shown to be exothermic with values of -0.08 eV on the BaO^T surface and -0.73 eV on the TiO_2^T surface. After its adsorption, the H_2 molecule dissociated, and each H-atom bonded with an O-atom of the surface to form two OHs. The results in this work showed that the TiO_2^T surface was more active to break the H-H bond, as the dissociative adsorption energy of H_2 was 0.23eV on the BaO^T surface, and -1.75 eV on the TiO_2^T surface. The main difference arose from the partial formation of oxygen vacancies on the BaO^T surface as result of the H-atom interaction with the surface O-atom that led to the upper shift of the O-atom position by 0.86 Å. For the TiO_2^T surface, the dissociation of the H_2 molecule also led to the formation of one OH and the remaining H-atom bonded on top of the closest surface Ti-atom; this intermediate had a relative energy of -0.47 eV. Next, the H_2O molecule was formed after one of the H-atoms diffused to bond with the already formed OH. The calculated relative energy for the H_2O formation was 1.61 eV on the BaO^T surface and -0.56 eV on the TiO_2^T surface. The high H_2O formation energy was due to the partial formation of an oxygen vacancy after the H_2O molecule started to desorb to the gas phase. Lastly, the final products, i.e., the oxygen-deficient surfaces and H_2O in the gas phase, had relative energies of 1.96 eV for the BaO^T surface and 0.94 eV for the TiO_2^T surface. In the same way described for the sulfidation process, the effect of the oxygen chemical potential at the chosen operating conditions of the SOFC was considered; thus the energy corresponding to the H_2O desorption from the surface to the gas phase and therefore the formation of the oxygen vacancy was decreased to -0.58 eV for the BaO^T surface and to -1.87 eV for the TiO_2^T surface. Although the final products are stabilized under the SOFC operating conditions, the activation energy to form each intermediate is expected to be relatively large as the difference in energy between the intermediates was considerable. This reaction mechanism is different to the HOR on Ni-YSZ involving charge-transfer reactions such as the OH^- formation on YSZ due to H-atom migration from the Ni-atom to YSZ, the subsequent H_2O formation as result of H-atom migration from the Ni-atom to the formed OH^- on YSZ, and O^{2-} migration from YSZ to the Ni-particle. A low activity showed to be kinetically governed by competitive H-atom and O^{2-} migration, where decreasing the kinetic barrier of O^{2-} migration from YSZ to the Ni-particle led to higher activity.[74]

3.3.3 Effect of Sulfidation of $BaTiO_3(001)$ Surfaces on Hydrogen Oxidation Reaction.

To avoid dipole-dipole interaction, mirrored sulfided BaO and TiO_2 slabs were employed to assess the effect of sulfur on the HOR. The reaction pathways for the HOR on the sulfided $BaTiO_3(001)$ surfaces are shown in Figure 3-5.

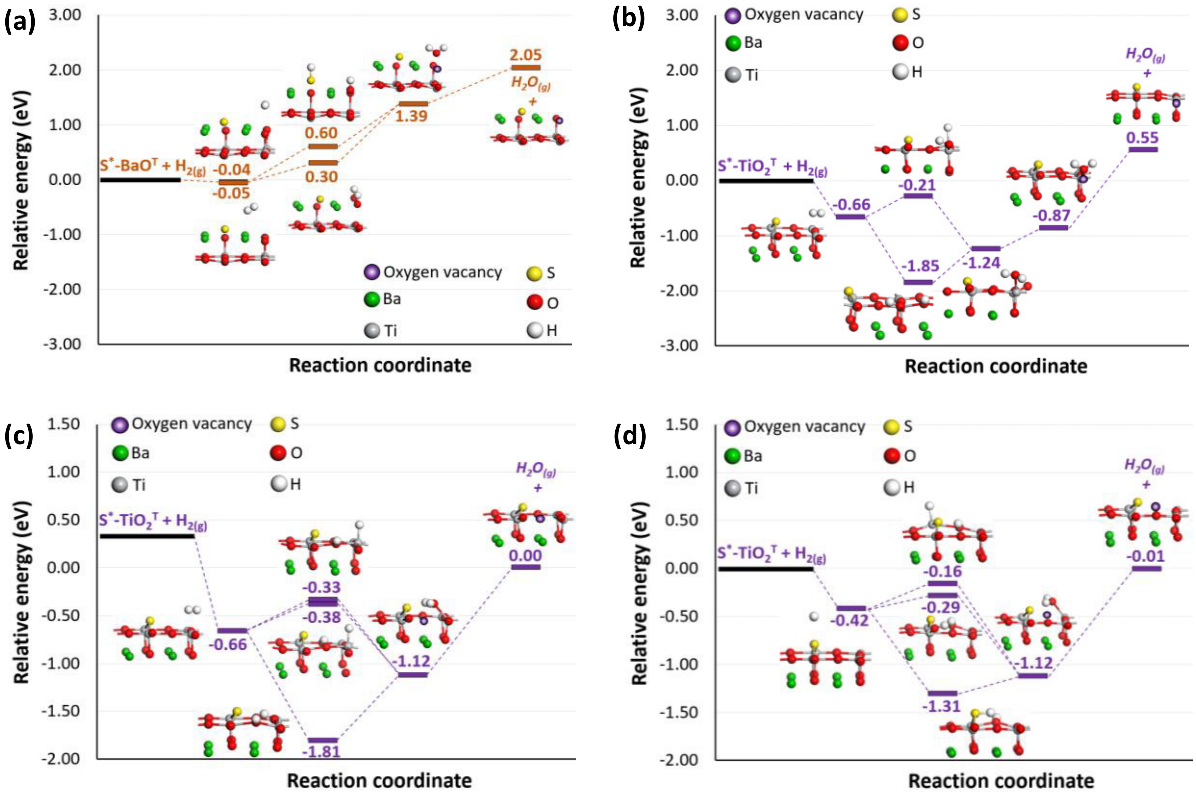

Figure 3-5. Reaction pathways for H_2 oxidation on sulfided $BaTiO_3(001)$ surfaces: (a) BaO-terminated surface, (b-d) TiO_2-terminated surface. Only the surface and subsurface layers are shown.

The presence of sulfur on the BaO^T surface is shown in Figure 3-5(a). The calculated adsorption energy of H_2 molecule was -0.04 eV for the adsorption between two O-atoms, and it was -0.05 eV for the adsorption between S- and O-atoms. Comparing the results in Figures 3-4 and 3-5, the influence of sulfur on the molecular adsorption was found to be small. The sulfidation of the BaO^T surface had a small increase in the dissociation of the H_2 molecule to form two OHs, resulting in a dissociative adsorption energy of 0.30 eV. Similarly to the pristine surface, the partial formation of the oxygen vacancies by the interaction of H-atoms influenced considerably the endothermic dissociation. Moreover, the presence of sulfur on the BaO^T surface led to a new intermediate for the dissociated H_2 molecule, i.e., the formation of OH and HS pair. This new intermediate was less stable than the intermediate with two OH species by 0.30 eV; its relative energy was 0.60 eV. Next, the formation of H_2O was promoted on the sulfided BaO^T surface; the relative energy decreased from 1.61 eV on the pristine surface to 1.39 eV due to the presence of sulfur. Lastly, the calculated relative energy, 2.05 eV, for the complete desorption of H_2O from the sulfided BaO^T surface had a small increase of 0.09 eV. By including the effect of the oxygen chemical potential under the operating conditions of the SOFC, the energy for the formation of the oxygen vacancy after H_2O desorbed to the gas phase was decreased to -0.49 eV.

The effect of sulfur on the HOR over the sulfided BaO^T surface can be summarized as follows: First, it stabilized the formation of the H_2O molecule and the partial formation of an oxygen vacancy. Second, it led to the formation of a new reaction intermediate after the H_2 dissociation. Although its formation was not stable due to the partial formation of oxygen vacancies, under the SOFC operating conditions this energy was calculated to be stable. Additionally, by having different intermediates the activation energy for the rate-determining steps can be decreased, which may lead to faster kinetics. Third, no significant detrimental effect was perceived for the formation of the reaction intermediates. The promoting effect, the formation of another intermediate, and insignificant detrimental effects of the surface sulfur on the BaO^T surface in part can explain the increased performance of $BaTiO_3$ anode working with H_2 containing H_2S.[40] The nature of the mentioned interactions is unique in contrast to the negative effect of adsorbed sulfur on the Ni anode.[32,33,35]

On the other hand, the presence of sulfur on the TiO_2^T surface led to the formation of different intermediates after the H_2 molecule interacted with the surface; hence the reaction will occur via mechanisms different from that on the pristine surface. In this work, three different reaction pathways were analyzed as shown in Figure 3-5.

The first possible reaction pathway is shown in Figure 3-5(b), which started with the H_2 molecular adsorption on top of a Ti-atom, with the adsorption energy of -0.66 eV. Next, the dissociation of the molecule occurred exothermically to form two OHs on the surface with a relative energy of -1.85 eV; note that this energy is lower than that for the pristine surface by 0.10 eV. Besides the formation of two OHs, the splitting of H_2 led to the formation of OH and HTi pair with a relative energy of -0.21 eV. After the H_2 dissociation, H_2O was formed and bonded with its O-atom to the closest Ti-atom with a relative energy of -1.24 eV. As the H_2O desorption to the gas phase occurred, the energy changed from -1.24 to -0.87 eV. As in the case of the formation of the two OHs, the presence of sulfur had a stabilizing effect on the formation and initial desorption of H_2O. The complete desorption of H_2O associated with the oxygen vacancy formation was an endothermic reaction with a relative energy of 0.55 eV; this value was 0.39 eV more stable than for the pristine TiO_2^T surface.

The second possible reaction pathway is shown in Figure 3-5(c). The first reaction intermediate had the same configuration of the H_2 molecule adsorbed on top of a Ti-atom, with an adsorption energy of -0.66 eV. Next, just as in the mechanism explained above, the dissociation of the molecule occurred exothermically to form two OHs on the surface with a relative energy of -1.81 eV. The splitting of H_2 also led to the formation of OH and HTi pair, with a relative energy ranging from -0.38 to -0.33 eV. The formation of these intermediates was more unstable than on the pristine TiO_2^T surface by 0.09 and 0.14 eV, respectively. Through the diffusion of one of the H-atoms, H_2O was formed, which located with its O-atom interacting with one of the surface Ti-atoms. This configuration had a relative energy of -1.12 eV. The complete desorption of the formed H_2O led to an oxygen vacancy closer to the S-atom with a relative energy of 0.00 eV. Based on the values of the relative energy for the oxygen vacancy formation, the presence of sulfur had a stabilizing effect as the energy decreased from 0.94 eV for the pristine TiO_2^T surface to 0.55 or 0.00 eV for the sulfided TiO_2^T surface depending on where the oxygen vacancy was formed. These values were decreased to -2.26 or -2.81 eV, respectively, by employing the oxygen chemical potential approximation, making the oxygen vacancy formation stable.

The third reaction pathway for the HOR is shown in Figure 3-5(d). This reaction started with the H_2 molecule adsorbed on top of one of the Ti-atoms closest to the S-atom; the molecule's adsorption energy was -0.42 eV. The most stable intermediate for the H_2 dissociation led to the formation of OH and SH pair with an energy of -1.31 eV this being the least stable dissociation on the sulfided TiO_2^T surface, it was 0.44 eV more unstable than the pristine TiO_2^T surface. The second stable intermediate for the H_2 dissociation was the formation of two OHs that had a relative energy of -0.29 eV. The third and the least stable pair formed after the H_2 dissociation was OH and H-atom bonded on top of a Ti-atom with a relative energy of -0.16 eV. The formation of H_2O was the subsequent step, in which the H_2O molecule was adsorbed on top of a Ti-atom with a relative energy of -1.12 eV. Lastly, the H_2O desorbed to the gas phase forming an oxygen vacancy close to the S-atom with a relative energy of -0.01 eV, which was decreased to -2.82 eV by taking into consideration the effect of the oxygen chemical potential making the oxygen vacancy formation on the sulfided TiO_2^T surface stable. The effect of sulfur on the HOR was more evident on the TiO_2^T surface than on the BaO^T surface, due to the promotion of the H_2 dissociation into two OHs, promotion of H_2O formation, desorption, and hence oxygen vacancy formation. Additionally, the presence of sulfur provided alternative sequences of elementary steps to accomplish the HOR. In some cases the change in energy between reaction steps was smaller than for the HOR on the pristine surface; hence it is also probable that the energy to overcome the barriers would also be smaller. By having multiple elementary steps with lower activation energies rather than a few steps with high barriers, the reaction kinetics will be enhanced, hence increasing the performance of the SOFC working with $BaTiO_3$ as anode after H_2S introduction into the fuel.[40] This type of behavior is opposite to the effect of adsorbed sulfur on the H_2 dissociation on Ni surfaces.[32,33,35]

3.3.4 Effect of Sulfidation of $BaTiO_3(001)$ Surfaces on CH_4 Sequential Decomposition.

Similarly to the HOR, mirrored sulfided slabs were used for the CH_4 sequential decomposition. The relative energies of the sequential stripping of H-atoms from the CH_4 molecule were calculated employing equation 3-2. In Figure 3-6 are shown the most stable species of the sequential H-atom dissociation from CH_4 on the sulfided $BaTiO_3(001)$ surfaces. In order to directly compare and assess the effect of S-atom on the CH_4 sequential dissociation, only the most stable adsorbed species were taken into consideration and directly compared against their corresponding configuration on the pristine $BaTiO_3(001)$ surfaces. The interactions and stability of all the CH_y species and H-atom were explained in terms of their adsorption energies and are summarized in Table 1. The adsorption energy of the CH_4 molecule on the sulfided BaO^T surface was -0.04 eV, which was less stable than its adsorption on the sulfided TiO_2^T surface with the energy of -0.57 eV. The presence of sulfur on both surfaces made the adsorption of the molecule unstable by 0.02 and 0.12 eV for the BaO^T and TiO_2^T surface, respectively. The first dissociation of CH_4 on the sulfided BaO^T surface led to CH_3 bonded with the S-atom, which moved upward by 0.46 Å and partially formed an oxygen vacancy due to the interaction with CH_3; the relative energy of this configuration was ca. 1.35 eV, which is 0.13 eV more unstable than the pristine BaO^T surface. On the other hand, for the sulfided TiO_2^T surface, the first C-H bond breaking had a relative energy of -1.80 eV, where the CH_3 bonded with the S-atom that moved upward by 0.41 Å forming an oxygen vacancy as a result of the interaction with CH_3.

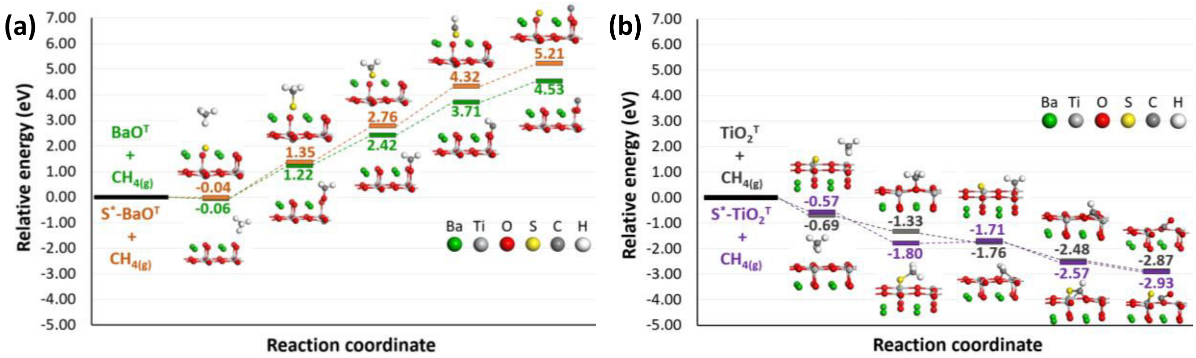

Figure 3-6. Energy diagrams for CH_4 sequential decomposition on $BaTiO_3(001)$ surfaces: (a) pristine (green lines) and sulfided (orange lines) BaO-terminated surfaces; (b) pristine (gray lines) and sulfided (purple lines) TiO_2-terminated surfaces. Only the surfaces and subsurfaces are shown.

The presence of sulfur on the TiO_2^T surface activated the CH_4 molecule decreasing the relative energy of its first dissociation from -1.33 to -1.80 eV. The dissimilarities in energy between the $BaTiO_3(001)$ surfaces arose mainly from the smaller formation energy of an oxygen vacancy on the TiO_2^T surface than on the BaO^T surface; additionally quantifying the relative energy (as in equation 3-2) requires the energy value of the interaction of a single H-atom, which for the BaO^T surface was more unstable than for the TiO_2^T surface by 1.39 and 1.42 eV for the pristine and sulfided surface, respectively. Next, breaking the second C-H bond on the BaO^T surface led to CH_2 with its C-atom interacting with the two Ba-atoms below, and with the S-atom that moved upward from the surface by 0.28 Å. The relative energy of this configuration was 2.76 eV, where the presence of sulfur had a detrimental effect of 0.34 eV for the CH_2 interaction with the sulfided BaO^T surface. For the case of the sulfided TiO_2^T surface, stripping the second H-atom led to CH_2 to bond with its C-atom to a surface O-atom and Ti-atom. The relative energy of this configuration was -1.71 eV, which had a minor detrimental effect compared with the pristine TiO_2^T surface of 0.05 eV. The next scission of an H-atom led to CH interacting with the two closest Ba-atoms and with the S-atom from the sulfided BaO^T surface. The relative energy of 4.32 eV was 0.61 eV more unstable than that of the pristine BaO^T surface. The decrease in the stability of CH on the sulfided BaO^T surface after interacting with the S-atom was linked to the rise in its adsorption energy as presented in Table 1. Removing the third H-atom on the sulfided TiO_2^T led to CH with its C-atom positioned between O-, Ti- and S-atoms from the surface. This configuration had a relative energy of -2.57 eV, which was 0.09 eV less than the energy on the pristine TiO_2^T surface. Lastly, removing the remaining H-atom gave a relative energy of 4.53 eV and led to C-atom on top of an O-atom from the sulfided BaO^T surface. This configuration was 0.68 eV more unstable than that on the pristine surface. On the sulfided TiO_2^T, dissociating the last C-H bond had a relative energy of -2.93 eV, which was 0.06 eV more stable than that of the pristine TiO_2^T surface. Breaking the last C-H bond led to the formation of CO that displaced from the surface by 0.94 Å, the CO formation on the sulfided TiO_2^T surface is more stable than on the pristine surface, as shown from their adsorption energies. The C-atom deposition may be suppressed on the sulfided TiO_2^T surface due to the endothermicity of the process from CH_3 to CH_2, or favorable formation of CO molecule. In Table 1 are summarized the adsorption and relative energies of the CH_y species and H-atom on the pristine and sulfided $BaTiO_3(001)$ surfaces.

Table 3-1. Relative (E_{rel}) and adsorption (E_{ads}) energies of the CH_y species and H-atom interacting with the pristine and sulfided $BaTiO_3(001)$ surfaces. All energies are in eV.

Adsorbate	E_{rel}^{BaO}	$E_{rel}^{*\,BaO}$	E_{ads}^{BaO}	$E_{ads}^{*\,BaO}$	$E_{rel}^{TiO_2}$	$E_{rel}^{*\,TiO_2}$	$E_{ads}^{TiO_2}$	$E_{ads}^{*\,TiO_2}$
CH_4			-0.06	-0.04			-0.69	-0.57
CH_3	1.22	1.35	-1.19	-1.12	-1.33	-1.80	-2.34	-2.85
CH_2	2.42	2.76	-2.65	-2.42	-1.76	-1.71	-4.04	-4.04
CH	3.71	4.32	-3.93	-3.49	-2.48	-2.57	-5.92	-6.09
C	4.53	5.21	-4.46	-4.00	-2.87	-2.93	-6.26	-6.44
H			-2.32	-2.26			-3.71	-3.68

E^*, corresponds to the energies on the respective sulfided surface

From Table 1, it can be concluded that sulfur on the BaO^T surface had a minor destabilizing effect on the interaction of CH_4, CH_3, and H-atom. For the interaction of CH_2, CH, and C-atom, the presence of sulfur made their interaction more unstable, hence making the C-atom deposition on the BaO^T surface less probable. On the other hand, for the TiO_2^T surface, the presence of sulfur stabilized the interaction of CH_3, CH, and C-atom by making their adsorption energies more negative. Similarly to the effect of sulfur on the BaO^T surface, the interaction of H-atom with the sulfided TiO_2^T surface suffered a minor decrease in its stability. To summarize, the sulfided TiO_2^T surface activated the dissociation of some C-H bonds of the CH_4 molecule, due to the endothermic process from CH_3 to CH_2, and promoted CO formation; C-atom deposition may be avoided, which is opposite to the poisoning effect of sulfur on the CH_4 dissociation over sulfur-adsorbed Ni surfaces.[33,35] This promoting effect of sulfur agrees well with experimentally reported performance enhancement of $BaTiO_3$ anode fueled with H_2S-containing CH_4.[40]

3.4 CONCLUSIONS

In this chapter, DFT method was adopted to investigate the activity of $BaTiO_3$ as SOFC electrocatalyst. The activity of $BaTiO_3$ was approximated by the reaction of H_2S, H_2 and CH_4 on $BatiO_3(001)$ surfaces. The sulfidation process of the $BaTiO_3$ catalyst will occur by exchanging the S-atom from the H_2S molecule with an O-atom from the surface. This exchange involves either the partial or total formation of an oxygen vacancy, which was calculated to be stable at the operating conditions of the SOFC. Similarly, the HOR involves the formation of an oxygen vacancy. The results from the H_2 reaction on $BaTiO_3(001)$ surfaces showed an increased energy difference between the intermediates, thus this reaction is expected to proceed slowly because the activation energy of each intermediate is expected to be even larger than the energy difference between intermediates. The slow kinetics can explain the poor initial performance of the SOFC employing $BaTiO_3$ as anode material.

Moreover, for the HOR, the presence of sulfur promoted the formation of some reaction intermediates, led to form different molecular entities by providing alternative sequences of elementary steps for the reaction to occur, and activated the H-H bond breaking. The above mentioned effects due to the presence of sulfur are contrary to that on the H_2 dissociation on Ni surfaces.

Due to the presence of sulfur the first C-H bond will be activated depending on the termination of the $BaTiO_3$ surface. On the TiO_2^T surface, sulfur stabilized the species formed after sequentially stripping the H-atoms from the CH_4 molecule, especially for the case of CH_3 activating the first bond breaking of the CH_4 molecule making the reaction exothermic. Additionally, the endothermic reaction from CH_3 to CH_2 and promoted CO formation will lead to the suppression of C-atom deposition. On the BaO^T surface, the presence of sulfur made the deposition of C-atom less probable, and no significant detrimental effect on the CH_4

activation was observed. The above-mentioned effects agree well with the experimentally reported performance enhancement of a $BaTiO_3$ anode fueled with H_2S-containing CH_4.

REFERENCES

(3-1) Cairns, E. J.; Simons, E. L.; Tevebaugh, A. D. Ammonia–Oxygen Fuel Cell. *Nature* **1968**, *217*, 780-781.

(3-2) Sigal, C. T.; Vayenas, C. G. Ammonia Oxidation to Nitric Oxide in a Solid Electrolyte Fuel Cell. *Solid State Ionics* **1981**, *5*, 567-570.

(3-3) Wojcik, A.; Middleton, H.; Damopoulos, I.; Van Herle, J. Ammonia as a Fuel in Solid Oxide Fuel Cells. *J. Power Sources* **2003**, *118*, 342-348.

(3-4) Ma, Q.; Peng, R.; Lin, Y.; Gao, J.; Meng, G. A High-Performance Ammonia-Fueled Solid Oxide Fuel Cell. *J. Power Sources* **2006**, *161*, 95-98.

(3-5) Drewery, M.; Kennedy, E.; Alenazey, F.; Dlugogorski, B.; Stockenhuber, M. The Effect of Synthesis Gas Composition on the Performance of Ni-Based Solid Oxide Fuel Cells. *Chem. Eng. Res. Des.* **2015**, *101*, 22-26.

(3-6) Sun, Y. F.; Li, J. H.; Chuang, K. T.; Luo, J. L. Electrochemical Performance and Carbon Deposition Resistance of Ce-Doped $La_{0.7}Sr_{0.3}Fe_{0.5}Cr_{0.5}O_{3-\delta}$ Anode Materials for Solid Oxide Fuel Cells Fed with Syngas. *J. Power Sources* **2015**, *274*, 483-487.

(3-7) Qin, H.; Zhu, Z.; Liu, Q.; Jing, Y.; Raza, R.; Imran, S.; Singh, M.; Abbas, G.; Zhu, B. Direct Biofuel Low-Temperature Solid Oxide Fuel Cells. *Energy Environ. Sci.* **2011**, *4*, 1273-1276.

(3-8) Kirtley, J. D.; Pomfret, M. B.; Steinhurst, D. A.; Owrutsky C.; Walker, R. A. Toward a Working Mechanism of Fuel Oxidation in SOFCs: *in situ* Optical Studies of Simulated Biogas and Methane. *J. Phys. Chem. C* **2015**, *119*, 12781-12791.

(3-9) Papurello, D.; Lanzini, A.; Tognana, L.; Silvestri, S.; Santarelli, M. Waste to Energy: Exploration of Biogas from Organic Waste in a 500 W_{el} Solid Oxide Fuel Cell (SOFC) Stack. *Energy* **2015**, *85*, 145-158.

(3-10) Tuyen, T. Q.; Kaida, T.; Sakamoto, M.; Sasaki, K.; Shiratori, Y. Effectiveness of Paper-Structured Catalyst for the Operation of Biodiesel-Fueled Solid Oxide Fuel Cell. *J. Power Sources* **2015**, *283*, 320-327.

(3-11) Mehr, A. S.; Mahmoudi, S. M. S.; Yari, M.; Chitsaz, A. Thermodynamic and Exergoeconomic Analysis of Biogas Fed Solid Oxide Fuel Cell Power Plants Emphasizing on Anode and Cathode Recycling: A Comparative Study. *Energy Convers. Manage.* **2015**, *105*, 596-606.

(3-12) Kirtley, J. D.; Pomfret, M. B.; Steinhurst D. A.; Owrutsky, J. C.; Walker, R. A. In Operando Optical Studies of SOFCs Operating with Butanol. *ECS Trans.* **2015**, *68*, 1091-1102.

(3-13) Slinn, M.; Kendall, K.; Mallon, C.; Andrews, J. Steam Reforming of Biodiesel By-Product to Make Renewable Hydrogen. *Bioresour. Technol.* **2008**, *99*, 5851-5858.

(3-14) Sengodan, S.; Choi, S.; Jun, A.; Shin, T. H.; Ju, H. Y.; Shin, J.; Irvine, J. T. S.; Kim, G. Layered Oxygen-Deficient Double Perovskite as an Efficient and Stable Anode for Direct Hydrocarbon Solid Oxide Fuel Cells. *Nat. Mater.* **2015**, *14*, 205-209.

(3-15) Yang, C.; Li, J.; Lin, Y.; Liu, J.; Chen, F.; Liu, M. In Situ Fabrication of CoFe Alloy Nanoparticles Structured $(Pr_{0.4}Sr_{0.6})_3(Fe_{0.85}Nb_{0.15})_2O_7$ Ceramic Anode for Direct Hydrocarbons Solid Oxide Fuel Cells. *Nano Energy* **2015**, *11*, 704-710.

(3-16) Aliotta, C.; Liotta, L. F.; Deganello, F.; La Parola, V.; Martorana, A. Direct Methane Oxidation on $La_{1-x}Sr_xCr_{1-y}Fe_yO_{3-\delta}$ Perovskite-Type Oxides as Potential Anode for Intermediate Temperature Solid Oxide Fuel Cells. *Appl. Catal. B* **2016**, *180*, 424-433.

(3-17) Farrell, B.; Linic, S. Direct Electrochemical Oxidation of Ethanol on SOFCs: Improved Carbon Tolerance of Ni Anode by Alloying. *Appl. Catal. B* **2016**, *183*, 386-393.

(3-18) Chick, L.; Weimar, M.; Whyatt, G.; Powell, M. The Case for Natural Gas Fueled Solid Oxide Fuel Cell Power Systems for Distributed Generation. *Fuel Cells* **2015**, *15*, 49-60.

(3-19) Cai, W.; Zhou, Q.; Xie, Y.; Liu, J. A Facile Method of Preparing Fe-Loaded Activated Carbon Fuel for Direct Carbon Solid Oxide Fuel Cells. *Fuel* **2015**, *159*, 887-893.

(3-20) Jiao, Y.; Tian, W.; Chen, H.; Shi, H.; Yang, B.; Li, C.; Shao, Z.; Zhu, Z.; Li, S. D. In Situ Catalyzed Boudouard Reaction of Coal Char for Solid Oxide-Based Carbon Fuel Cells with Improved Performance. *Appl. Energy* **2015**, *141*, 200-208.

(3-21) Danilovic, N.; Luo, J. L.; Chuang, K. T.; Sanger, A. R. Effect of Substitution with Cr^{3+} and Addition of Ni on the Physical and Electrochemical Properties of $Ce_{0.9}Sr_{0.1}VO_3$ as a H_2S-Active Anode for Solid Oxide Fuel Cells. *J. Power Sources* **2009**, *194*, 252-262.

(3-22) Roushanafshar, M.; Luo, J. L.; Vincent, A. L.; Chuang, K. T.; Sanger, A. R. Effect of Hydrogen Sulfide Inclusion in Syngas Feed on the Electrocatalytic Activity of LST-YDC Composite Anodes for High Temperature SOFC Applications. *Int. J. Hydrogen Energy* **2012**, *37*, 7762-7770.

(3-23) Hagen, A.; Rasmussen, J. F. B.; Thydén, K. Durability of Solid Oxide Fuel Cells Using Sulfur Containing Fuels. *J. Power Sources* **2011**, *196*, 7271-7276.

(3-24) Lohsoontorn, P.; Brett, D. J. L.; Brandon, N. P. Thermodynamic Predictions of the Impact of Fuel Composition on the Propensity of Sulphur to Interact with Ni and Ceria-Based Anodes for Solid Oxide Fuel Cells. *J. Power Sources* **2008**, *175*, 60-67.

(3-25) Zeng, Z. H.; Björketun, M. E.; Ebbesen, S.; Mogensen, M. B.; Rossmeisl, J. Origin of Electrolyte-Dopant Dependent Sulfur Poisoning of SOFC Anodes. *Phys. Chem. Chem. Phys.* **2013**, *15*, 6769-6772.

(3-26) Sasaki, K.; Haga, K.; Yoshizumi, T.; Minematsu, D.; Yuki, E.; Liu, R. R.; Uryu, C.; Oshima, T.; Ogura, T.; Shiratori, Y.; et al. Chemical Durability of Solid Oxide Fuel Cells: Influence of Impurities on Long-Term Performance. *J. Power Sources* **2011**, *196*, 9130-9140.

(3-27) Haga, K.; Adachi, S.; Shiratori, Y.; Ito, K.; Sasaki, K. Poisoning of SOFC Anodes by Various Fuel Impurities. *Solid State Ionics* **2008**, *179*, 1427-1431.

(3-28) Yoshizumi, T.; Taniguchi, S.; Shiratori, Y.; Sasaki, K. Sulfur Poisoning of SOFCs: Voltage Oscillation and Ni Oxidation. *J. Electrochem. Soc.* **2012**, *159*, F693-F701.

(3-29) Alfonso, D. R. First-Principles Studies of H_2S Adsorption and Dissociation on Metal Surfaces. *Surf. Sci.* **2008**, *602*, 2758-2768.

(3-30) Choi, Y. M.; Compson, C.; Lin, M. C.; Liu, M. Ab Initio Analysis of Sulfur Tolerance of Ni, Cu, and Ni-Cu Alloys for Solid Oxide Fuel Cells. *J. Alloys Compd.* **2007**, *427*, 25-29.

(3-31) Wang, J. H.; Liu, M. Computational Study of Sulfur-Nickel Interactions: A New S-Ni Phase Diagram. *Electrochem. Commun.* **2007**, *9*, 2212-2217.

(3-32) Galea, N. M.; Kadantsev E. U.; Ziegler, T. Studying Reduction in Solid Oxide Fuel Cell Activity with Density Functional Theory-Effects of Hydrogen Sulfide Adsorption on Nickel Anode Surface. *J. Phys. Chem. C* **2007**, *111*, 14457-14468.

(3-33) Ogura, T.; Ishimoto, T.; Koyama, M. Density Functional Theory Study of Sulfur Poisoning on Nickel Anode in Solid Oxide Fuel Cells: Effects of Surface and Subsurface Sulfur. *J. Chem. Eng. Jpn.* **2014**, *47*, 793-800.

(3-34) Monder, S. D.; Karan K. Ab Initio Adsorption Thermodynamics of H_2S and H_2 on Ni(111): The Importance of Thermal Corrections and Multiple Reaction Equilibria. *J. Phys. Chem. C* **2010**, *114*, 22597-22602.

(3-35) Abild-Pedersen, F.; Lytken, O.; Engbæk, J.; Nielsen, G.; Chorkendorff, I.; Nørskov, J. K. Methane Activation on Ni(111): Effects of Poisons and Step Defects. *Surf. Sci.* **2005**, *590*, 127-137.

(3-36) Malyi, O. I.; Chen, Z.; Kulish, V. V.; Bai, K.; Wu, P. Density Functional Theory Study of the Effects of Alloying Additions on Sulfur Adsorption on Nickel Surfaces. *Appl. Surf. Sci.* **2013**, *264*, 320-328.

(3-37) Gong, M.; Liu, X.; Trembly, J.; Johnson, C. Sulfur-Tolerant Anode Materials for Solid Oxide Fuel Cell Application. *J. Power Sources* **2007**, *168*, 289-298.

(3-38) Aguilar, L.; Zha, S.; Cheng, Z.; Winnick, J.; Liu, M. A Solid Oxide Fuel Cell Operating on Hydrogen Sulfide (H_2S) and Sulfur-Containing Fuels. *J. Power Sources* **2004**, *135*, 17-24.

(3-39) Vincent, A.; Luo, J. L.; Chuang, K. T.; Sanger, A. R. Effect of Ba Doping on Performance of LST as Anode in Solid Oxide Fuel Cells. *J. Power Sources* **2010**, *195*, 769-774.

(3-40) Li, J. H.; Fu, X. Z.; Luo, J. L.; Chuang, K. T.; Sanger, A. R. Application of $BaTiO_3$ as Anode Materials for H_2S-Containing CH_4 Fueled Solid Oxide Fuel Cells. *J. Power Sources* **2012**, *213*, 69-77.

(3-41) Staykov A.; Téllez H.; Akbay T.; Druce J.; Ishihara T.; Kilner J. Oxygen Activation and Dissociation on Transition Metal Free Perovskite Surfaces. *Chem. Mater.* **2015**, *27*, 8273-8281.

(3-42) Ishimoto, T.; Sato K.; Tada T.; Amezawa K.; Koyama M. Theoretical Study on Oxygen Dissociation Reaction on $LaSrCoO_3$. *ECS Trans.*, **2015**, *68*, 651-655.

(3-43) Han, J. W.; Yildiz, B. Mechanism for Enhanced Oxygen Reduction Kinetics at the $(La,Sr)CoO_{3-\delta}/(La,Sr)_2CoO_{4+\delta}$ Hetero-Interface. *Energy Environ. Sci.* **2012**, *5*, 8598-8607.

(3-44) Kresse, G.; Hafner, J. Ab Initio Molecular Dynamics for Liquid Metals. *Phys. Rev. B: Condens. Matter. Phys.* **1993**, *47*, 558-561.

(3-45) Kresse, G.; Furthmüller, J. Efficient Iterative Schemes for Ab Initio Total-Energy Calculations Using a Plane-Wave Basis Set. *Phys. Rev. B: Condens. Matter. Phys.* **1996**, *54*, 11169-11186.

(3-46) Kresse, G.; Furthmüller, J. Efficiency of Ab-Initio Total Energy Calculations for Metals and Semiconductors Using a Plane-Wave Basis Set. *Comput. Mater. Sci.* **1996**, *6*, 15-50.

(3-47) Blöchl, P. E. Projector Augmented-Wave Method. *Phys. Rev. B: Condens. Matter. Phys.* **1994**, *50*, 17953-17979.

(3-48) *Ferroelectrics and Related Substances;* Hellwege, K. H.; Hellwege A. M., Eds.; Landolt-Börnstein, New Series Vol. 3; Springer: Berlin, 1969.

(3-49) Tasker, P. W. The Stability of Ionic Crystal Surfaces. *J. Phys. C: Solid State Phys.* **1979**, *12*, 4977.

(3-50) Padilla, J.; Vanderbilt, D. Ab Initio Study of $BaTiO_3$ Surfaces. *Phys. Rev. B: Condens. Matter. Phys.* **1997**, *56*, 1625.

(3-51) Meyer, B.; Padilla, J.; Vanderbilt, D. Theory $PbTiO_3$, $BaTiO_3$, and $SrTiO_3$ Surfaces. *Faraday Discuss*. **1999**, *114*, 395-405.

(3-52) Kolpak, A. M.; Li, D.; Shao, R.; Rappe, A. M.; Bonnell, D. A. Evolution of the Structure and Thermodynamic Stability of the $BaTiO_3$(001) Surface. *Phys. Rev. Lett.* **2008**, *101*, 036102.

(3-53) Martirez, J. M. P.; Morales, E. H.; Saidi, W. A.; Bonnell, D. A.; Rappe, A. M. Atomic and Electronic Structure of the $BaTiO_3$(001) $(\sqrt{5}\times\sqrt{5})R26.6^\circ$ Surface Reconstruction. *Phys. Rev. Lett.* **2012**, *109*, 256802.

(3-54) Morales, E. H.; Bonnell, D. A. On the Relationship between Surface Reconstructions and Step Edge Stability on $BaTiO_3$(001). *Surf. Sci.* **2013**, *609*, 62-66.

(3-55) Morales, E. H.; Martirez, J. M. P.; Saidi, W. A.; Rappe, A. M.; Bonnell, D. A. Coexisting Surface Phases and Coherent One-Dimensional Interfaces on $BaTiO_3$(001). *ACS Nano* **2014**, *8*, 4465-4473.

(3-56) Rakotovelo, G.; Moussounda, P. S.; Haroun, M. F.; Légaré, P.; Rakotomahevitra, A.; Parlebas, J. C. DFT Study of $BaTiO_3$(001) Surface with O and O_2 Adsorption. *Eur. Phys. J. B* **2007**, *57*, 291-297.

(3-57) Zhukovskii, Y. F.; Kotomin, E. A.; Ellis, D. E. Comparative Ab Initio Study of Cu Overlayers on $BaTiO_3$(001) and MgO(001) Substrates. *Phys. Status Solidi B* **2008**, 24*5 (5)*, 980-985.

(3-58) Rakotovelo, G.; Moussounda, P. S.; Haroun, M. F.; Légaré, P.; Rakotomahevitra, A.; Rakotomalala, M.; Parlebas, J. C. Adsorption of CO, CO_2 and NO Molecules on a $BaTiO_3$(001) Surface. *Surf. Sci.* **2009**, *603*, 1221-1228.

(3-59) Geneste, G.; Dkhil, B. Adsorption and Dissociation of H_2O on In-Plane-Polarized $BaTiO_3$(001) Surfaces and their Relation to Ferroelectricity. *Phys. Rev. B: Condens. Matter. Phys.* **2009**, *79*, 235420.

(3-60) Berlich, A.; Strauss, H.; Langheinrich, C.; Chassé, A.; Morgner, H. Surface Termination of $BaTiO_3$(001) Single Crystals: A Combined Electron Spectroscopic and Theoretical Study. *Surf. Sci.* **2011**, *605*, 158-165.

(3-61) Nakayama, M.; Hotta, S.; Nakamura, T.; Kasuga, T. Morphology and Surface Structure of Cubic $BaTiO_3$ Using First-Principles Density Functional Theory. *J. Ceram. Soc. Jpn.* **2013**, *121*, 611-613.

(3-62) Noguera, C. *Physics and Chemistry at Oxide Surfaces*; Cambridge University Press: Cambridge, 1996.

(3-63) Sholl, D. S.; Steckel, J. A. *Density Functional Theory: A Practical Introduction*; John Wiley & Sons, Inc.: Hoboken, New Jersey, 2009.

(3-64) Goniakowski, J.; Finocchi, F.; Noguera, C. Polarity of Oxide Surfaces and Nanostructures. *Reports Prog. Phys.* **2008**, *71* (1), 016501.

(3-65) Moriwake, H. First-principles Calculation of Formation Energy of Neutral Point Defects in Perovskite-Type $BaTiO_3$. *Int. J. Quantum Chem.* **2004**, *99*, 824-827.

(3-66) Cao, D.; Cai, M. Q.; Hu, W. Y.; Yu, P.; Huang, H. T. Vacancy-Induced Magnetism in $BaTiO_3$(001) Thin Films Based on Density Functional Theory. *Phys. Chem. Chem. Phys.* **2011**, *13*, 4738-4747.

(3-67) Eror, N. G.; Smyth, D. M. Nonstoichiometric Disorder in Single-Crystalline $BaTiO_3$ at Elevated Temperatures. *J. Solid State Chem.* **1978**, *24*, 235-244.

(3-68) Chan, N. H.; Sharma, R. K.; Smyth D. M. Nonstoichiometry in Undoped $BaTiO_3$. *J. Am. Ceram. Soc.* **1981**, *64*, 556-562.

(3-69) Hui, S.; Petric, A. Evaluation of Yttrium-Doped $SrTiO_3$ as an Anode for Solid Oxide Fuel Cells. *J. Eur. Ceram. Soc.* **2002**, *22*, 1673-1681.

(3-70) Li, X.; Zhao, H.; Xu, N.; Zhou, X.; Zhang, C.; Chen, N. Electrical Conduction Behavior of La, Co, Co-Doped $SrTiO_3$ Perovskite as Anode Material for Solid Oxide Fuel Cells. *Int. J. Hydrogen Energy* **2009**, *34*, 6407-6414.

(3-71) Atkinson, A.; Barnett, S.; Gorte, R. J.; Irvine, J. T. S.; McEvoy, A. J.; Mogensen, M.; Singhal, S. C.; Vohs, J. Advanced Anodes for High-Temperature Fuel Fells. *Nat. Mater.* **2004**, *3*, 17-27.

(3-72) McIntosh, S.; Gorte, R. J. Direct Hydrocarbon Solid Oxide Fuel Cells. *Chem. Rev.* **2004**, *104*, 4845-4865.

(3-73) Heifets, E.; Kotomin, E. A.; Mastrikov, Y. A.; Piskunov, S.; Maier, J. In *Thermodynamics-Interaction Studies-Solids, Liquids and Gases*; Moreno P. J C., Ed; InTech: DOI: 10.5772/20114. Available from: http://www.intechopen.com/books/thermodynamics-interaction-studies-solids-liquids-and-gases/thermodynamics-of-abo3-type-perovskite-surfaces.

(3-74) Liu, S.; Muhammad, A.; Mihara, K.; Ishimoto, T.; Tada, T.; Koyama, M. Predictive Microkinetic Model for Solid Oxide Fuel Cell Patterned Anode: Based on an Extensive Literature Survey and Exhaustive Simulations. *J. Phys. Chem. C* **2017**, *121* (35), 19069–19079.

CHAPTER 4

Theoretical Study of SnO_2 as Support Material for Polymer Electrolyte Fuel Cell Electrocatalyst

4.1 INTRODUCTION

Polymer electrolyte fuel cells (PEFCs) have been broadly researched as technologies for the transportation sector, portable devices, and residential co-generation systems due to their environmental friendly operation, modularity and high efficient energy conversion.[1-6] However, some long-standing issues due to the high cost of platinum (Pt), unreliable performance and low durability are still a major impediment for large-scale commercialization.[1,2,4,5,7-10] Pt, while it exhibits the best electrocatalytic performance,[8,10] is a scarce and expensive element. Thus a great deal of researchers have focused on reducing the amount of Pt used.[4-8,10-15] Nowadays, Pt-nanoparticles are uniformly dispersed on carbon as support material to maximize the active surface area per unit mass of Pt, decrease the Pt-loading, and decreasing the cost.[6,8,10,14-17] Carbon blacks are the most commonly used supports for Pt and Pt based-alloys due to the high surface area, good electronic conductivity, and low cost.[8,10,16,18-21] Nevertheless, the activity of carbon blacks is affected by the presence of organo-sulfur impurities, and deep surface micro-pores.[21,22] Additionally, carbon blacks are unstable under the operating conditions experienced at the cathode side of PEFCs, i.e., relatively elevated temperature,[3,23] acidic conditions,[3,23] humidity,[3] and high potential.[3,6,23] Consequently, different carbon-based support materials have been extensively investigated as alternative supports for PEFC catalysts, such as single wall carbon nanotubes[24,25] and multiple wall carbon nanotubes that show excellent conductivity, and lower degradation rate compared to carbon black.[10,26] Graphene is another promising support material with high conductivity, fast electron transfer, and large surface area for catalyst nanoparticle attachment.[27-29] Also, tailored graphitic nanofibers led to greatly dispersed nanoparticles, which adopted specific crystallographic orientations that were more resistant to the CO poisoning,[30] in the same way carbon nanofibers led to controlled size and well-dispersed nanoparticles decoration.[31] Moreover, the morphology and structure of mesoporous carbons facilitated the diffusion of reactants to the active sites, removing byproducts, and enhancing dispersion of the metal nanoparticles.[32-34] Boron-doped diamond-like carbons have been shown to be relatively electrochemically stable under conditions of carbon corrosion.[35,36] Although, employing different carbon-based support materials improved the durability and the performance of the active layer, the complete suppression of carbon degradation has not yet been achieved.

Nanostructured metal oxides may be able to provide an alternative to carbon-based supports. Resistance towards corrosion, low cost, and wide availability of certain metal oxides increase their suitability for the replacement of carbon-based support materials.[37] Among them, SnO_2, an n-type semiconductor and amphoteric oxide that has been widely used in gas sensing devices,[38] transparent conducting electrodes,[39,40] complete oxidation of methane,[41,42] promoter for propane[43] and isobutene[44] dehydrogenation showed a large improvement in durability when used as support material for Pt-nanoparticles.[23,45] However, a mild degradation due to Ostwald ripening, and low activity attributed to the low conductivity of SnO_2 were observed.[23,46] Enhanced electrical conductivity of SnO_2 was obtained by the introduction of small percentages of dopant materials.[6,23,46-51] Higher electrical conductivity of the support was reported to lead to an improved activity for the oxygen reduction reaction (ORR).[23,46] On the other hand, Ta-,[50] and Sb-[3] doped SnO_2 possessed electrical conductivities more than 40 times higher than Nb-doped SnO_2, however the ORR activity of the Nb-doped SnO_2 was similar and higher to the Sb- and Ta-doped SnO_2, respectively. Hence, no definite correlation between the support conductivity and the ORR activity can be obtained. A recent study, using various dopants with different concentrations concluded that although doping SnO_2 directly affects the ORR activity, the ambiguity between support conductivity and ORR activity still holds.[52] Moreover, large Pt-loadings on oxidized SnO_2, reduced SnO_2 and graphene showed comparable ORR. While only for oxidized SnO_2, decreasing the amount of Pt led to lower ORR activities, which were attributed to stronger adsorption of oxygenated systems.[51] Although, these results show that there is a pronounced dependence of the electronic properties and the catalytic behavior of metal particles on the support material, a systematic study to understand the influence of SnO_2 on the physical, and electronic properties of Pt-nanoparticles is currently missing. Little information regarding the effect of SnO_2 on the properties of Pt-nanoparticles is available in theoretical studies. Previous density functional theory (DFT) calculations have explained the stronger interaction of the Pt/SnO_2 system compared to the Pt/graphene system by a larger variation of the Pt-Pt distance.[11]

Other DFT studies reported that the interaction of a Pt-nanoparticle consisting of 29 atoms was stronger on reduced SnO_2 compared with stoichiometric SnO_2,[53] and that the presence of Sb on the reduced SnO_2 surface led to an even stronger interaction.[54] Similarly, hydrogen atom diffusion in a Pt_{29}/SnO_2 system was shown to be promoted as the H-atom approached the support.[55] After two hydrogen atoms were adsorbed onto SnO_2, spontaneous O_2 adsorption on the Pt-nanoparticle was achieved, and the most stable H_2O formation occurred near the metal-support interface.[56]

Predicting the performance of a catalyst based on theoretical models will lead to engineer materials with specific catalytic functions and increased resistance towards degradation. The strong interaction between the catalyst and adsorbate has sometimes been used to describe the reactivity of metal/metal oxide surfaces.[57,58] Thus, it is important to elucidate the variables that can suitably describe the energetics of the adsorbent-adsorbate interaction. In recent years DFT method has been recognized as useful in understanding the adsorbate-adsorbent interaction. Hammer-Nørskov model[59] linearly scales the *d*-band center and the adsorption energy. This model showed moderate linear correlations between the heats of adsorption of small molecules or atoms such as CO, H_2, O_2, and C_xH_y on various metal surfaces.[60] Also, a close linear relationship was also found for the H_2, CO, and OH adsorption energies and the *d*-band centers of Pt-atom supported on strained graphene.[61] The O-atom binding energy on a Rh-surface showed better correlation with the *d*-band center than when the O-atom was adsorbed on a Ag-surface.[62] Large deviations were observed between the adsorption energies and *d*-band centers for the CO and O-atom adsorbed on Au-surfaces and Au_{12} nanoparticles.[63] Electrochemical changes in the hydrogen adsorption energy on Pd-overlayers on different metals scaled linearly with the changes in the *d*-band center due to changes in the interatomic distances.[64] The CO, and O-atom binding energies on different metal surfaces showed a close linear fit with the surfaces' *d*-band centers.[65] The binding energy of an O-atom on Pt-surfaces and Pt-alloys surfaces and the materials *d*-band centers showed a modest fit.[66] However, the reported relationship do not account for less coordinated atoms such as vertices and edges of nanoparticles and their effect on the adsorption, especially for small enough nanoparticles that do not expose well-defined planes.[57,67,68] In the same way, the O-atom and OH adsorption on 1 and 2 nm Pt-nanoparticles revealed that there is not a unique relation between the shift of the *d*-band centers and the chemisorption energies.[57] Hence the *d*-band center would not be a sole descriptive variable when change in particle size and coordination occurs.[57] Likewise, the O-atom, O_2, OOH, H_2O, and H_2O_2 adsorption on a number of truncated octahedral Pt-nanoparticles with diameters between 0.7 and 1.7 nm revealed that the *d*-band center model is not suitable on nanometer-size systems, where their proposed generalized coordination number can be more appropriated.[69] Similarly, a quadratic model was used to approximate the CO adsorption on Au-nanoparticles that was estimated by the changes in the coordination number and the curvature.[68] However, in order to reduce computational cost atomic re-arrangement and changes in the symmetry due to the CO-Au interaction were not consider. In the same way, the CO adsorption on Pt-nanoparticles ranging from 0.2-1.5 nm in diameter was correlated with a number of descriptors.[70] Among them, a new descriptor, which partially incorporates some of the features of the CO-Pt bond formation was obtained from the CO adsorption on the Pt-nanoparticles where their coordinates were kept frozen.[70] Such additional descriptor involves an extra DFT calculation, which for larger systems is prohibitively computationally expensive. Additionally, the adsorption of CO was limited to the top sites of the Pt-nanoparticles.[70] Therefore, based on these examples from literature, simple and robust models with sound physical-chemical foundations and a reasonable transferability to more complex systems, and that do not require additional computational calculations to be estimated are missing. Complex systems exist at the PEFCs, where the effect of the size, shape, composition of the nanoparticle, the effect of the support, etc. should be taken into consideration. It is understandable that due to the complexity of these systems, it is difficult to obtain direct information on the structural or electronic properties. First-principles computational modeling methods can help providing insight into the atomic structure, morphology, electronic properties, etc., hence would provide valuable information on parameters that are crucial in catalyst design. For the reasons mentioned, in this work, a suitable multi-descriptor model for the O-atom binding energies considering the correlation with changing the Pt-nanoparticle size, and the adsorption site was proposed. Detailed analysis of the physical-chemical properties of Pt-nanoparticles was conducted in order to describe the O-adsorption energy as function on six different variables. Additionally, the DFT calculations were also conducted to understand the local behavior of the physical and electronic properties of Pt-nanoparticles supported on SnO_2 and use this information to predict the binding energy of an O-atom on the supported Pt-nanoparticles taking also into consideration the different adsorption sites.

4.2 COMPUTATIONAL PROCEDURE

All calculations performed in this chapter were based on the plane wave DFT method implemented in the Vienna Ab initio Simulation Package (VASP 5.3.5).[71-73]

Perdew−Burke−Ernzerhof parametrization of the generalized gradient approximation (GGA-PBE) was employed as exchange-correlation functional together with the projector augmented wave (PAW) method.[74] Spin-polarized calculations were performed throughout the study with a plane wave energy cutoff of 400 eV. The convergence criteria for all calculations were set until the difference in total energy between two ionic steps was less than 10^{-4} eV/atom, and 10^{-5} eV/atom for the band structure energy. The optimization of the face-centered cubic phase of Pt-bulk, and the rutile-type structure of SnO_2 was performed with 16 × 16 × 16, and 8 × 8 × 12 Monkhorst-Pack k-point mesh, respectively for the Brillouin zone integration where all the atoms and the crystal volume were allowed to relax. After the optimization, the calculated lattice parameter of Pt-bulk (a = 3.966 Å) and SnO_2 (a, b = 4.763 Å, and c = 3.222 Å) are in good agreement with the experimental value (a = 3.916 Å),[75] and (a, b = 4.737 Å, and c = 3.186 Å),[76] respectively. Isolated Pt-nanoparticles (Pt_n, where n = 4, 13, 55, 201, 405, 711, 807, or 2406 atoms, and correspond to sizes of 0.26, 0.53, 1.07, 1.70, 2.23, 2.78, 2.92, and 4.33 nm, respectively) were modeled and optimized until reaching convergence. To avoid the interaction between periodic images, 12 Å were set as the minimum distance between the boundaries of the cell and the Pt-atoms. After the optimization, Pt_4, Pt_{13}, and half-spherical clusters of Pt_{37}, Pt_{119}, and Pt_{233} that were truncated from Pt_{55}, Pt_{201}, and Pt_{405}, respectively were set to interact with their (111) planes parallel to those of SnO_2(110), as it was observed experimentally.[6] Two-layered oxygen-terminated SnO_2(110) (a single layer consists of top O, middle SnO, and bottom-O planes) was used as support for Pt_4, Pt_{13}, Pt_{37}, Pt_{119}, and Pt_{233} nanoparticles. The models employed in the calculations are shown in Figure 4-1. For the Pt_n/SnO_2 systems, a minimum distance of 15 Å was set between the boundaries of the cell and the Pt-atoms. The optimization of the isolated Pt_n and Pt_n/SnO_2 was performed at Γ point in the reciprocal space, due to significant spatial extent of the systems, where all Pt-atoms and the atoms of the top layer of SnO_2 were relaxed. To corroborate the difference in stability of Pt-nanoparticles on SnO_2 and directly compare the effect of graphene as support material, Pt-atom, Pt_4, Pt_{13}, and Pt_{37} nanoparticles supported on graphene were modeled and optimized with the same settings as the Pt-nanoparticles on SnO_2.

The cohesive energies of isolated Pt_n, E_{coh}, the adsorption energies, E_{ads}, and formation energies, E_{form}, of Pt-clusters supported were defined as:

$$E_{coh} = E_{Pt_n} - nE_{Pt} \tag{4-1}$$

$$E_{ads} = E_{Pt_n/Support} - (E_{Support} + E_{Pt_n}) \tag{4-2}$$

$$E_{form} = E_{Pt_n/Support} - (E_{Support} + nE_{Pt}) \tag{4-3}$$

where n is the number of atoms in the nanoparticle, E_{Pt} is the energy of a single Pt-atom, $E_{Pt_n}$is the energy of the Pt-nanoparticle (the energy of Pt_{37}, Pt_{119}, and Pt_{233} were obtained by a self-consistent field calculation after the corresponding Pt-nanoparticles were optimized and cleaved in the (111) direction), $E_{Support}$ is the energy of the SnO_2 or graphene slabs, and $E_{Pt_n/Support}$ is the energy of the Pt-nanoparticle interacting with SnO_2 or graphene.

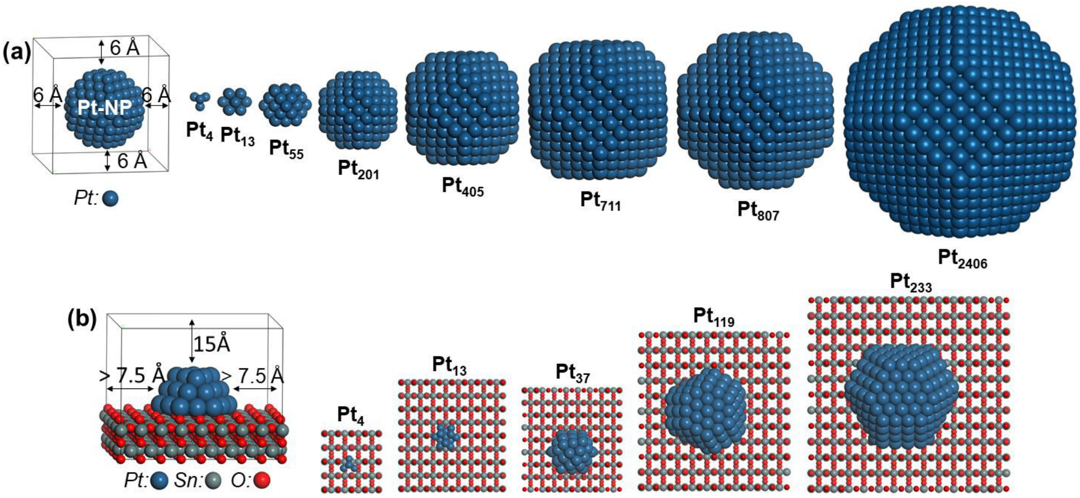

Figure 4-1. Models employed in the calculations: (a) isolated, and (b) supported Pt-nanoparticles.

The O-binding energy on the isolated Pt-nanoparticles, E_{bin}, and on the supported ones, $E_{bin-support}$, were defined as:

$$E_{bin} = E_{Pt_n-O} - (E_O + E_{Pt_n}) \tag{4-4}$$

$$E_{bin-support} = E_{Pt_n/Support-O} - (E_O + E_{Pt_n/Support}) \tag{4-5}$$

where E_{Pt_n-O}, $E_{Pt_n/Support-O}$ are the energies of an oxygen atom interacting with an isolated and supported Pt-nanoparticle, respectively and E_O is the energy of an isolated O-atom. For all the calculated energies, negative values indicate stability.

4.3 RESULTS AND DISCUSSION

4.3.1 Isolated Pt-nanoparticles.

4.3.1.1 Geometrical features. In this section, the structural aspects of the isolated Pt-nanoparticles and their dependences on the nanoparticle size are described. Figure 4-2a shows the ratio of surface sites at the outer-shell atoms in the isolated Pt-nanoparticles. The entire outer-shell atoms of Pt_4 and Pt_{13} are located at the nanoparticles' vertices, and as the size of the nanoparticle increases the number of atoms at the vertices decreases.

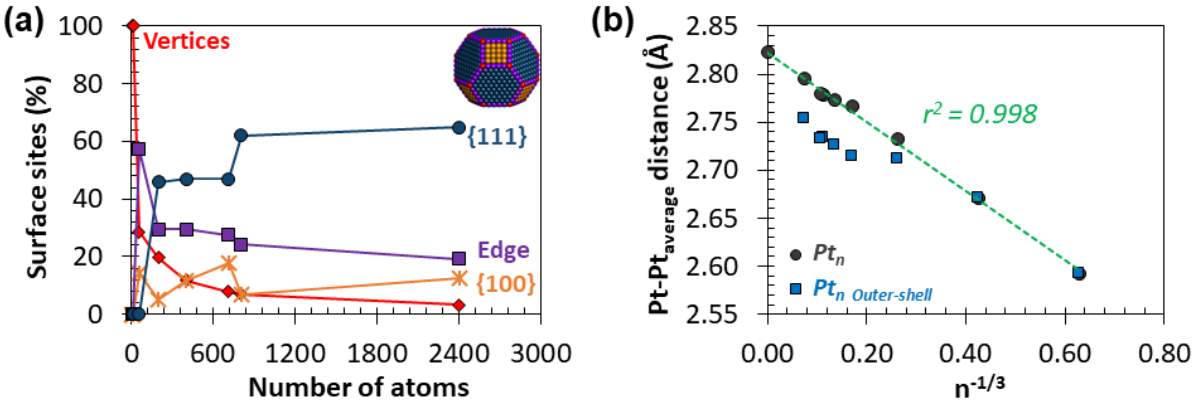

Figure 4-2. Size dependence of the isolated Pt_n geometrical features: (a) percentage of surface sites: vertices (red diamonds), edge (purple squares), {100} (orange stars), and {111} atoms (blue circles) and (b) average Pt-Pt distances of the nanoparticle (gray circles), and the nanoparticle's outer-shell atoms (blue squares). The linear regression line (dashed green) and the coefficient of determination are also shown.

Similarly, from Pt_{55} to Pt_{2406} the percentage of edge atoms also decreases with increasing the size of the nanoparticle. The {110} sites exhibited an unclear size dependency; the fraction of {110} sites in increasing order is $Pt_{201} < Pt_{807} < Pt_{405} < Pt_{2406} < Pt_{711}$. Increasing the size of the nanoparticle led to an increase in the fraction of {111} sites, which becomes predominant in Pt_{201} or larger. Atoms at edges and vertices are of higher energy (more reactive) as they are chemically unsaturated with a lower coordination number. The number of atoms with coordination numbers of 5, 6 and 7 decreases with increasing the nanoparticle size, while the number of atoms with coordination number of 12 increases. The size dependence of the average interatomic Pt-Pt distance is shown in Figure 2b. The average Pt-Pt distance was studied as a function of the nanoparticle size, which was approximated by $n^{-1/3}$ that showed to be proportional to the effective radius of the nanoparticle and to its surface to volume ratio.[77-80]

The nanoparticles' interatomic distance increased linearly with increasing the nanoparticle size and it was linearly scaled to a Pt-bulk value of 2.823 Å, which is in good agreement with the calculated value of 2.805 Å, and with the experimental value of 2.775 Å.[81] The overestimated value of the predicted interatomic Pt-Pt bulk distance (0.048 Å) compared to the experimental value was expected and agreed well with a previous work on scaling the properties of palladium nanoparticles where an overestimation of 0.04 to 0.10 Å was observed from employing the GGA functionals.[77] Similar scalability tendencies have been observed in palladium,[78,79] copper, gold, and silver nanoparticles.[80] Scalability is an interesting attribute for applications in nanoscience, photonics, catalysis, etc., as it allows the prediction and control of size-intrinsic properties.[78] However, it should be noted that the change in the ratio of outer-shell atoms and inner atoms also varied as the size of the nanoparticle increased while the average values of the Pt-Pt interatomic distance were discussed in the above analysis. These deviations in the interatomic distances are largely determined by decreasing the surface to volume ratio and grew with decreasing the size of the nanoparticle as shown in Figure 4-2b.

Another size-dependent property is the cohesive energy of the nanoparticle. The cohesive energy, which is the heat of sublimation, equals to the energy to divide the metal nanoparticle into isolated atoms.[78,82,83] The cohesive energy also showed a linear scale relation with $n^{-1/3}$, and it was gradually strengthening towards the corresponding energy in the bulk with increasing the particle size, as shown in Figure 4-3.

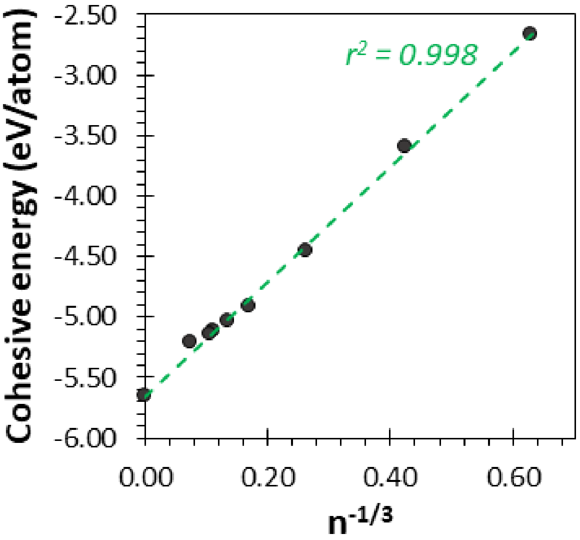

Figure 4-3. Size dependence of the isolated Pt-nanoparticles' cohesive energy (gray circles). The linear regression line (dashed green line) and the coefficient of determination are also shown.

The extrapolated Pt-bulk value of the cohesive energy was -5.66 eV/atom, which is in agreement with the calculated one by using a bulk model consisting of 4 atoms, -5.49

eV/atom, as well as the experimental value of -5.84 eV/atom.[84] The underestimation of the cohesive energy with respect to the experimental Pt-bulk value was attributed to the GGA functionals, as similar behavior was observed for the approximation of the cohesive energy on palladium[78] and ruthenium[85] nanoparticles. It should be noted that the value of the cohesive energy includes all atoms and different stabilities should be expected for the atoms at the outer-shell of each nanoparticle depending on their degree of coordination. As chemically unsaturated atoms with a lower coordination number are more prone to dissolution and bond weakening induced by adsorbates than highly coordinated atoms.[2,12,86]

4.3.1.2 Electronic properties. The electronic structure analysis of the isolated platinum nanoparticles is presented based on the density of states (DOS) profiles, as shown in Figure 4-4. This analysis can provide relevant information regarding the catalytic activity, as possible changes and other peculiarities in the DOS profiles will lead to different reactivity of the nanoparticles. Figure 4a shows the size dependence of the DOS. As the size of the Pt-nanoparticles becomes smaller, a decrease in confinement dimensions made the energy levels discrete. This decrease of the overlapping energy levels increases the energy separation between adjacent levels. The energy level-spacings are large for Pt_4 and Pt_{13} indicating their molecular character. Increasing the number of atoms in the nanoparticle, a continuous DOS emerges as the size increases due to overlapping of orbitals, as in the cases of Pt_{55} or larger nanoparticles. The same behavior was also reported for copper, silver, gold,[84] and Pt-nanoparticles.[87] In addition, as the Pt nanoparticles get bigger, their DOS profiles start to converge, as shown in the DOS difference (Figure 4a). Because the interaction of adsorbates is directly on the outer-shell atoms, the DOS profiles of only the outer-shell atoms are also shown in Figure 4b. For smaller nanoparticles, the DOS profiles are similar for both the whole nanoparticle and the outer-shell atoms, due to the large surface-to-volume ratio. As the size increases, the DOS profile of the outer-shell starts to resemble that of Pt(111), correlating well with the dominance of {111} sites for the largest nanoparticles, as shown in Figure 2a. The DOS profiles at the valence band of the outer-shell atoms became narrower than the ones for the whole nanoparticle as the particle size increased. This narrowing of the valence band led to an increment in the DOS peaks to maintain the same DOS area. A narrower valence band for transition metals signifies a *d*-band center closer to the Fermi level, which was reported to affect the adsorption properties of the nanoparticle.[51,88,89]

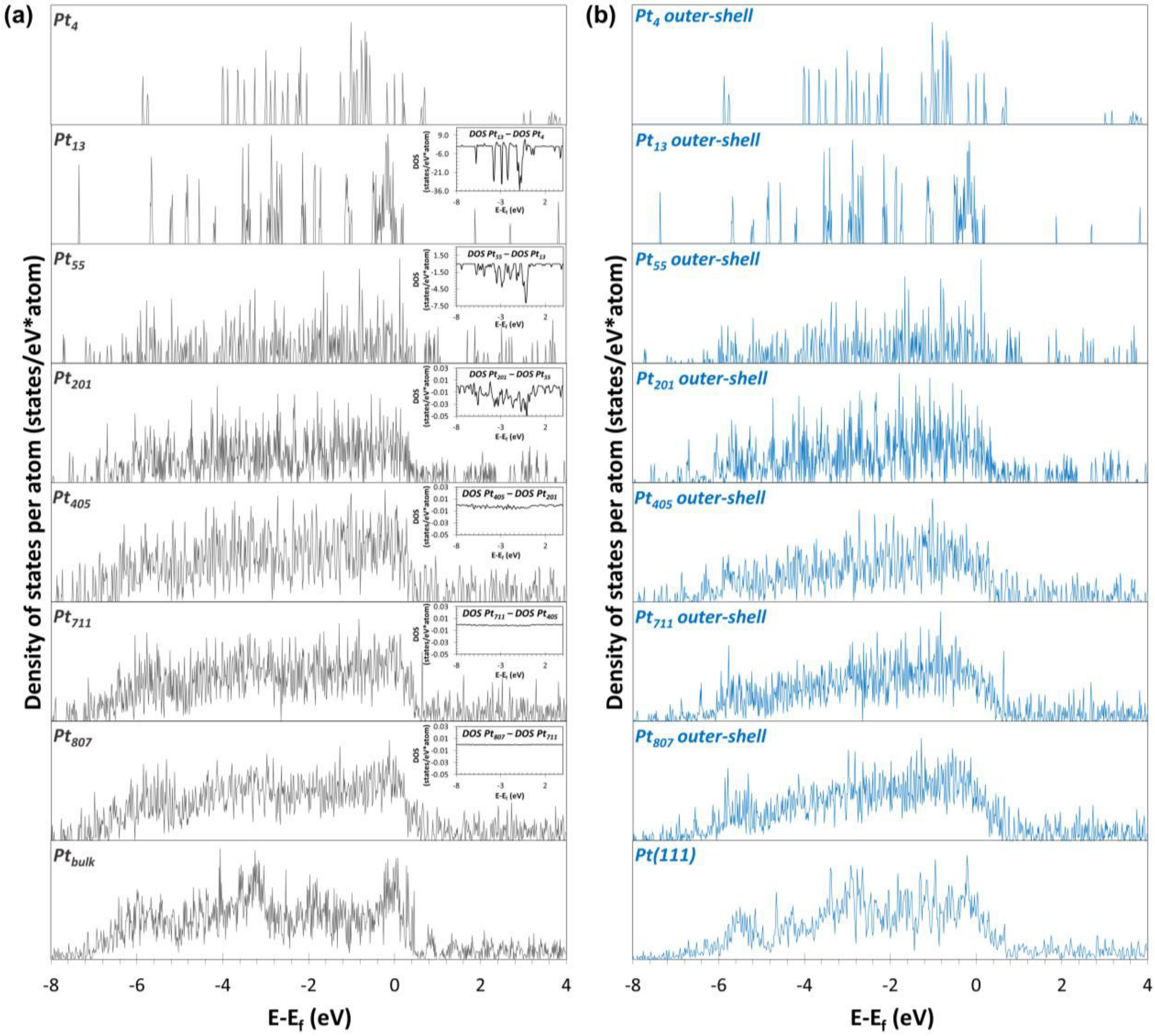

Figure 4-4. Electronic properties of isolated Pt-nanoparticles: (a) DOS profiles of the Pt-nanoparticles, the DOS difference between contiguous nanoparticles is also shown. (b) DOS profiles of the outer-shell atoms of the Pt-nanoparticles.

In Hammer-Nørskov model, the adsorption energy correlates with the position of the *d*-band center relative to the Fermi level. A downshift of the *d*-states relative to the Fermi level decreases the binding energies as the antibonding states become filled. Figure 4-5 shows the *d*-band center relative to the Fermi level for the isolated platinum nanoparticles. It is clear that the *d*-band centers of the nanoparticles and their outer-shell atoms downshifted with increasing the nanoparticle size. The *d*-band centers of the outer-shell atoms approached the value of the Pt(111) with increasing the nanoparticle size. Only Pt_{201} and Pt_{405} showed a downshifted *d*-band center value compared to Pt(111), hence following Hammer-Nørskov model the adsorbates interaction on those nanoparticles will be less stable.

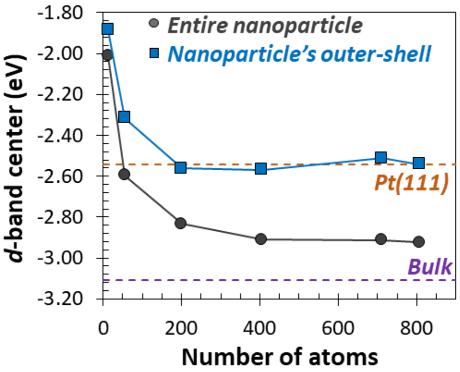

Figure 4-5. Size dependence of the Pt-nanoparticles' (gray circles) and the nanoparticles' outer-shell atoms' *d*-band centers (blue squares). The values of the Pt-bulk (dashed purple line) and Pt(111) (dashed orange line) *d*-band centers are shown as reference.

4.3.1.3 Chemical properties. In heterogeneous catalysis, the reacting species adsorb on the catalytic active solid surface. Chemical bonds are broken and formed on the surface and eventually the products are released back into the gas or liquid phase. The description of the chemical bond between a surface and an adsorbate is fundamental for understanding the surface chemical reactivity. At the cathode environment of a PEFC, O_2 activation typically involves a proton and electron transfer to form adsorbed OOH before the O-O bond is broken.[90] Hence, the catalyst must be able to stabilize OOH moderately, so after its dissociation into O-atom and OH, the catalyst surface must not bind these species too strongly else the desorption of H_2O will not be fast. In previous works[90,57,77] it was stated that if a surface can adsorb O-atom 0.0 to 0.4 eV more weakly than Pt(111), then the ORR activity will be better than Pt. The O-atom adsorption energy has been used as a descriptor of the catalytic activity.[77,90] In this section the size and adsorption site dependence of the O-atom binding on Pt_{13}, Pt_{55}, Pt_{201}, and Pt_{405} was analyzed. In Figure 4-6 the adsorption site and O-atom binding energy are shown. For the extended Pt(111) surface, the preferred adsorption site of an O-atom is on high symmetric sites such as FCC and HCP. The O-atom chemisorption on top sites is weaker than FCC and HCP sites, and on bridge sites, a local minimum was not found for the adsorption of O-atom, thus the atom moved to the FCC sites after optimization. On the other hand, the O-atom adsorption is preferred on the bridge sites of the Pt-nanoparticles, except for Pt_{13}, which changed towards a more stable symmetry after an O-atom was adsorbed on its top site. The adsorption on HCP sites of Pt_{55} is more stable than on FCC sites, which is due to that one of the three Pt-atoms at the HCP site is located at a vertex, leaving it under coordinated compared to atoms in the FCC site and enhancing its binding energy with the O-atom.

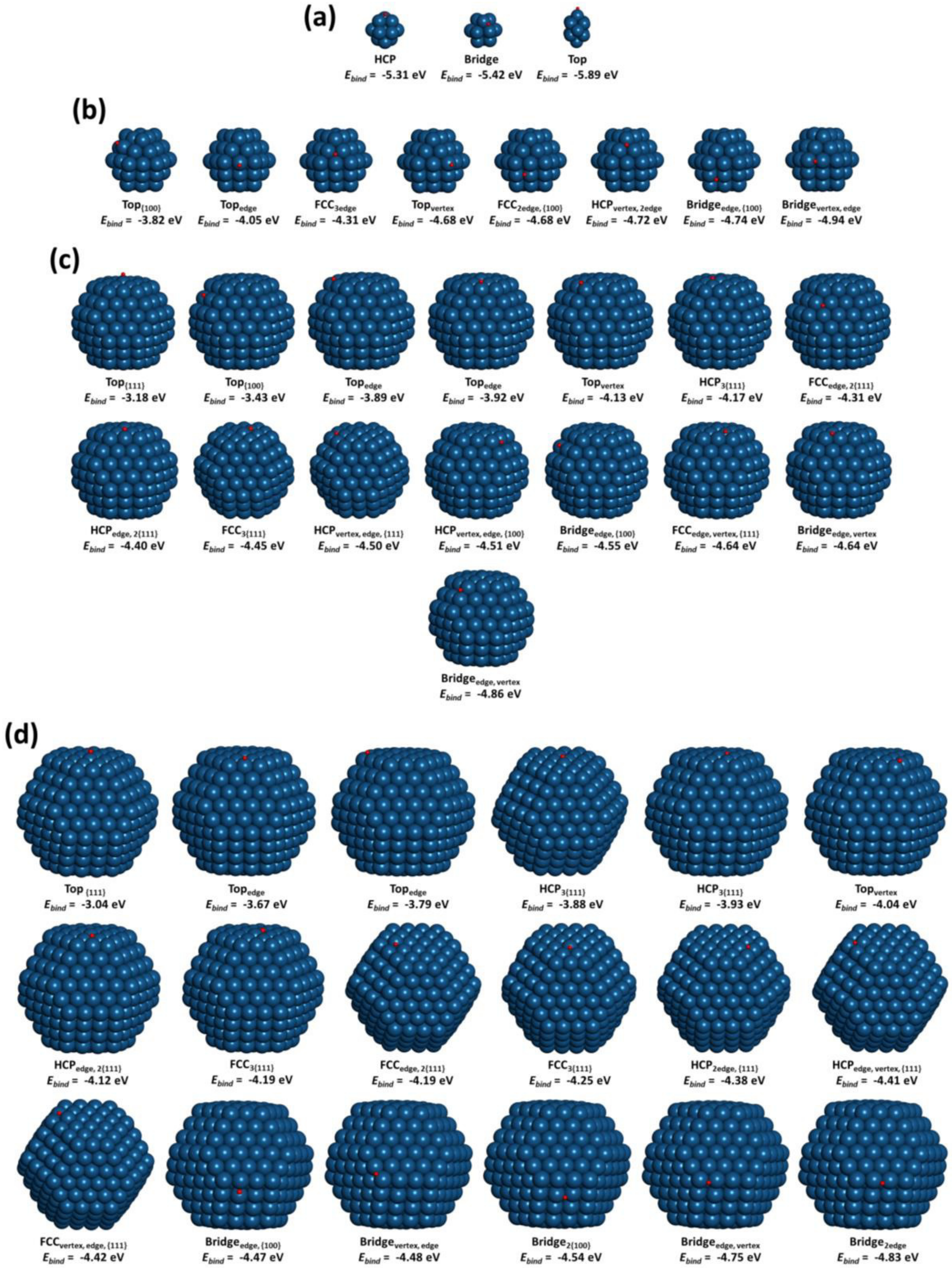

Figure 4-6. O-atom adsorption sites: (a) on Pt_{13}, (b) on Pt_{55}, (c) on Pt_{201}, and (d) on Pt_{405}. The values of the binding energy are also shown.

In the same way for the remaining nanoparticles, a more stable O-adsorption was observed as the Pt-atoms involved in the adsorption become less coordinated by other Pt-atoms. In Figure 4-7 can be seen that the stability of the O-atom adsorption lowers with increasing the size of the Pt-nanoparticles. It is difficult to single out the size effect from the adsorption site effect, however for O-atom adsorption at the nanoparticles' vertices, the binding energy increased 0.55 eV from Pt_{55} to Pt_{201}, and 0.09 eV from Pt_{201} to Pt_{405}. The O-atom binding energy on the top of a center atom of the {111} facet increased from -3.18 eV for Pt_{201} to -3.04 eV for Pt_{405}, which are 0.08 and 0.22 eV less stable than the O-atom binding energy on the top site of Pt(111), respectively. The binding energy on the FCC sites of the {111} surface of Pt_{201} and Pt_{405} are 0.11 and 0.37 eV less stable than on the FCC sites of Pt(111), respectively. The HCP sites of the {111} facet of Pt_{405} binds O-atom 0.22 to 0.27 eV less stable than on the HCP sites of Pt(111). Considering the statement of weaker O-binding energies than on Pt(111) will lead to an increased ORR activity,[90,91] the weaker stability of the O-atom binding on the {111} facet of Pt_{405} is less than 0.40 eV compared to Pt(111). Thus controlling the size of the Pt-nanoparticles close to 2.23 nm, which is the diameter of Pt_{405} could lead to an enhancement on the ORR activity. Previous experimental results[91] showed that the Pt-mass activity increased with growth of the particles, exhibiting a maximum activity at 2.20 nm. It should be noted that although there is a good agreement between the results in this work and the previously mentioned experimental results,[91] the operating conditions, the effect of support, different symmetry of the Pt-nanoparticles, etc., were not taken into consideration in this work.

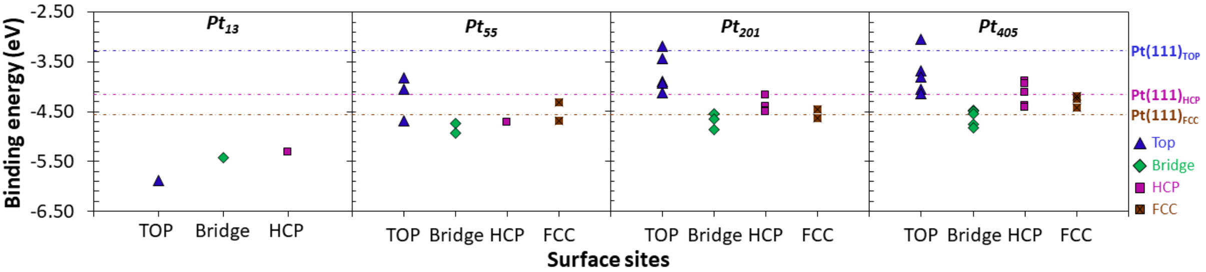

Figure 4-7. O-atom biding energies. Blue triangles, green diamonds, pink squares, and "X" filled brown squares indicate top, bridge, HCP, and FCC adsorption sites, respectively. The O-atom binding energies on the Pt(111) sites are shown as reference.

4.3.2 Effect of SnO_2 as support material. In this section, the influence of $SnO_2(110)$ on the geometrical features and electronic properties is discussed.

4.3.2.1 Effect of SnO_2 on the nanoparticles' geometrical features. Figure 4-8a shows the frequency distribution of the Pt-Pt interatomic distances of the isolated Pt-nanoparticles and Pt-nanoparticles supported on SnO_2. From the frequency distribution, nanoparticles consisting of 4, 13, and 37 atoms supported on SnO_2 exhibit significant changes in Pt-Pt distance compared to larger nanoparticles; Pt_{119} and Pt_{233} supported on SnO_2.

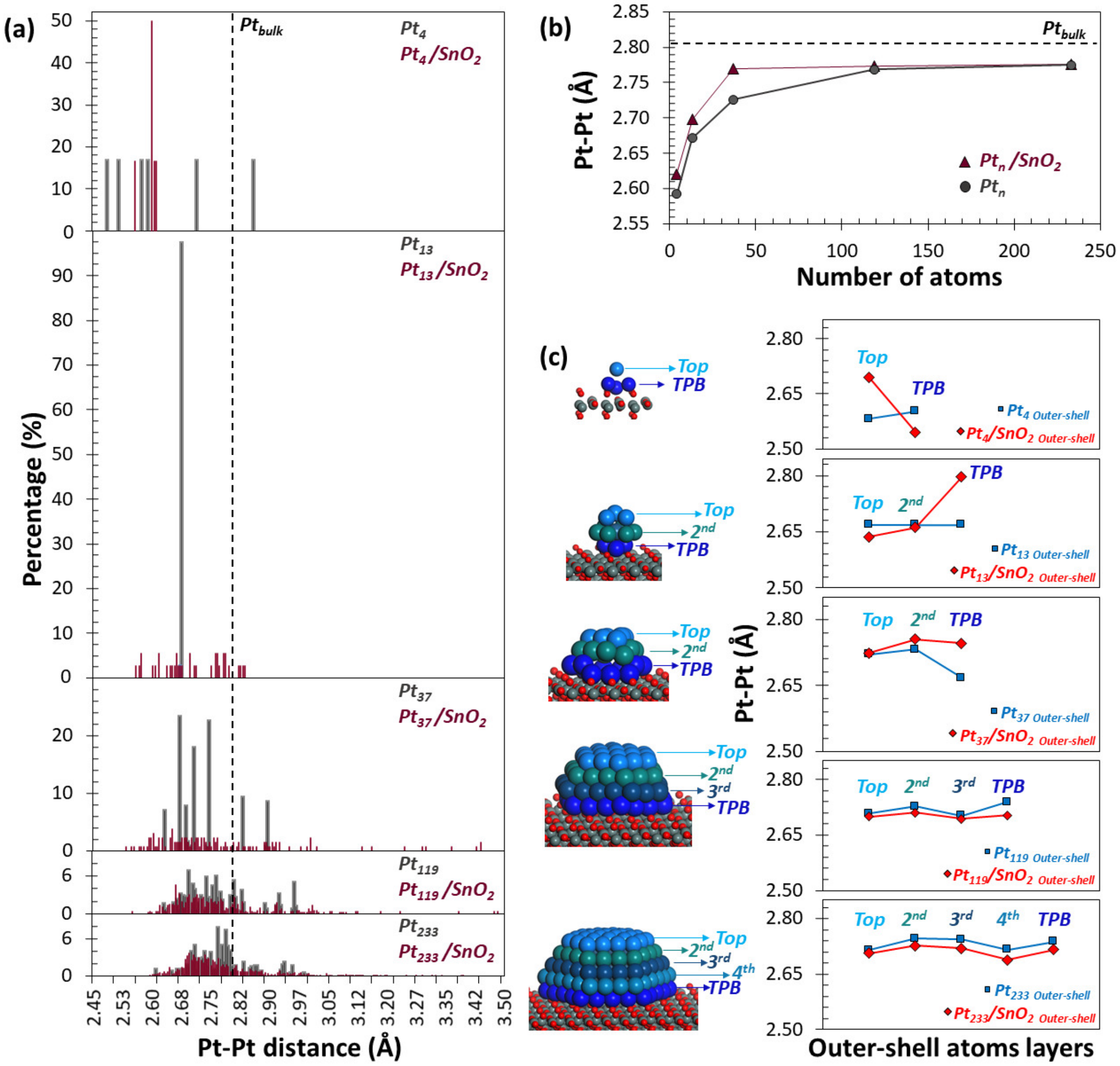

Figure 4-8. Effect of SnO_2 on the Pt-Pt distance: (a) frequency distribution of the Pt-Pt distance of the isolated (gray bars) and supported (dark red bars) Pt-nanoparticles, (b) size dependence of the Pt-Pt distance of isolated Pt-nanoparticles (gray circles) and supported Pt-nanoparticles (dark red triangles), and (c) variation in the Pt-Pt distance of the outer-shell atoms of isolated (blue squares) and supported (red diamonds) Pt-nanoparticles.

The average interatomic Pt-Pt distance was plotted against the size of the nanoparticle in Figure 4-8b. The interaction of the Pt-nanoparticles with SnO_2 lead to a rise in the Pt-Pt distance compared to the isolated nanoparticles. As the size of the nanoparticle increases the difference in the Pt-Pt distance due to the interaction with the support decreased, showing that the support effect will dissipate with increasing the size of the nanoparticle. The largest elongation of the interatomic distance was 0.044 Å observed for Pt_{37}/SnO_2, which also exhibited the largest atomic rearrangement.

Moreover, the variations in the interparticle distance due to the interaction with SnO_2 were also analyzed for the outer-shell atoms of the supported nanoparticles. Figure 4-8c shows the average interatomic Pt-Pt distances from the top facet to the Pt/SnO_2 interface. The largest variations were observed for the atoms located at the triple phase boundary (TPB). As the size of the nanoparticle increases the average interatomic distance for the atoms at the interface decreased, except for Pt_4, ranging from an expanded Pt-Pt distance of 2.800 Å for the interface atoms of Pt_{13}/SnO_2, to a compressed Pt-Pt distance of 2.725 Å for the interface atoms of Pt_{233}/SnO_2. Moreover, for the atoms at the top facets, variations in the interatomic distances became smaller, except for Pt_4, compared to the interface atoms, especially for the larger nanoparticles. The exception of Pt_4 can be explained regarding its small size and the lack of a core atom that behaves as a bulk-like atom. Showing that the support effect weakens with increasing the size of the supported nanoparticle and that the support effect is localized at the metal/support interface. Similar but stronger localization of the Pt-Pt distance at the interface was observed for platinum nanoparticles supported on graphene, where for all the Pt-nanoparticles an elongation of the Pt-Pt interatomic distance was observed.[15] On the contrary, the Pt-Pt interatomic distance changed from an elongation for Pt_{13} and Pt_{33} supported on SnO_2 to a shortening of the interatomic distances of the supported Pt_{119} and Pt_{233}. It should be noted that in the preceding study[15] spherical cuboctahedral Pt-nanoparticles were optimized on graphene.

4.3.2.2 Effect of SnO_2 on the nanoparticles' electronic properties. The contact between the Pt-nanoparticles and SnO_2 led to electron transfer from the nanoparticles to the support ranging from 0.76 electrons for Pt_4 to 4.10 electrons for Pt_{233}, leading to average charges of 0.19 e^-/atom to 0.02 e^-/atom, respectively. From Pt_{13}/SnO_2 to Pt_{233}/SnO_2 the outer-shell atoms are more oxidized than the corresponding atoms at the isolated nanoparticles, which can lead to a larger interaction with nucleophilic species such as O^{2-}, OH^-, H_2O, and H_2O_2 that are found at the cathode environment of the PEFC. It was reported that the electrocatalyst after forming OOH on its surface should have enough catalytic activity for the O-O bond dissociation, and it should be noble enough to bind moderately O-atom and OH after the dissociation else the desorption of H_2O will not be fast.[92] Hence, a larger interaction with nucleophilic species will result in blocking of the catalyst active sites slowing the kinetics of the reaction. Experimental results revealed that different Pt-loads supported on oxidized SnO_2 exhibited such a strong interaction with oxygenated species, which led to lower ORR activities for low Pt-loadings.[51] The electron density redistribution was mostly localized at the nanoparticle-support junction. The number of transferred electrons decreased with increasing the number of atoms at the Pt-SnO_2 interface. On the other hand, the atoms at the top facet of the supported nanoparticle evidenced smaller changes in their charge compared to the corresponding atoms at the isolated nanoparticles, as shown in Figure 4-9.

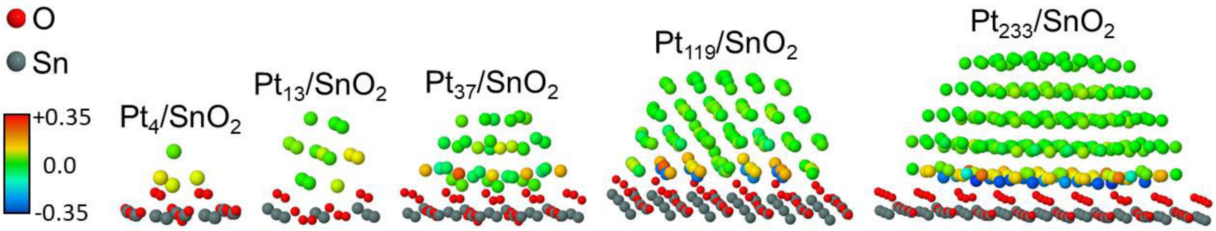

Figure 4-9. Color coding of the Pt-atoms charge.

The changes in the atomic charge for the top facet atoms is also size dependent and fades away with increasing the nanoparticle size. Variations in the *d*-band centers of the supported nanoparticles arising from the interaction with SnO_2 followed the same trend as the redistribution of the valence electrons and are shown in Figure 4-10. Because the interaction of the Pt-nanoparticles with gaseous species and adsorbates will be directly on the outer-shell atoms, in this study, only the *d*-band centers of the outer-shell atoms were analyzed.

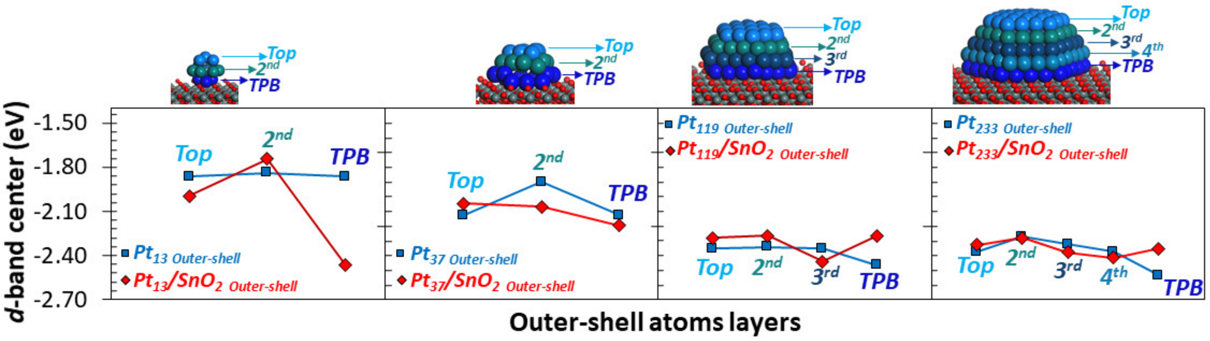

Figure 4-10. Effect of SnO_2 on the *d*-band centers of the outer-shell atoms of isolated (blue squares) and supported (red diamonds) Pt-nanoparticles.

Similarly to the charge distribution analysis and to the changes in the interatomic Pt-Pt distance, larger changes were observed at the TPB atoms. The *d*-band center of Pt_{13}/SnO_2 experienced a downshift of 0.60 eV and the downshifted value decreased to 0.07 eV for Pt_{37}/SnO_2. Similar behavior was observed for Pt-nanoparticles on graphene,[15] where the *d*-band centers of the atoms at the interface became more negative. Oppositely, a maximum upshift of 0.20 eV was observed for Pt_{119}/SnO_2 that experienced a small decrease to 0.18 eV for Pt_{233}/SnO_2. It is interesting to note that the change from a downshift to an upshift in the *d*-band centers is for nanoparticles between 37 and 119 atoms. The atoms at the top facet of the supported nanoparticles (except for Pt_{13}/SnO_2) exhibited an upshift in the *d*-band centers, which decreased with increasing the number of layers in the nanoparticle, as the middle layers will dissipate the effect of SnO_2.

Following Hammer-Nørskov model, the upshift of the *d*-band centers will lead to more stable adsorption of oxygenated species, which will decrease with increasing the size of the supported nanoparticle. Moreover, a good correlation between the different values of the electron density distribution and the changes in the *d*-band centers while varying the size of the nanoparticles can confirm the increased stability of oxygenated species in small size Pt-nanoparticles supported on SnO_2. Experimentally, it was reported that the use of SnO_2 as support material for different Pt-loads led to an enhanced OH adsorption, which lowered significantly the ORR activity.[51]

4.3.2.3 Effect of SnO_2 on the nanoparticles' stability. Small size Pt-nanoparticles supported on carbon have shortened lifetime at the operating conditions of the PEFC; the weak interaction between platinum and carbon leads to Pt-atom dissolution, nanoparticle aggregation and detachment from the support.[11] On the other hand, Pt-nanoparticles supported on SnO_2 exhibited stronger stability, although some degradation due to Ostwald ripening was confirmed.[23] In this section, the interaction stability between the nanoparticles and the support was approximated by the adsorption energy. Additionally, the adsorption energy of a Pt-atom, Pt_4, Pt_{13}, and Pt_{37} nanoparticles on graphene, and its effect on the Pt-Pt interaction were compared with the corresponding energies of Pt-nanoparticles supported on SnO_2. Figure 4-11a displays the supported Pt-clusters on graphene. The adsorption energies of all the Pt_n/SnO_2 are more stable than for the Pt_n/graphene systems. For both systems, increasing the size of the nanoparticle increased the total interaction with the support, as shown in Figure 4-11b. On the other hand, the adsorption energy per atom in the nanoparticle decreased with increasing the size of the nanoparticle agreeing with a previous theoretical study[15] on the interaction of Pt-nanoparticles with graphene. The effect of the support material on the Pt-Pt interaction was estimated from their formation energies as shown in Figure 4-11c. It was observed that the cohesive energies of isolated Pt-NPs were close to the formation energies of Pt-NPs supported on graphene, showing the weak interaction between

Pt and graphene.[15] As the size of the Pt-nanoparticles increased, the Pt-Pt interaction control in the most part the stability of the Pt-nanoparticles supported on graphene.

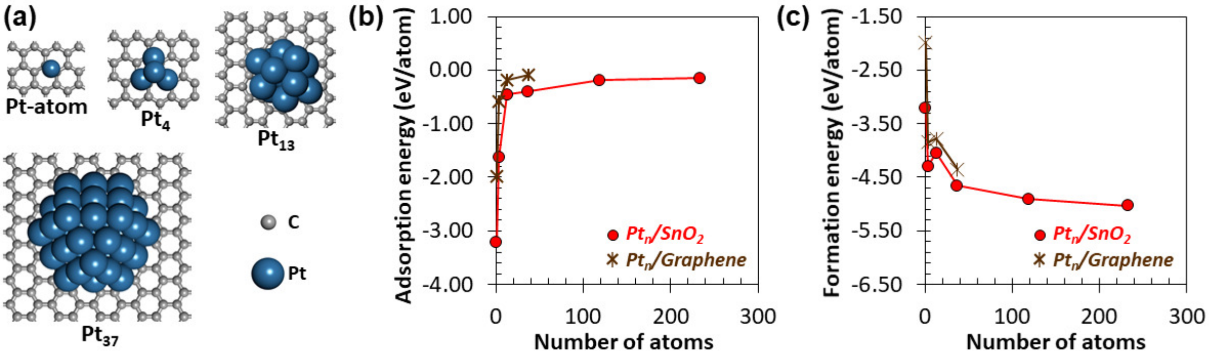

Figure 4-11. Effect of the support on the nanoparticles' stability: (a) models of the Pt_n/graphene, (b) adsorption energies and (c) formation energies of the Pt-nanoparticles supported on SnO_2 (red circles) and graphene (brown asterisks).

This weak interaction was also reported to be responsible for the formation of spherical Pt-nanoparticles, thus the contact between Pt-atoms and C-atoms is limited.[11] On the other hand, the stronger interaction between Pt and SnO_2 led to the formation of semispherical nanoparticles[11] increasing the number of Pt-atom in contact with the surface of the support, and decreasing the agglomeration of Pt-nanoparticles. While other effects such as carbon corrosion might be included in the experimental observations showing the faster degradation of Pt-nanoparticles supported on carbon-based materials. The stronger interaction between the Pt-clusters and SnO_2 up to some extent explain the increased resistance against Pt-atom dissolution, nanoparticle aggregation and detachment from the support compared to the Pt-clusters supported on graphene. The size dependence of the formation energies showed that with increasing the size of the nanoparticle a more stable Pt-Pt interaction is expected, which is opposite to the tendency of the adsorption energy per atom. Therefore, as the size of the nanoparticle increases the stronger Pt-Pt interaction will lead to an increase in the nanoparticle's stability.

The 6th generation density derived electrostatic and chemical (DDEC6) atomic population analysis was conducted to compute the bond orders.[93] The individual bond orders and the sum of bond orders can help provide valuable information regarding the stability and trends in activity. To single out the effect of SnO_2 on the Pt-Pt interaction of the outer-shell atoms, the bond order values were computed for the isolated Pt_4, Pt_{13}, and for the half-spherical clusters and then compared to the respective outer-shell atoms of the supported nanoparticles. The bond order values for the outer-shell atoms of the isolated nanoparticles became larger with increasing their size, as shown in Figure 4-12. Similarly, larger bond orders were observed with increasing the size of the supported Pt-nanoparticles.

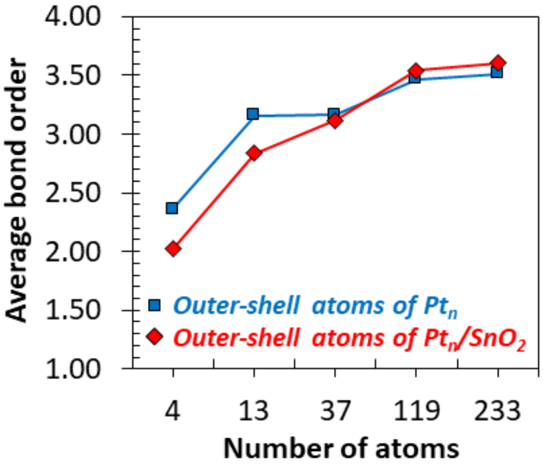

Figure 4-12. Size and support effect on the bond order for the outer-shell atoms of isolated (blue squares) and supported Pt-nanoparticles (red diamonds).

The bond order values of the outer-shell atoms of Pt_4, Pt_{13}, and Pt_{37} supported on SnO_2 were smaller than the values of the outer-shell atoms of isolated Pt-nanoparticles, showing a detrimental effect of SnO_2 in the Pt-Pt interaction. The detrimental effect dissipates for supported Pt-nanoparticles containing more than 37 atoms, i.e., Pt_{119} and Pt_{233}. The weakening of the Pt-Pt interaction due to SnO_2 on the small size Pt-nanoparticles can also explain the Pt-mass loss due to dissolution of the PtO_x formed as consequence of the strong adsorption of oxygenated species.[51,94,95]

4.3.3 O-atom binding energy description, prediction via multi-descriptors. In this section, the limitations of the conventional *d*-band center model via the O-atom binding on Pt-nanoparticles are demonstrated, and a new model to predict the O-atom binding energy taking into consideration the changes in the nanoparticle size and adsorption site effects is proposed based on a linear combination of the Pt-nanoparticles properties. The O-atom binding energy as a function of the *d*-band center is shown in Figure 4-13a. A poor correlation between the two parameters can lead to errors in the estimated O-binding energy larger than 1 eV as shown in Figure 4-13b. Hence, the *d*-band center is not suitable as a single descriptor of the O-binding energy. Thus, based on the different properties of the Pt-nanoparticles a group of six variables were used to describe the energetics of the adsorbent-adsorbate interaction. In Figure 4-14a the predicted O-binding energy as a function of the calculated O-binding energy is shown.

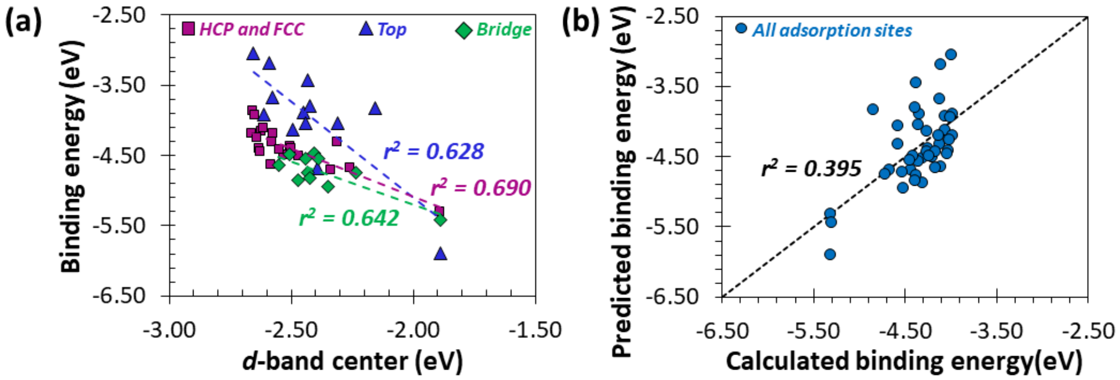

Figure 4-13. Relationship between the binding energies on the pristine Pt-nanoparticles and the *d*-band center: (a) O-atom binding energies on top, bridge, HCP and FCC sites as a function of the *d*-band center, and (b) accuracy of the predicted O-atom binding energies compared to the DFT calculated ones. Linear regression line and coefficients of determination are shown.

The variables associated with the O-binding energy were grouped into three types: (i) Type I variables are the average nearest neighbor (NN) Pt-Pt distance, and the generalized coordination number,[69] which involve only the structural information of the isolated Pt-nanoparticles. (ii) Type II variables involve only the electronic structure of each adsorption site. The nearest neighbor and second nearest neighbor (NN + 2nd NN) *d*-band center and *d*-bandwidth fit in this category. (iii) Type 3 variables are the sum of bond orders of NN and the sum of bond orders of NN + 2nd NN that were obtained after conducting the DDEC6 atomic population analysis.[93] The definition of the NN and 2nd NN is shown in Figure 4-14b.

The predicted O-binding energy, E_{bin}^{pred} was defined as follows:

$$E_{bin}^{pred} = -8.999 - 0.141 d_{Pt-Pt} - 3.317 \varepsilon_{d-band}^{NN+2^{nd}\,NN} - 0.610 \omega_{d-band}^{NN+2^{nd}\,NN} + 0.62944 GCN + 0.253 BO^{NN} - 0.078 BO^{NN+2^{nd}\,NN} \quad (4\text{-}6)$$

where d_{Pt-Pt}, $\varepsilon_{d-band}^{NN+2^{nd}\,NN}$, $\omega_{d-band}^{NN+2^{nd}\,NN}$, GCN, BO^{NN}, $BO^{NN+2^{nd}\,NN}$are the average NN Pt-Pt distance, the NN + 2nd NN *d*-band center and *d*-bandwidth, the generalized coordination number, the NN and the NN + 2nd NN sum of bond order, respectively.

Although the difference between the predicted and DFT calculated O-atom binding energies can be as large as 0.44 eV, this proposed model can predict the O-binding energy more accurately than Hammer-Nørskov model. Additionally, for the first time the variation in the nanoparticle size and adsorption sites were considered, thus making this model suitable to estimate the O-binding energy on more complex systems. Lastly, to obtain the data for the model no additional DFT calculations are required.

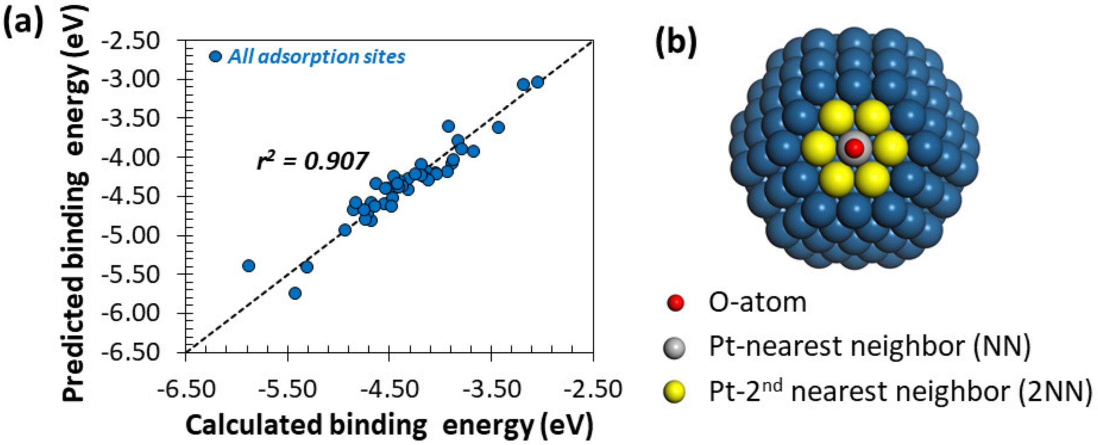

Figure 4-14. Relationship between the binding energies on the pristine Pt-nanoparticles and the proposed model: (a) accuracy of the predicted O-atom binding energies compared to the DFT calculated ones (b) definition of the NN and 2^{nd} NN. Linear regression line and coefficients of determination are shown.

4.3.3.1 Prediction of the O-atom binding energy on the supported Pt-nanoparticles. The O-atom binding energies were calculated using equation 4-5 for ten different configurations of O-atom on Pt_{13}/SnO_2. These energies and their corresponding values of the above-mentioned variables were included in the multi-regression analysis to correct equation 4-6 for additional support effects such us the interaction between the O-atom adsorbed on the nanoparticle and the atoms on the surface of the support.

The new equation that can predict the O-atom binding energy considering the effect of the nanoparticle size, adsorption site and support effect was defined as follows:

$$E_{bin}^{pred} = -12.080 - 0.117 d_{Pt-Pt} - 12.132 \varepsilon_{d-band}^{NN+2^{nd}\,NN} - 2.920 \omega_{d-band}^{NN+2^{nd}\,NN} + 1.011 GCN + 0.233 BO^{NN} - 0.082 BO^{NN+2^{nd}\,NN} \qquad (4\text{-}7)$$

The coefficients in equation 4-7 are the average values after the validation was performed by the holdout method, where the data sample was randomly divided into two sets of data points, the training and the test set, respectively. The size of training set was selected to 3/4 of the data points in the sample and the remaining 1/4 were assigned to the test set. Multi-regression analysis was performed on the training set, then the prediction model obtained was used to estimate and validate the values of the test set. In this study, the training and test sets were selected randomly in ten different cases. Increasing the number of cases in random sub-sampling will lead to a dependence between the training and test sets,[96] thus high variance is expected because the large number of training cases became similar.[97] Thus, in cross-validation five- or tenfold are recommended as a good compromise.[96,97]

In Table 4-1 is shown the statistical analysis of the coefficients in equation 4-6. From Table 4-1, it can be seen a low standard deviation for all the coefficients in equation 4-6 except for the values of the intercept and the coefficient multiplying the *d*-band center, for which the standard deviation was 0.740 and 0.669, respectively. Additionally, larger difference of the maximum and minimum values of the intercept and *d*-band center with respect to the mean value was observed compared to the remaining coefficients. However, the coefficients multiplying the interatomic distance, the NN and NN+2nd NN sum of bond orders showed the largest variability relative to the mean value corresponding to coefficients of variation of 28.63, 17.416, and 16.741%, respectively.

Table 4-1. Descriptive statistical analysis of the coefficients in equation 4-6.

Mean	*Minimum*	*Maximum*	*Variance*	*Standard deviation*	*Coefficient of variation*
-12.080	-13.125	-10.727	0.547	0.740	0.234
-0.117	-0.178	-0.076	0.001	0.034	0.011
-12.132	-13.479	-11.394	0.447	0.669	0.211
-2.920	-3.202	-2.643	0.024	0.155	0.049
1.011	0.895	1.176	0.010	0.102	0.032
0.233	0.141	0.275	0.002	0.041	0.013
-0.082	-0.102	-0.059	0.000	0.014	0.004

In Table 4-2 the coefficients of determination for the training and test sets of the ten cases studied are shown. From Table 4-2 it can be seen that only in two cases the coefficients of determination were smaller than 0.900, and from the ten cases studied an average value larger than 0.900 was obtained, thus it is possible to conclude that the model is robust and appropriate to predict the O-atom binding energies on supported Pt-nanoparticles, taking into consideration the size, adsorption site, and support effects. The relative importance analysis presented in Figure 4-15a is useful for a better understanding of the role played by each variable in the description of the O-atom binding energy.

Table 4-2. Coefficients of determination of the training and test set.

Case	*Training set*	*Test set*
1	0.901	0.860
2	0.903	0.878
3	0.907	0.903
4	0.907	0.904
5	0.902	0.905
6	0.908	0.908
7	0.908	0.916
8	0.893	0.943
9	0.896	0.934
10	0.889	0.946

From Figure 4-15a, for the isolated Pt-nanoparticles, the variable that contributes the most to describe the O-atom binding energy is the generalized coordination number followed closely by the *d*-band center. For the supported nanoparticles, the contribution of the generalized coordination number, *d*-band center, *d*-bandwidth increased by ca. 8, 10, and 2%, respectively. The effect of SnO_2 had almost no effect on the sum of bond orders of nearest and second nearest neighbors, which have a relative importance of 10%. The interatomic distance and the nearest neighbor bond order showed a decreased in their contribution to describe the O-atom binding energy.

Employing equation 4-7 the O-atom binding energy on the supported Pt-nanoparticles was predicted for over 150 different adsorption sites. The predicted O-atom binding energy on the supported Pt-nanoparticles, shown in Figure 4-15b, are more negative than on the isolated Pt-nanoparticles, except for some top sites of Pt_{119}/SnO_2 and Pt_{233}/SnO_2. As the size of the Pt-NPs supported on SnO_2 increased, the support effect on the O-atom binding energy decreased, and less negative values for the O-atom binding energy were obtained with increasing the size of the Pt-nanoparticles. This tendency agrees well with previous observations from cyclic voltammograms of Pt-nanoparticles supported on Nb-doped SnO_2, where decreasing the size of the nanoparticle led to a negative shift in the oxygen desorption peak potential indicating stronger adsorption of oxygenated species.[46] It should be noted that in the previously mentioned study[46] the Pt-nanoparticles were supported on Nb-doped SnO_2. Thus the interplay between the dopant and the particle size effect may have made the oxygenated species less prone to interact with Pt-nanoparticles > 2.6 nm. Regarding the nanoparticle size effect, it was reported that the oxophilicity of metal nanoparticles increased with decreasing the particle size,[94,95,98] which can lead to the formation PtO_x[95] that are known to be prone to dissolution during the electroreduction of O_2.[99]

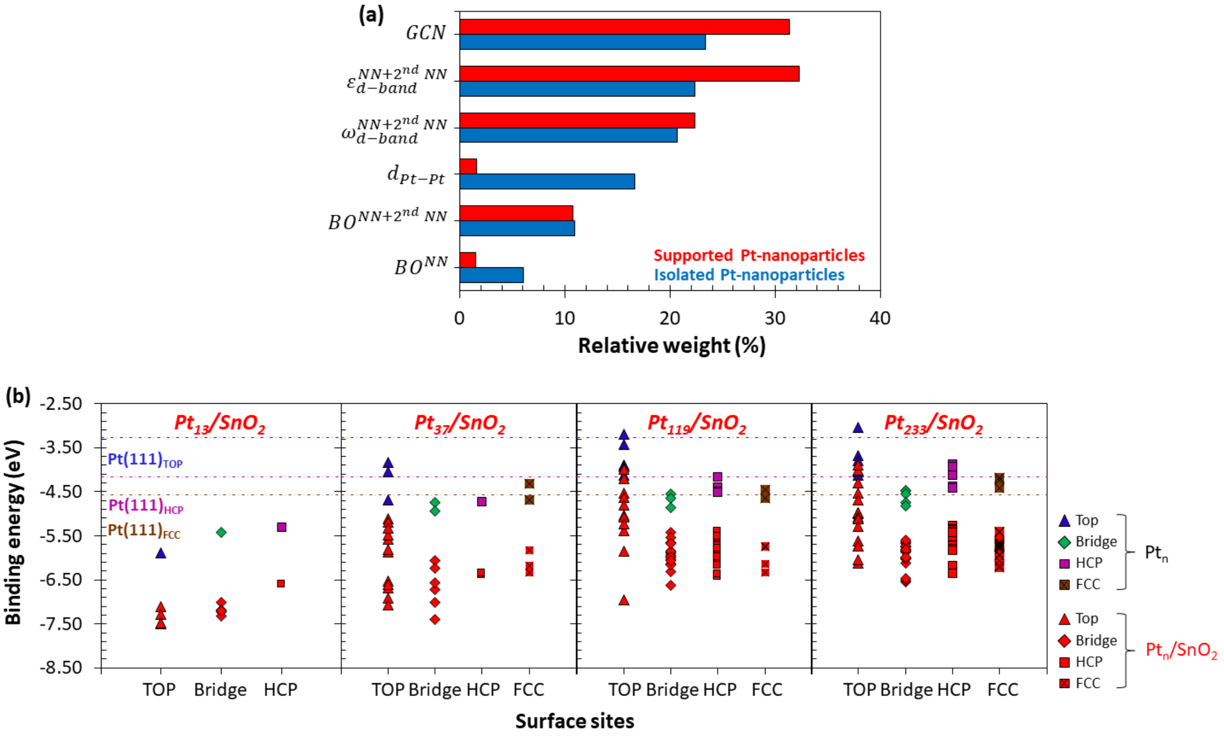

Figure 4-15. Predicted O-atom binding energies on Pt-nanoparticles supported on SnO_2. (a) Relative importance analysis of the variables describing the O-atom binding energies on isolated (blue bars) and supported Pt-nanoparticles (red bars), and (b) predicted effect of SnO_2 on O-atom binding energies. Red triangles, diamonds, squares, and "X" filled squares indicate the top, bridge, HCP, and FCC adsorption sites, respectively. The O-atom binding energies on the isolated Pt-nanoparticles are shown for comparison, blue triangles, green diamonds, pink squares, and "X" filled brown squares indicate top, bridge, HCP, and FCC adsorption sites, respectively. The O-atom binding energies on the Pt(111) sites are shown as reference.

Furthermore, this work results showing a strong interaction of O-atom on Pt-nanoparticles supported on stoichiometric SnO_2 compared to that on graphite-supported Pt agree well with experimental observations where the strong adsorption of oxygenated species on Pt-nanoparticles with diameters of 2.0 nm supported on oxidized SnO_2, corresponding to a stoichiometric Sn:O ratio of 1:2[100] was responsible for the low ORR activity compared to glassy carbon.[51] The ORR activity increased only after an extended Pt-regions were formed on oxidized SnO_2 due to the large Pt-loadings, where the effect of the support is minimum. In this study, the largest supported Pt-nanoparticle, Pt_{233}/SnO_2, has a size of ca. 2.11 nm, and showed to be a good adsorbent for the O-atom, which will block the active sites for the ORR to occur. The results in this work show similar tendency with experimental observations, where SnO_2 as an alternative to carbon will help to stabilize the interaction of oxygenated species on Pt-nanoparticles, blocking the active sites, and lowering ORR activity.

4.4 CONCLUSIONS

The effect of SnO_2 as support material on the geometrical features, electronic properties, and stability of Pt-nanoparticles was investigated via DFT method. Due to electron transfer from the nanoparticle to the support the outer-shell atoms of the supported nanoparticles became more oxidized, thus a stronger interaction of oxygenated species should be expected. The *d*-band center analysis sustained the idea of a more stable adsorption on the surface of the supported platinum nanoparticles. The predicted O-atom binding energies showed the negative effect of SnO_2 on the ORR activity of Pt-nanoparticles, where due to the effect of SnO_2 oxygenated species can effectively block the active sites of the Pt-nanoparticles required for the adsorption and dissociation of O_2.

In terms of durability, SnO_2 can help to inhibit the migration and aggregation of Pt-nanoparticles compared to graphene as support material due to a stronger interaction between the nanoparticle and SnO_2, which was approximated by the nanoparticles adsorption energy. Nevertheless, the promoted interaction between oxygenated species and Pt-nanoparticles supported on SnO_2 can lead to the formation of PtO_x that will dissolve during the ORR reaction. It is found that SnO_2 weakened the interatomic interaction of the outer-shell atoms of nanoparticles containing less than 119 atoms, while for larger nanoparticles a slight increase in the Pt-Pt interaction was observed, which in part can explain the higher stability of platinum nanoparticles when SnO_2 is used a support material.

REFERENCES

(4-1) Ishimoto, T.; Koyama, M. A Review of Molecular-Level Mechanism of Membrane

Degradation in the Polymer Electrolyte Fuel Cell. *Membranes* **2012**, *2* (3), 395–414.

(4-2) Seo, J. K.; Khetan, A.; Seo, M. H.; Kim, H.; Han, B. First-Principles Thermodynamic Study of the Electrochemical Stability of Pt Nanoparticles in Fuel Cell Applications. *J. Power Sources* **2013**, *238*, 137–143.

(4-3) Kakinuma, K.; Chino, Y.; Senoo, Y.; Uchida, M.; Kamino, T.; Uchida, H.; Deki, S.; Watanabe, M. Characterization of Pt Catalysts on Nb-Doped and Sb-Doped $SnO_{2-\delta}$ Support Materials with Aggregated Structure by Rotating Disk Electrode and Fuel Cell Measurements. *Electrochim. Acta* **2013**, *110*, 316–324.

(4-4) De Lile, J. R.; Zhou, S. Theoretical Modeling of the PEMFC Catalyst Layer: A Review of Atomistic Methods. *Electrochim. Acta* **2015**, *177*, 4–20.

(4-5) Higgins, D.; Hoque, M. A.; Seo, M. H.; Wang, R.; Hassan, F.; Choi, J. Y.; Pritzker, M.; Yu, A.; Zhang, J.; Chen, Z. Development and Simulation of Sulfur-Doped Graphene Supported Platinum with Exemplary Stability and Activity towards Oxygen Reduction. *Adv. Funct. Mater.* **2014**, *24*, 4325–4336.

(4-6) Chino, Y.; Taniguchi, K.; Senoo, Y.; Kakinuma, K.; Hara, M.; Watanabe, M.; Uchida, M. Effect of Added Graphitized CB on Both Performance and Durability of Pt/Nb-SnO_2 Cathodes for PEFCs. *J. Electrochem. Soc.* **2015**, *162* (7), F736–F743.

(4-7) Knights, S. D.; Colbow, K. M.; St-Pierre, J.; Wilkinson, D. P. Aging Mechanisms and Lifetime of PEFC and DMFC. *J. Power Sources* **2004**, *127* (1–2), 127–134.

(4-8) Yousfi-Steiner, N.; Moçotéguy, P.; Candusso, D.; Hissel, D. A Review on Polymer Electrolyte Membrane Fuel Cell Catalyst Degradation and Starvation Issues: Causes, Consequences and Diagnostic for Mitigation. *J. Power Sources* **2009**, *194* (1), 130–145.

(4-9) Peighambardoust, S. J.; Rowshanzamir, S.; Amjadi, M. Review of the Proton Exchange Membranes for Fuel Cell Applications. *Int. J. Hydrogen Energy* **2010**, *35* (17), 9349–9384.

(4-10) Sharma, S.; Pollet, B. G. Support Materials for PEMFC and DMFC Electrocatalysts—a Review. *J. Power Sources* **2012**, *208*, 96–119.

(4-11) Daio, T.; Staykov, A.; Guo, L.; Liu, J.; Tanaka, M.; Lyth, S. M.; Sasaki, K. Lattice Strain Mapping of Platinum Nanoparticles on Carbon and SnO_2 Supports. *Sci. Rep.* **2015**, *5*, 13126.

(4-12) Escaño, M. C. S. First-Principles Calculations of the Dissolution and Coalescence Properties of Pt Nanoparticle ORR Catalysts: The Effect of Nanoparticle Shape. *Nano Res.* **2015**, *8* (5), 1689–1697.

(4-13) Stamenkovic, V. R.; Fowler, B.; Mun, B. S.; Wang, G.; Ross, P. N.; Lucas, C. A.; Marković, N. M. Improved Oxygen Reduction Activity on Pt_3Ni (111) via Increased Surface Site Availability. *Science* **2007**, *315* (5811), 493–497.

(4-14) Yu, X.; Ye, S. Recent Advances in Activity and Durability Enhancement of Pt/C Catalytic Cathode in PEMFC: Part I. Physico-Chemical and Electronic Interaction between Pt and Carbon Support, and Activity Enhancement of Pt/C Catalyst. *J. Power Sources* **2007**, *172* (1), 133–144.

(4-15) Verga, L. G.; Aarons, J.; Sarwar, M.; Thompsett, D.; Russell, A. E.; Skylaris, C.-K. Effect of Graphene Support on Large Pt Nanoparticles. *Phys. Chem. Chem. Phys.* **2016**, *18* (48), 32713–32722.

(4-16) Seger, B.; Kamat, P. V. Electrocatalytically Active Graphene-Platinum Nanocomposites. Role of 2-D Carbon Support in PEM Fuel Cells. *J. Phys. Chem. C* **2009**, *113* (19), 7990–7995.

(4-17) Antolini, E. Carbon Supports for Low-Temperature Fuel Cell Catalysts. *Appl. Catal. B Environ.* **2009**, *88* (1–2), 1–24.

(4-18) Singh, R. N.; Awasthi, R.; Sharma, C. S. An Overview of Recent Development of Platinum-Based Cathode Materials for Direct Methanol Fuel Cells. *Int. J. Electrochem. Sci.* **2014**, *9*, 5607–5639.

(4-19) Kim, J.; Jang, J.-S.; Peck, D.-H.; Lee, B.; Yoon, S.-H.; Jung, D.-H. Methanol-Tolerant Platinum-Palladium Catalyst Supported on Nitrogen-Doped Carbon Nanofiber for High Concentration Direct Methanol Fuel Cells. *Nanomaterials* **2016**, *6* (8), 148.

(4-20) Park, Y.-C.; Tokiwa, H.; Kakinuma, K.; Watanabe, M.; Uchida, M. Effects of Carbon Supports on Pt Distribution, Ionomer Coverage and Cathode Performance for Polymer Electrolyte Fuel Cells. *J. Power Sources* **2016**, *315*, 179–191.

(4-21) Lázaro, M. J.; Calvillo, L.; Celorrio, V.; Pardo, J. I.; Perathoner, S.; Moliner, R. Study and Application of Vulcan XC-72 in Low Temperature Fuel Cells. In *Carbon Black: Production, Properties and Uses*; Sanders, I. J., Peeten, T. L., Eds.; Nova Science Publishers, Inc., 2011; pp. 41–68.

(4-22) Trogadas, P.; Fuller, T. F.; Strasser, P. Carbon as Catalyst and Support for Electrochemical Energy Conversion. *Carbon* **2014**, *75*, 5–42.

(4-23) Takasaki, F.; Matsuie, S.; Takabatake, Y.; Noda, Z.; Hayashi, A.; Shiratori, Y.; Ito, K.; Sasaki, K. Carbon-Free Pt Electrocatalysts Supported on SnO_2 for Polymer Electrolyte Fuel Cells: Electrocatalytic Activity and Durability. *J. Electrochem. Soc.* **2011**, *158* (10), B1270–B1275.

(4-24) Che, G.; Lakshmi, B. B.; Fisher, E. R.; Martin, C. R. Carbon Nanotubule Membranes for Electrochemical Energy Storage and Production. *Nature* **1998**, *393* (6683), 346.

(4-25) Dudin, P. V; Unwin, P. R.; Macpherson, J. V. Electrochemical Nucleation and Growth of Gold Nanoparticles on Single-Walled Carbon Nanotubes: New Mechanistic Insights. *J. Phys. Chem. C* **2010**, *114* (31), 13241–13248.

(4-26) Park, S.; Shao, Y.; Kou, R.; Viswanathan, V. V; Towne, S. A.; Rieke, P. C.; Liu, J.; Lin, Y.; Wang, Y. Polarization Losses under Accelerated Stress Test Using Multiwalled Carbon Nanotube Supported Pt Catalyst in PEM Fuel Cells. *J. Electrochem. Soc.* **2011**, *158* (3), B297–B302.

(4-27) Guo, S.; Dong, S.; Wang, E. Three-Dimensional Pt-on-Pd Bimetallic Nanodendrites Supported on Graphene Nanosheet: Facile Synthesis and Used as an Advanced Nanoelectrocatalyst for Methanol Oxidation. *ACS Nano* **2009**, *4* (1), 547–555.

(4-28) Qu, L.; Liu, Y.; Baek, J.-B.; Dai, L. Nitrogen-Doped Graphene as Efficient Metal-Free Electrocatalyst for Oxygen Reduction in Fuel Cells. *ACS Nano* **2010**, *4* (3), 1321–1326.

(4-29) Liu, S.; Wang, J.; Zeng, J.; Ou, J.; Li, Z.; Liu, X.; Yang, S. “Green” Electrochemical Synthesis of Pt/graphene Sheet Nanocomposite Film and Its Electrocatalytic Property. *J. Power Sources* **2010**, *195* (15), 4628–4633.

(4-30) Bessel, C. A.; Laubernds, K.; Rodriguez, N. M.; Baker, R. T. K. Graphite Nanofibers as an Electrode for Fuel Cell Applications. *J. Phys. Chem. B* **2001**, *105* (6), 1115–1118.

(4-31) Maiyalagan, T. Pt–Ru Nanoparticles Supported PAMAM Dendrimer Functionalized Carbon Nanofiber Composite Catalysts and Their Application to Methanol Oxidation. *J. Solid State Electrochem.* **2009**, *13* (10), 1561–1566.

(4-32) Ding, J.; Chan, K.-Y.; Ren, J.; Xiao, F. Platinum and Platinum–ruthenium Nanoparticles Supported on Ordered Mesoporous Carbon and Their Electrocatalytic Performance for Fuel Cell Reactions. *Electrochim. Acta* **2005**, *50* (15), 3131–3141.

(4-33) Su, F.; Zeng, J.; Bao, X.; Yu, Y.; Lee, J. Y.; Zhao, X. S. Preparation and Characterization of Highly Ordered Graphitic Mesoporous Carbon as a Pt Catalyst Support for Direct Methanol Fuel Cells. *Chem. Mater.* **2005**, *17* (15), 3960–3967.

(4-34) Joo, S. H.; Pak, C.; You, D. J.; Lee, S.-A.; Lee, H. I.; Kim, J. M.; Chang, H.; Seung, D. Ordered Mesoporous Carbons (OMC) as Supports of Electrocatalysts for Direct Methanol Fuel Cells (DMFC): Effect of Carbon Precursors of OMC on DMFC Performances. *Electrochim. Acta* **2006**, *52* (4), 1618–1626.

(4-35) Swain, G. M. The Use of CVD Diamond Thin Films in Electrochemical Systems. *Adv. Mater.* **1994**, *6* (5), 388–392.

(4-36) Xu, J.; Granger, M. C.; Chen, Q.; Strojek, J. W.; Lister, T. E.; Swain, G. M. Peer Reviewed: Boron-Doped Diamond Thin-Film Electrodes. *Anal. Chem.* **1997**, *69* (19), 591A–597A.

(4-37) Sasaki, K.; Takasaki, F.; Noda, Z.; Hayashi, S.; Shiratori, Y.; Ito, K. Alternative Electrocatalyst Support Materials for Polymer Electrolyte Fuel Cells. *ECS Trans.* **2010**, *33* (1), 473–482.

(4-38) Mädler, L.; Sahm, T.; Gurlo, A.; Grunwaldt, J.-D.; Barsan, N.; Weimar, U.; Pratsinis, S. E. Sensing Low Concentrations of CO Using Flame-Spray-Made Pt/SnO_2 Nanoparticles. *J. Nanoparticle Res.* **2006**, *8* (6), 783–796.

(4-39) Boltz, J.; Koehl, D.; Wuttig, M. Low Temperature Sputter Deposition of SnO_x: Sb Films for Transparent Conducting Oxide Applications. *Surf. Coatings Technol.* **2010**, *205* (7), 2455–2460.

(4-40) Turgut, G.; Sönmez, E. Synthesis and Characterization of Mo Doped SnO_2 Thin Films with Spray Pyrolysis. *Superlattices Microstruct.* **2014**, *69*, 175–186.

(4-41) Roth, D.; Gelin, P.; Tena, E.; Primet, M. Combustion of Methane at Low Temperature over Pd and Pt Catalysts Supported on Al_2O_3, SnO_2 and Al_2O_3-Grafted SnO_2. *Top. Catal.* **2001**, *16* (1–4), 77–82.

(4-42) Urfels, L.; Gélin, P.; Primet, M.; Tena, E. Complete Oxidation of Methane at Low Temperature over Pt Catalysts Supported on High Surface Area SnO_2. *Top. Catal.* **2004**, *30* (1–4), 427–432.

(4-43) Bariås, O. A.; Holmen, A.; Blekkan, E. A. Propane Dehydrogenation over Supported Platinum Catalysts: Effect of Tin as a Promoter. *Catal. Today* **1995**, *24* (3), 361–364.

(4-44) Llorca, J.; Homs, N.; Leon, J.; Sales, J.; Fierro, J. L. G.; De La Piscina, P. R. Supported Pt–Sn Catalysts Highly Selective for Isobutane Dehydrogenation: Preparation, Characterization and Catalytic Behavior. *Appl. Catal. A Gen.* **1999**, *189* (1), 77–86.

(4-45) Masao, A.; Noda, S.; Takasaki, F.; Ito, K.; Sasaki, K. Carbon-Free Pt Electrocatalysts Supported on SnO_2 for Polymer Electrolyte Fuel Cells. *Electrochem. Solid-State Lett.* **2009**, *12* (9), B119-B122.

(4-46) Tsukatsune, T.; Takabatake, Y.; Noda, Z.; Daio, T.; Zaitsu, A.; Lyth, S. M.; Hayashi, A.; Sasaki, K. Platinum-Decorated Tin Oxide and Niobium-Doped Tin Oxide PEFC Electrocatalysts: Oxygen Reduction Reaction Activity. *J. Electrochem. Soc.* **2014**, *161* (12), F1208–F1213.

(4-47) Oh, H.; Nong, H. N.; Strasser, P. Preparation of Mesoporous Sb-, F-, and In-doped SnO_2 Bulk Powder with High Surface Area for Use as Catalyst Supports in Electrolytic Cells. *Adv. Funct. Mater.* **2015**, *25* (7), 1074–1081.

(4-48) Gurrola, M. P.; Guerra-Balcázar, M.; Álvarez-Contreras, L.; Nava, R.; Ledesma-García, J.; Arriaga, L. G. High Surface Electrochemical Support Based on Sb-Doped SnO_2. *J. Power Sources* **2013**, *243*, 826–830.

(4-49) Mohanta, P. K.; Glökler, C.; Arenas, A. O.; Jörissen, L. Sb Doped SnO_2 as a Stable Cathode Catalyst Support for Low Temperature Polymer Electrolyte Membrane Fuel Cell. *Int. J. Hydrogen Energy* **2017**, *42* (46), 27950–27961.

(4-50) Senoo, Y.; Taniguchi, K.; Kakinuma, K.; Uchida, M.; Uchida, H.; Deki, S.; Watanabe, M. Cathodic Performance and High Potential Durability of Ta-$SnO_{2-\delta}$-Supported Pt Catalysts for PEFC Cathodes. *Electrochem. Commun.* **2015**, *51*, 37–40.

(4-51) Rabis, A.; Binninger, T.; Fabbri, E.; Schmidt, T. J. Impact of Support Physicochemical Properties on the CO Oxidation and the Oxygen Reduction Reaction Activity of Pt/SnO_2 Electrocatalysts. *J. Phys. Chem. C* **2018,** 122,4739-4746.

(4-52) Fabbri, E.; Rabis, A.; Chino, Y.; Uchida, M.; Schmidt, T. J. Boosting Pt Oxygen Reduction Reaction Activity by Tuning the Tin Oxide Support. *Electrochem. Commun.* **2017**, *83*, 90–95.

(4-53) Zyubin, A. S.; Zyubina, T. S.; Dobrovol'skii, Y. A.; Volokhov, V. M. Interaction of Platinum Nanoparticles with Different Types of Tin Dioxide Surface: Quantum-Chemical Modeling. *Russ. J. Inorg. Chem.* **2013**, *58* (1), 56–61.

(4-54) Zyubin, A. S.; Zyubina, T. S.; Dobrovol'skii, Y. A.; Frolova, L. A.; Volokhov, V. M. Platinum Nanoparticles on the Antimony-Doped Tin Dioxide Surface: Quantum-Chemical Modeling. *Russ. J. Inorg. Chem.* **2013**, *58* (12), 1489–1495.

(4-55) Zyubina, T. S.; Zyubin, A. S.; Dobrovol, Y. A.; Volokhov, V. M. Quantum Chemical Modeling of Hydrogen Migration on the Pt_{29}/SnO_2 Composite Catalyst. *Russ. Chem. Bull.* **2015**, *64* (4), 752–758.

(4-56) Zyubina, T. S.; Zyubin, A. S.; Dobrovol'skii, Y. A.; Volokhov, V. M. Interaction of Dioxygen with the Platinum $Pt_{19}/SnO_2/H_2$ Cluster: DFT Calculation. *Russ. J. Inorg. Chem.* **2013**, *58* (3), 311–319.

(4-57) Han, B. C.; Miranda, C. R.; Ceder, G. Effect of Particle Size and Surface Structure on Adsorption of O and OH on Platinum Nanoparticles: A First-Principles Study. *Phys. Rev. B* **2008**, *77* (7), 075410.

(4-58) İnoğlu, N.; Kitchin, J. R. New Solid-State Table: Estimating *d*-Band Characteristics for Transition Metal Atoms. *Mol. Simul.* **2010**, *36* (7–8), 633.

(4-59) Hammer, B.; Nørskov, J. K. Theoretical Surface Science and Catalysis—calculations and Concepts. In *Advances in Catalysis*; Elsevier, 2000; Vol. 45, pp. 71–129.

(4-60) Lu, C.; Lee, I. C.; Masel, R. I.; Wieckowski, A.; Rice, C. Correlations between the Heat of Adsorption and the Position of the Center of the D-Band: Differences between Computation and Experiment. *J. Phys. Chem. A* **2002**, *106* (13), 3084–3091.

(4-61) Kim, G.; Kawazoe, Y.; Lee, K.-R. Controlled Catalytic Properties of Platinum Clusters on Strained Graphene. *J. Phys. Chem. Lett.* **2012**, *3* (15), 1989–1996.

(4-62) Greeley, J.; Nørskov, J. K. A General Scheme for the Estimation of Oxygen Binding Energies on Binary Transition Metal Surface Alloys. *Surf. Sci.* **2005**, *592* (1–3), 104–111.

(4-63) Jiang, T.; Mowbray, D. J.; Dobrin, S.; Falsig, H.; Hvolbæk, B.; Bligaard, T.; Nørskov, J. K. Trends in CO Oxidation Rates for Metal Nanoparticles and Close-Packed, Stepped, and Kinked Surfaces. *J. Phys. Chem. C* **2009**, *113* (24), 10548–10553.

(4-64) Kibler, L. A.; El-Aziz, A. M.; Hoyer, R.; Kolb, D. M. Tuning Reaction Rates by Lateral Strain in a Palladium Monolayer. *Angew. Chemie Int. Ed.* **2005**, *44* (14), 2080–2084.

(4-65) Mavrikakis, M.; Hammer, B.; Nørskov, J. K. Effect of Strain on the Reactivity of Metal Surfaces. *Phys. Rev. Lett.* **1998**, *81* (13), 2819–2822

(4-66) Stamenkovic, V.; Mun, B. S.; Mayrhofer, K. J. J.; Ross, P. N.; Markovic, N. M.; Rossmeisl, J.; Greeley, J.; Nørskov, J. K. Changing the Activity of Electrocatalysts for Oxygen Reduction by Tuning the Surface Electronic Structure. *Angew. Chemie Int. Ed.* **2006**, *45* (18), 2897–2901.

(4-67)Takigawa, I.; Shimizu, K.; Tsuda, K.; Takakusagi, S. Machine Learning Predictions of Factors Affecting the Activity of Heterogeneous Metal Catalysts. In *Nanoinformatics*; Tanaka, I., Ed.; Springer Singapore: Singapore, 2018; pp 45–64.

(4-68) Mpourmpakis, G.; Andriotis, A. N.; Vlachos, D. G. Identification of Descriptors for the CO Interaction with Metal Nanoparticles. *Nano Lett.* **2010**, *10* (3), 1041–1045

(4-69) Calle-Vallejo, F.; Martínez, J. I.; García-Lastra, J. M.; Sautet, P.; Loffreda, D. Fast Prediction of Adsorption Properties for Platinum Nanocatalysts with Generalized Coordination Numbers. *Angew. Chemie Int. Ed.* **2014**, *53* (32), 8316–8319.

(4-70) Gasper, R.; Shi, H.; Ramasubramaniam, A. Adsorption of CO on Low-Energy, Low-Symmetry Pt Nanoparticles: Energy Decomposition Analysis and Prediction via Machine-Learning Models. *J. Phys. Chem. C* **2017**, *121* (10), 5612–5619.

(4-71) Kresse, G.; Hafner, J. Ab Initio Molecular Dynamics for Liquid Metals. *Phys. Rev. B: Condens. Matter. Phys.* **1993**, *47*, 558-561.

(4-72) Kresse, G.; Furthmüller, J. Efficient Iterative Schemes for Ab Initio Total-Energy Calculations Using a Plane-Wave Basis Set. *Phys. Rev. B: Condens. Matter. Phys.* **1996**, *54*, 11169-11186.

(4-73) Kresse, G.; Furthmüller, J. Efficiency of Ab-Initio Total Energy Calculations for Metals and Semiconductors Using a Plane-Wave Basis Set. *Comput. Mater. Sci.* **1996**, *6*, 15-50.

(4-74) Blöchl, P. E. Projector Augmented-Wave Method. *Phys. Rev. B: Condens. Matter. Phys.* **1994**, *50*, 17953-17979.

(4-75) Arblaster, J. W. Crystallographic Properties of Platinum. *Platin. Met. Rev.* **1997**, *41* (1), 12–21.

(4-76) Haines, J.; Léger, J. M. X-Ray Diffraction Study of the Phase Transitions and Structural Evolution of Tin Dioxide at High Pressure: Relationships between Structure Types and Implications for Other Rutile-Type Dioxides. *Phys. Rev. B* **1997**, *55* (17), 11144.

(4-77) Krüger, S.; Vent, S.; Rösch, N. Size Dependence of Bond Length and Binding Energy in Palladium and Gold Clusters. *Ber. Bunsenges. Phys. Chem.* **1997**, *101* (11), 1640–1643.

(4-78) Koitz, R.; Soini, T. M.; Genest, A.; Trickey, S. B.; Rösch, N. Scalable Properties of Metal Clusters: A Comparative Study of Modern Exchange-Correlation Functionals. *J. Chem. Phys.* **2012**, *137* (3), 34102.

(4-79) Yudanov, I. V; Metzner, M.; Genest, A.; Rösch, N. Size-Dependence of Adsorption Properties of Metal Nanoparticles: A Density Functional Study on Palladium Nanoclusters. *J. Phys. Chem. C* **2008**, *112* (51), 20269–20275.

(4-80) Roldán, A.; Viñes, F.; Illas, F.; Ricart, J. M.; Neyman, K. M. Density Functional Studies of Coinage Metal Nanoparticles: Scalability of Their Properties to Bulk. *Theor. Chem. Acc.* **2008**, *120* (4–6), 565–573.

(4-81) Gallego, S.; Ocal, C.; Soria, F. Surface and Bulk Reconstruction of Pt (111) 1×1. *Surf. Sci.* **1997**, *377*, 18–22.

(4-82) Qi, W. H.; Wang, M. P. Size Effect on the Cohesive Energy of Nanoparticle. *J. Mater. Sci. Lett.* **2002**, *21* (22), 1743–1745.

(4-83) Roduner, E. Size Matters: Why Nanomaterials Are Different. *Chem. Soc. Rev.* **2006**, *35* (7), 583–592.

(4-84) Kittel, C.; McEuen, P.; McEuen, P. *Introduction to Solid State Physics*; 8th edition. Wiley New York, 1996; Vol. 8.

(4-85) Nanba, Y.; Ishimoto, T.; Koyama, M. Structural Stability of Ruthenium Nanoparticles: A Density Functional Theory Study. *J. Phys. Chem. C* **2017**, *121* (49), 27445–27452.

(4-86) Jinnouchi, R.; Toyoda, E.; Hatanaka, T.; Morimoto, Y. First Principles Calculations on Site-Dependent Dissolution Potentials of Supported and Unsupported Pt Particles. *J. Phys. Chem. C* **2010**, *114* (41), 17557–17568.

(4-87) Li, L.; Larsen, A. H.; Romero, N. A.; Morozov, V. A.; Glinsvad, C.; Abild-Pedersen, F.; Greeley, J.; Jacobsen, K. W.; Nørskov, J. K. Investigation of Catalytic Finite-Size-Effects of Platinum Metal Clusters. *J. Phys. Chem. Lett.* **2013**, *4* (1), 222–226.

(4-88) Hammer, B.; Morikawa, Y.; Nørskov, J. K. CO Chemisorption at Metal Surfaces and Overlayers. *Phys. Rev. Lett.* **1996**, *76* (12), 2141.

(4-89) Hammer, B.; Nørskov, J. K. Theoretical Surface Science and Catalysis—calculations and Concepts. In *Advances in Catalysis*; Elsevier, 2000; Vol. 45, pp. 71–129.

(4-90) Greeley, J.; Stephens, I. E. L.; Bondarenko, A. S.; Johansson, T. P.; Hansen, H. A.; Jaramillo, T. F.; Rossmeisl, J.; Chorkendorff, I.; Nørskov, J. K. Alloys of Platinum and Early Transition Metals as Oxygen Reduction Electrocatalysts. *Nat. Chem.* **2009**, *1* (7), 552–556.

(4-91) Shao, M.; Peles, A.; Shoemaker, K. Electrocatalysis on Platinum Nanoparticles: Particle Size Effect on Oxygen Reduction Reaction Activity. *Nano Lett.* **2011**, *11* (9), 3714–3719.

(4-92) Nørskov, J. K.; Rossmeisl, J.; Logadottir, A.; Lindqvist, L.; Kitchin, J. R.; Bligaard, T.; Jónsson, H. Origin of the Overpotential for Oxygen Reduction at a Fuel-Cell Cathode. *J. Phys. Chem. B* **2004**, *108* (46), 17886–17892.

(4-93) Manz, T. A. Introducing DDEC6 Atomic Population Analysis: Part 3. Comprehensive Method to Compute Bond Orders. *RSC Adv.* **2017**, *7* (72), 45552–45581.

(4-94) Mayrhofer, K. J. J.; Blizanac, B. B.; Arenz, M.; Stamenkovic, V. R.; Ross, P. N.; Markovic, N. M. The Impact of Geometric and Surface Electronic Properties of Pt-Catalysts on the Particle Size Effect in Electrocatalysis. *J. Phys. Chem. B* **2005**, *109* (30), 14433–14440.

(4-95) Fuentes, S.; Figueras, F. Hydrogenolysis of Cyclopentane and Hydrogenation of Benzene on Palladium Catalysts of Widely Varying Dispersion. *J. Chem. Soc. Faraday Trans. 1 Phys. Chem. Condens. Phases* **1978**, *74*, 174.

(4-96) Kohavi, R. A Study of Cross-Validation and Bootstrap for Accuracy Estimation and Model Selection. In *Ijcai*; Montreal, Canada, 1995; Vol. 14, pp 1137–1145.

(4-97) Hastie, T.; Tibshirani, R.; Friedman, J. The Elements of Statistical Learning. Data Mining, Inference, and Prediction. Springer-Verlag New York, Inc., New York 2001.

(4-98) Fabbri, E.; Taylor, S.; Rabis, A.; Levecque, P.; Conrad, O.; Kötz, R.; Schmidt, T. J. The Effect of Platinum Nanoparticle Distribution on Oxygen Electroreduction Activity and Selectivity. *ChemCatChem* **2014**, 1410-1418.

(4-99) Kuhn, A. T.; Randle, T. H. Effect of Oxide Thickness on the Rates of Some Redox Reactions on a Platinum Electrode. *J. Chem. Soc., Faraday Trans. 1* **1985**, *81*, 403−419

(4-100) Rabis, A.; Kramer, D.; Fabbri, E.; Worsdale, M.; Kötz, R.; Schmidt, T. J. Catalyzed SnO_2 Thin Films: Theoretical and Experimental Insights into Fabrication and Electrocatalytic Properties. *J. Phys. Chem. C* **2014**, *118*, 11292−11302.

CHAPTER 5

CONCLUSIONS AND FUTURE WORK

5.1 CONCLUSIONS

In this work, the roles of $BaTiO_3$ as solid oxide fuel cell (SOFC) electrocatalyst and SnO_2 as support material for polymer electrolyte fuel cell (PEFC) electrocatalyst were investigated from an atomistic point of view.

As SOFC electrocatalyst material, $BaTiO_3$ exhibited low performance, which was attribute to its low catalytic activity. The activity of $BaTiO_3$ was approximated by the reaction of H_2S, $H_{2,}$ and CH_4 on $BatiO_3(001)$ surfaces. The sulfidation process of the $BaTiO_3$ catalyst will occur by exchanging the S-atom from the H_2S molecule with an O-atom from the surface. This process involves either the partial or total formation of an oxygen vacancy, which was calculated to be stable at the operating conditions of the SOFC. The H_2 oxidation reaction on $BaTiO_3$ also involves the formation of an oxygen vacancy, contrary to the reaction mechanism on nickel and yttria-stabilized zirconia (Ni-YSZ) composed anode where charge-transfer reactions such as H-atom and O^{2-} migration kinetically govern the activity of the anode. The H_2 oxidation reaction will proceed slowly due to the increased energy difference between intermediates, so larger activation energies are to be expected, which in part can explain the poor initial performance of the SOFC employing $BaTiO_3$ as anode material. For the H_2 oxidation reaction, the presence of sulfur activated the H-H bond breaking, led to the formation of new reaction intermediates and promoted the formation of some intermediates, such as oxygen vacancy formation. Due to the presence of sulfur, the species formed after sequentially stripping the H-atoms from the CH_4 molecule were stabilized depending on the termination of the $BaTiO_3$ surface. Especially, the stabilization of CH_3 led to the activation of CH_4, which became an exothermic reaction on the TiO_2-terminated surface. Additionally, the presence of sulfur helps to suppress carbon deposition.

When SnO_2 was used as support material for Pt-nanoparticles as electrocatalyst for PEFC, a low performance was reported. One of the factors behind the low performance is the stronger interaction of oxygenated species on the supported nanoparticles that will block the active sites for the oxygen reduction reaction (ORR) to occur. SnO_2 as support material led to changes in the interatomic distance and interaction, and electronic properties of the Pt-nanoparticles making them more oxophilic. The predicted O-atom binding energy on supported nanoparticles was more negative than on isolated ones, thus confirming that oxygenated species can effectively block the active sites of the Pt-nanoparticles required for the adsorption and dissociation of O_2. The strong interaction of oxygenated species on the supported Pt-nanoparticles can also lead to the formation of PtO_x, which are known to be prone to dissolution during the ORR. Regarding stability, SnO_2 weakened the Pt-Pt interaction of the outer-shell atoms of Pt_4, $Pt_{13,}$ and Pt_{37} compared to the isolated ones, while the interatomic interaction of larger size nanoparticles became slightly stronger, which in part can explain the higher stability of Pt/SnO_2 systems when used as polymer electrolyte fuel cell electrocatalyst.

5.2 FUTURE WORK

The performance of $BaTiO_3$ as anode for the SOFC increased due to the presence of sulfur. However, the output current density is not comparable to Ni-YSZ anode, which can be attributed to the low catalytic activity and mixed ionic-electronic conductivity of $BaTiO_3$. Thus, from this work results, the activation of the lattice oxygen is key for oxidation reactions, and to increase the activity. Additionally, the activation of the surface O-atom will help to prevent C-deposition and CO_2 formation increasing the lifetime of the catalyst. Also, the interaction of H_2O, CO, and CO_2 on pristine, sulfided, and doped $BaTiO_3$ may lead to degradation on the electrocatalyst due to the formation of various oxides, peroxides, hydroxides, and carbonates. Thus, it is important to elucidate at atomistic scale the probability and formation mechanisms of the previously mentioned compounds. These results can also provide insights not only for the activity but also for the durability of other perovskite-based materials that have been targeted as possible electrocatalyst.

In this study, it was shown that SnO_2 as support material will lead to the oxidation of Pt-nanoparticles due to charge transfer from the nanoparticles to SnO_2, which will decrease the nanoparticles' activity towards the ORR. The effect of different dopants on SnO_2 on the physical, electronic and chemical properties of Pt-nanoparticles should be assessed in this context. The effect of support should not be limited to the O-atom interaction but also the CO adsorption, and the feasibility for the CO_2 formation and CO poisoning the catalyst. Similarly, the poisoning effect of trace impurities such as chlorine and possible strategies of how to improve the electrocatalyst resistance will be interesting to study.